

5

3409

3410

3411

Longevity studies and Consolidation of the present CMS RPC system

3412 The RPC system, located in both barrel and endcap regions, provides a fast, independent muon
3413 trigger over a large portion of the pseudo-rapidity range ($|\eta| < 1.6$). During HL-LHC operations
3414 the expected conditions in terms of background and pile-up will make the identification and correct
3415 p_T assignment a challenge for the muon system. The goal of the RPC upgrade is to provide additional
3416 hits to the Muon System with more precise timing. All this information will be elaborated by the
3417 Trigger System in a global way enhancing the performance of the muon trigger in terms of efficiency
3418 and rate control. The RPC Upgrade consists of two projects: an improved Link Board System and
3419 the extension of the RPC coverage up to $|\eta| = 2.4$.

3420 The Link Board System is responsible for the processing, the synchronization and the zero-
3421 suppression of the signals coming from the RPC FEBs. The Link Board components have been
3422 produced between 2006 and 2007 and will be subjected to ageing and failure on a long term scale.
3423 An upgraded Link Board System will overcome the ageing problems and will allow for a more
3424 precise timing information to the RPC hits from 25 to 1.5 ns.

3425 In order to develop an improved RPC that fulfills CMS requirements, an extensive R&D program is
3426 being conducted. The benefits of adding two new RPC layers in the innermost ring of stations 3 and
3427 4 will be mainly observed in the neutron-induced background reduction and efficiency improvement
3428 for both the muon trigger and the offline reconstruction.

3429 The coverage of the RPC System up to higher pseudo-rapidity $|\eta| = 2.1$ was part of the original
3430 CMS TDR. Nevertheless, the expected background rates being higher than the certified rate capa-
3431 bility of the present CMS RPCs in that region and the budget being limited, RPCs were restricted to
3432 a smaller pseudo-rapidity range. Even though the iRPC technology that will equip the extension of
3433 the Muon System will be different than the current CMS RPC technology, it is necessary to certify
3434 the rate capability and longevity of the existing detectors as the radiation level will increase together
3435 with the increase of instantaneous luminosity of the LHC. For this purpose, unused spare CMS RPC
3436 detectors have been installed in different irradiation facilities, first of all, to certify the detectors to

the new levels of irradiation they will be subjected to and, finally, to study their ageing and certify their good operation throughout the HL-LHC program.

This chapter will discuss the longevity and consolidation studies of the present CMS RPC system to which I have contributed. Two different irradiation facilities have been used at CERN. In each of them I took a leading role in defining the experimental set-up, but also in the data collection and data analysis. In the first facility in which preliminary tests were conducted, I also worked on simulations of the experimental setup and I made predictions on the particle rate expected at the detector level. During the last 4 years of longevity test conducted in the second facility, I became a DAQ expert and built a software which is now the base for the data collection to study the longevity of CMS RPCs. Moreover, I also worked together with the Detector Control Software (DCS) expert to provide an online monitoring of the collected data. Indeed, I developed a software that automates the extractions of the detectors' data and produces plots at destination of the users thanks to a fast analysis. This software is a corner stone for the final data analysis. Documentations of both these softwares are given in Appendix A and Appendix B.

In a first section of the chapter, the irradiation facilities will be described. The study conducted will then be summarized in details. A description of the set-ups as well as a comprehensive review of the obtained results will be provided.

5.1 Testing detectors under extreme conditions

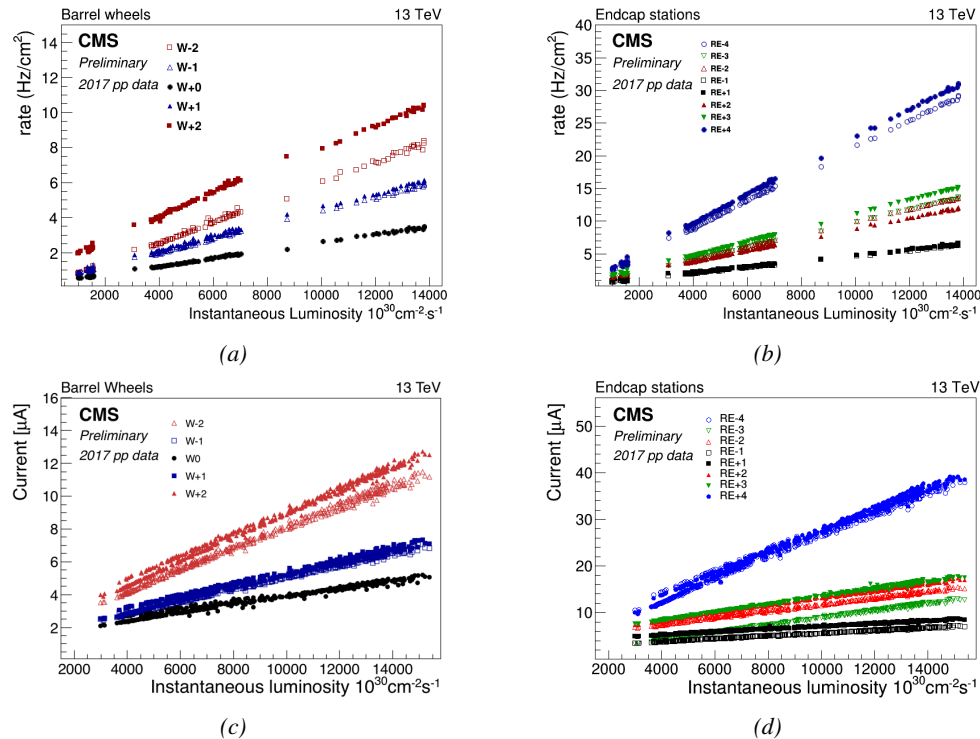


Figure 5.1: Mean RPC Barrel (left column) and Endcap (right column) rate (top row) and current (bottom row) as a function of the instantaneous luminosity as measured in 2017 p-p collision data.

The upgrade from LHC to HL-LHC will increase the peak luminosity from 10^{34} $\text{cm}^{-2} \text{s}^{-1}$ to 5×10^{34} $\text{cm}^{-2} \text{s}^{-1}$, increasing the total expected background to which the RPC system will be subjected. Mainly composed of low energy gammas, neutrons, and electrons and positrons from $p\text{-}p$ collisions, but also of low momentum primary and secondary muons, punch-through hadrons from calorimeters, and particles produced in the interaction of the beams with collimators, the background will mostly affect the regions of CMS that are the closest to the beam line, i.e. the RPC detectors located in the endcaps.

Data collected during 2017, presented in Figure 5.1, allows to study the values of the background rate in the entire RPC system. This was achieved thanks via the monitoring of the rates in each RPC rolls and of the current in each HV channel. A linear dependence of the mean rate or current on the instantaneous luminosity is shown in selected runs with identical LHC running parameters. It is assumed that such a linear behaviour should be observed at even higher luminosities and is therefore used to extrapolate the rates and currents that will be expected during HL-LHC. In Figure 5.2, a linear extrapolation of the distribution of the background hit rate per unit area as well as the integrated charge is shown at a HL-LHC condition. The maximum hit rate per unit area in the endcap detectors at HL-LHC conditions is expected to be of the order of 600 Hz/cm² while the charge deposition should exceed 800 mC/cm². The detectors will thus have to be certified up to an irradiation of 840 mC/cm². These extrapolations are provided with a required safety factor 3 for the certification study.

In the past, extensive long-term tests were carried out at several gamma and neutron facilities certifying the detector performance. Both full size and small prototype RPCs have been irradiated with photons up to an integrated charge of $\sim 0.05 \text{ C/cm}^2$ and $\sim 0.4 \text{ C/cm}^2$ respectively and were certified for rates reaching 200 Hz/cm² [262, 263]. Since the beginning of Run-I until December 2017, the RPC system provided stable operation and excellent performance. The average integrated charge is of about 1.66 mC/cm² in the Barrel and 4.58 mC/cm² in the Endcap, closer to the beam line, as can be seen in Figure 5.3). The detectors did not show any ageing effects for a maximum integrated charge in a detector of the order of 0.01 C/cm² and a peak luminosity reaching 1.4×10^{34} $\text{cm}^{-2} \text{s}^{-1}$ during the 2017 data taking period.

To perform the necessary studies on the present CMS RPC detectors, facilities offering the possibility to irradiate the chambers are necessary in order to recreate HL-LHC conditions or stronger and

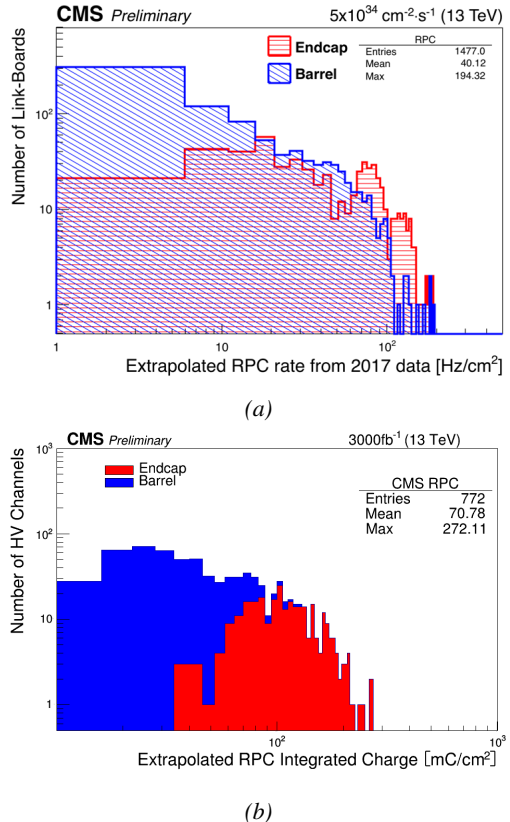


Figure 5.2: Linear extrapolation of the hit rate (a) and of the integrated charge (b) per region (Barrel, Endcap) respectively to HL-LHC instantaneous luminosity ($5 \times 10^{34} \text{ cm}^{-2} \text{s}^{-1}$) and HL-LHC integrated luminosity (3000 fb^{-1}).

study the detector performance through time. A first series of such studies was conducted in the former Gamma Irradiation Facility (GIF) of CERN before its dismantlement starting from September 2014. This preliminary study was used as a stepping stone towards the building of a more powerful irradiation fully dedicated to longevity studies of CMS and ATLAS subsystems in the perspective of HL-LHC. The period of preliminary work has also been a key moment in the elaboration and improvement of data acquisition, offline analysis and online monitoring tools that are extensively used in the new gamma irradiation facility.

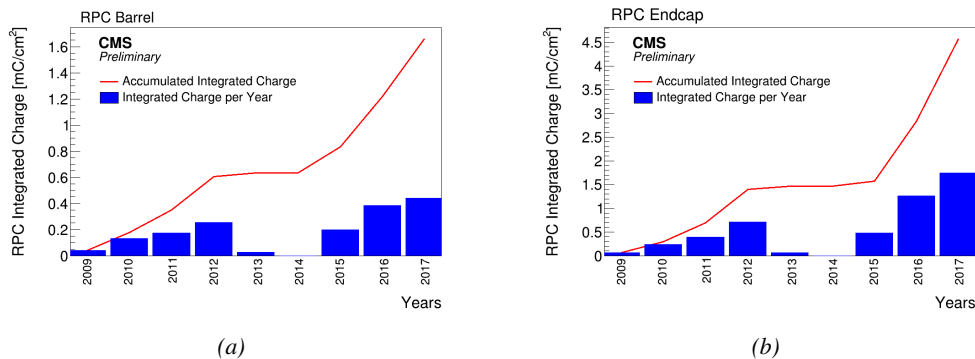


Figure 5.3: CMS RPC mean integrated charge in the Barrel region (a) and the Endcap region (b). The integrated charge per year is shown in blue. The red curve shows the evolution of the accumulated integrated charge through time. The blank period in 2013 and 2014 corresponds to LS1.

5.1.1 The Gamma Irradiation Facility

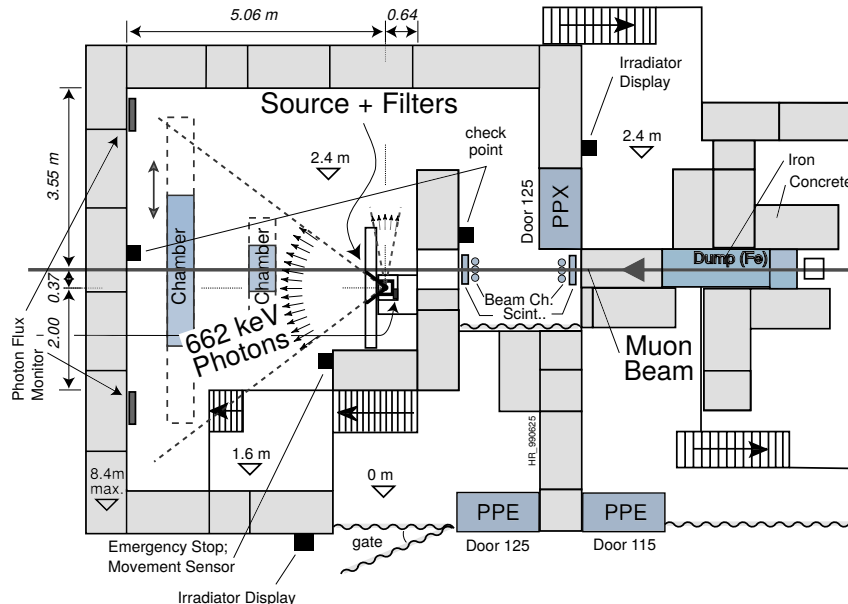


Figure 5.4: Layout of the test beam zone of GIF at CERN.

3509 Located in the SPS West Area at
 3510 the downstream end of the X5 test
 3511 beam, the GIF was a test area in
 3512 which particle detectors were ex-
 3513 posed to a particle beam in pres-
 3514 ence of an adjustable gamma back-
 3515 ground [264]. Its goal was to repro-
 3516 duce background conditions these
 3517 detectors would endure in their op-
 3518 erating environment at LHC. The
 3519 layout of the GIF is shown in Figure
 3520 5.4. Gamma photons are produced
 3521 by a strong ^{137}Cs source installed in
 3522 the upstream part of the zone inside

3523 a lead container. The source container includes a collimator, designed to irradiate a $6 \times 6 \text{ m}^2$ area at
 3524 5 m maximum distance to the source. A thin lens-shaped lead filter helps providing with a uniform
 3525 out-coming flux in a vertical plane, orthogonal to the beam direction. The photon rate is controlled
 3526 by further lead filters allowing the maximum rate to be limited and to vary within a range of four
 3527 orders of magnitude. Particle detectors under test are then placed within the pyramidal volume in
 3528 front of the source, perpendicularly to the beam line in order to profit from the homogeneous photon
 3529 flux. Adjusting the background flux of photons can then be done using the filters and choosing the
 3530 position of the detectors with respect to the source. The zone is surrounded by 8 m high and 80 cm
 3531 thick concrete walls. Access is possible through three entry points. Two access doors for personnel
 3532 and one large gate for material. A crane allows installation of heavy equipment in the area.

3533 As described on Figure 5.5, the ^{137}Cs source emits a 662 keV photon in 85% of the decays. An
 3534 activity of 740 GBq was measured on the 5th of March 1997. The half-life of Cesium is well known
 3535 ($t_{1/2} = (30.05 \pm 0.08) \text{ y}$) and can be used to compute the activity of the source at the time of the
 3536 study. The GIF tests were done in between the 20th and the 31st of August 2014, i.e. at a time $t =$
 3537 $(17.47 \pm 0.02) \text{ y}$ resulting in an attenuation of the activity from 740 GBq in 1997 to 494 GBq in
 3538 2014.

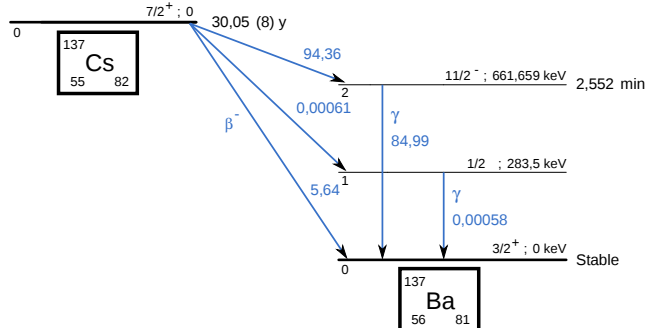


Figure 5.5: ^{137}Cs decays by β^- emission to the ground state of ^{137}Ba ($BR = 5.64\%$) and via the 662 keV isomeric level of ^{137}Ba ($BR = 94.36\%$) whose half-life is 2.55 min.

3539 5.1.2 The new Gamma Irradiation Facility

3540 The GIF++, located in the SPS North Area at the downstream end of the H4 test beam, has replaced
 3541 its predecessor during LS1 and has been operational since spring 2015 [265]. Like GIF, GIF++
 3542 features a ^{137}Cs source of 662 keV gamma photons, their fluence being controlled with a set of
 3543 filters of various attenuation factors. The source provides two separate large irradiation areas for
 3544 testing several full-size muon detectors with homogeneous irradiation, as presented in Figure 5.6.

3545 The source activity was measured to be about 13.5 TBq in March 2016. With the photon flux
 3546 being far greater than HL-LHC expectations, GIF++ provides an excellent facility for accelerated
 3547 ageing tests of muon detectors. The source is situated in a bunker designed to perform irradia-
 3548 tion test along a muon beam line, which is available during selected periods throughout the year.
 3549 The H4 beam, providing the area with muons with a maximum momentum of about 150 GeV/c,
 3550 passes through the GIF++ zone and is used to periodically study the performance of the detectors
 3551 placed under long term irradiation. Its flux is of 104 particles/s/cm² focused in an area of about
 3552 $10 \times 10 \text{ cm}^2$.

	1	2	3
A	1	10	100
B	1	1.468	100
C	1	2.154	4.642

Table 5.1: Attenuation of single filters on each filter plane of the GIF++ Cesium source.

attenuation factor (for example $333 = 100 \times 100 \times 4.642 = 46420$).

Adjusting the gamma flux is possible thanks to the three planes (A, B and C) of adjustable absorbers featured on the Cesium source [266]. With properly adjusted filters, one can simulate the background expected at HL-LHC and study the performance and ageing of muon detectors in HL-LHC environment. Each plane of filters features three filters (1, 2 and 3) with different Absorption factor (ABS) listed in Table 5.1. The source absorber settings can be referred by a three digit number with a format ABC or by its

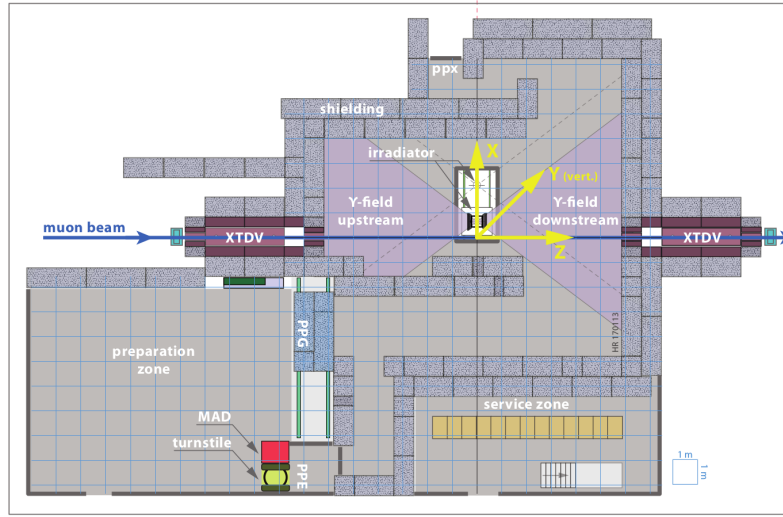


Figure 5.6: Floor plan of the GIF++ facility. When the facility downstream of the GIF++ takes electron beam, a beam pipe is installed along the beam line (z -axis). The irradiator can be displaced laterally (its center moves from $x = 0.65$ m to 2.15 m), to increase the distance to the beam pipe.

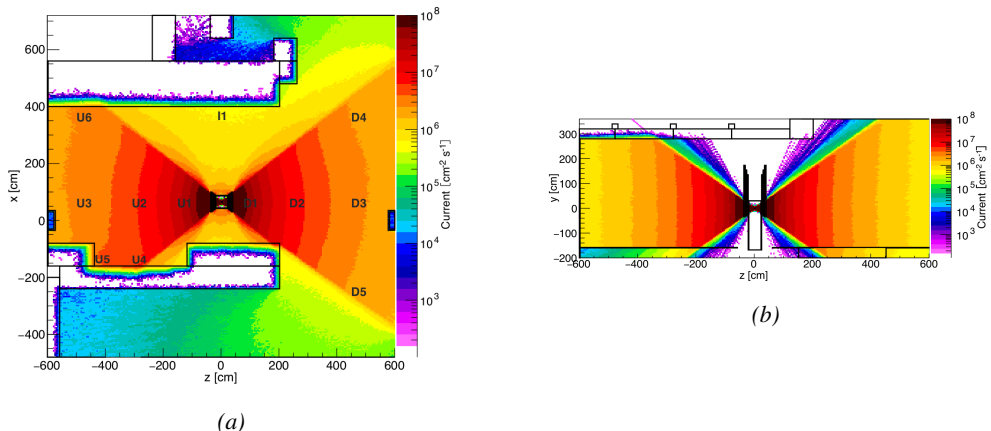


Figure 5.7: Simulated unattenuated current of photons in the xz plane (a) and yz plane (b) through the source at $x = 0.65$ m and $y = 0$ m [267]. With angular correction filters, the current of 662 keV photons is made uniform in xy planes.

The gamma current as simulated with GEANT4 is presented in Figure 5.7. In their simulation paper [267], Pfeiffer et al. define the particle current as "a measure of the net number of particles crossing a flat surface with a well-defined orientation. The unit of current is $\text{m}^{-2} \text{s}^{-1}$ and thus identical to the unit of flux. Current is meaningful in cases where particles are counted without any interest in their interactions." The labels UN, DN, with $N \in [1 : 5]$ and I1 correspond to the position of different Radiation Monitoring (RADMON) sensors measuring the irradiation in the bunker area [267]. According to the simulation results, that agree within 12% to the doses measured with the RADMONs, the RPCs that will be tested in GIF++ can expect a maximal gamma current of the order of 2 to $5 \times 10^6 \text{ cm}^{-2} \text{s}^{-1}$ assuming they will always stay in a region in between sensor U5 and the back wall of the upstream area.

5.2 Preliminary studies at GIF

5.2.1 RPC test setup

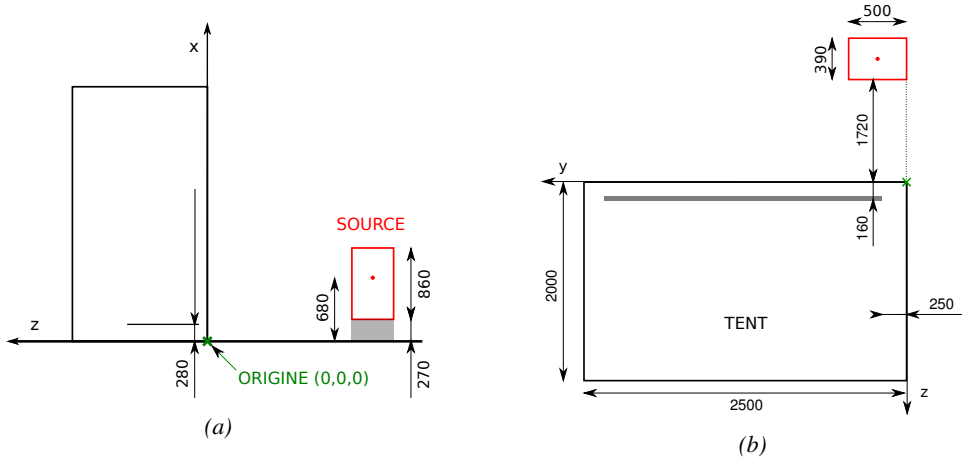


Figure 5.8: Description of the RPC setup. Dimensions are given in mm. A tent containing RPCs is placed at 1720 mm from the source container. The source is situated in the center of the container. RE-4-2-BARC-161 chamber is 160 mm inside the tent. This way, the distance between the source and the chambers plan is 2060 mm. Figure (a) provides a side view of the setup in the xz plane while Figure (b) shows a top view in the yz plane.

During Summer 2014, preliminary tests have been conducted in the GIF area on an endcap chamber of type RE4/2 and labeled RE-4-2-BARC-161 produced for the extension of the endcap with a fourth disk in 2013. This chamber has been placed into a trolley covered with a tent in order to control the temperature. The positions of the RPC inside the tent and of the tent with respect to the source in the bunker are described in Figure 5.8. The goal of the study was to have a preliminary understanding of the rate capability of the present technology used in CMS. It was decided to measure the efficiency of the RPC under irradiation for detecting cosmic muons as, at the time of the tests, the beam was not operational anymore. Three different absorber settings were used and compared to the case where the detector was not irradiated in order to study the evolution of the performance of the detector with increasing exposure to gamma radiation. First of all, measurements were done with the fully opened source. To complete this preliminary study, the gamma flux has been attenuated by

3585 a factor 2, a factor 5 and finally the source was shut down. The efficiency of the RPC at detecting
 3586 the cosmic muons in coincidence with a cosmic trigger as well as the background rate as seen by the
 3587 detectors were measured.

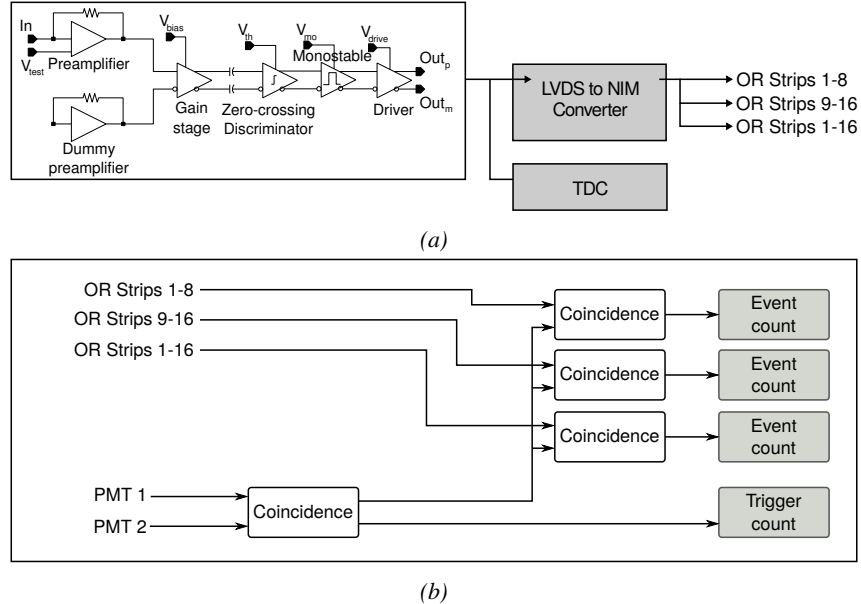


Figure 5.9: (a) Shaping of the signals from the RPC strips by the FEE. The output LVDS signals are then read-out by a TDC module connected to a computer or converted into NIM and sent to scalers. (b) Trigger logic implementation with the RPC and photomulitplier signals.

3588
 3589
 3590
 3591
 3592
 3593
 3594
 3595
 3596
 3597
 3598
 3599
 3600



3601 *Figure 5.10: RE-4-2-BARC-161 chamber is inside the tent as*
 3602 *described in Figure 5.8. In the top right, the two scintillators used*
 3603 *as trigger can be seen.*

3604
 3605
 3606
 3607

libraries and the data collected by the TDCs was saved into .dat files is analysed with an algorithm computing parameters such as efficiency, hit profile, cluster size, or gamma and noise rates which was developed with C++ as well. Finally, histograms and curves are produced using ROOT.

The data taking was performed using a CEAN TDC module of type V1190A [268] to which the digitized output of the RPC Front-End Board is connected, as described in Figure 5.9a and the trigger signal from the telescope. The communication with the computer is performed thanks to a CAEN communication module of type V1718 [269]. In order to control the rates recorded by the detector, the digitized RPC signals are also sent to scalers as described in Figure 5.9b. The C++ DAQ software used in GIF was developed as an early attempt towards the understanding of the CAEN li-

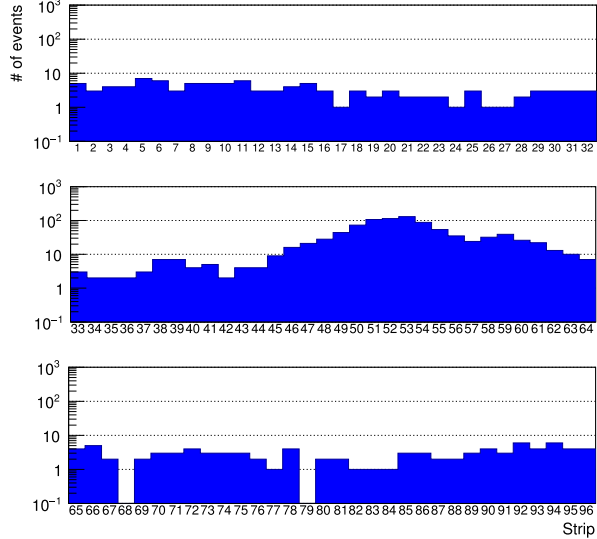
3608 The trigger system was com-
 3609 posed of two plastic scintillators and
 3610 was placed in front of the setup with
 3611 an inclination of 10° with respect to
 3612 the detector plane in order to look at
 3613 cosmic muons. Using this particular
 3614 trigger layout, shown in Figure 5.10,
 3615 lead to a cosmic muon hit distribution
 3616 into the chamber similar to the
 3617 one of Figure 5.11. As mentioned
 3618 in Chapter 2, the endcap RPC read-
 3619 out is segmented into three pseudo-
 3620 rapidity partitions. The outer most
 3621 partition, corresponding to the wide
 3622 end of the chamber, is the partition
 3623 A. The other two partitions are the
 3624 partitions B and C. Each of them
 3625 consists in 32 copper strips. These
 3626 32 strips are connected to the FEEs
 3627 by groups of 16. The trigger is
 3628 placed in front of the half-partition
 3629 B2 which corresponds to the last 16 strips of partition B (49 to 64).

3630 Measured without gamma irradiation, two peaks can be seen on the profile of readout partition
 3631 B, centered on strips 52 and 59. Some events still occur in other half-partitions than B2 contributing
 3632 to the inefficiency of detection of cosmic muons. In the case of partitions A and C, the very low
 3633 amount of data can be interpreted as noise. On the other hand, it is clear that a little portion of
 3634 muons reached the half-partition B1 (strips 33 to 48). Section 5.2.2 will help us understand that
 3635 these two peaks are due respectively to forward and backward coming cosmic particles. Forward
 3636 coming particles are detected first by the scintillators and then the RPC while the backward going
 3637 muons are first detected in the RPC.

3638 **5.2.2 Geometrical acceptance of the setup layout to cosmic muons**

3639 In order to profit from a constant gamma irradiation, the detectors inside of the GIF bunker had to be
 3640 placed in a plane orthogonal to the beam line. The muon beam that used to be available was meant to
 3641 test the performance of detectors under test. This beam being not active anymore, another solution
 3642 to test detector performance had to be used. Thus, it was decided to use cosmic muons detected
 3643 through a telescope composed of two scintillators. Lead blocks were used as shielding to protect the
 3644 photomultipliers from gammas as can be seen from Figure 5.10.

3645 An inclination of $\sim 10^\circ$ was given to the cosmic telescope to increase the muon trigger rate for
 3646 this otherwise horizontal setup. A good compromise had to be found between good enough muon
 3647 flux and narrow enough hit distribution to be sure to contain all the events into a single half-partition
 3648 as required from the limited available readout hardware. It was then foreseen to detect muons and
 3649 read them out only from half-partition B2. Nevertheless, a misplacement of the trigger scintillators
 3650 resulted in an inefficiency, as can be seen in Figure 5.11 with events appearing in half-partition B1.



3651 *Figure 5.11: Hit distributions over all three partitions of
 3652 RE-4-2-BARC-161 chamber is showed. Top, middle and bottom
 3653 figures respectively correspond to partitions A, B, and C.*

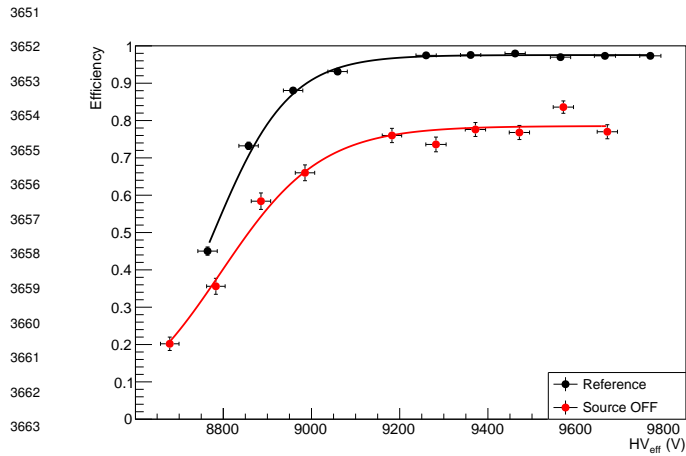


Figure 5.12: Comparison of the efficiency of chamber RE-4-2-BARC-161 with and without irradiation. Results are derived from data taken on half-partition B2 only.

by the red curve. The inefficiency too high compared to the 12.7% of data contained into the first 16 strips observed on Figure 5.11, to be explained only by the geometrical acceptance of the setup itself. Simulations have been conducted to quantify the inefficiency of the setup.

As can be seen in Figure 5.12, a comparison of the performance of chamber RE-4-2-BARC-161 with and without irradiation suggests an inefficiency of approximately 20%. On the 18th of June 2014, data have been taken on the chamber at CERN building 904 (Prevessin Site) with cosmic muons providing us a reference efficiency plateau of $(97.54 \pm 0.15)\%$ represented by the black curve. A similar measurement has been done at GIF on the 21st of July with the same chamber giving a plateau of $(78.52 \pm 0.94)\%$ represented

5.2.2.1 Geometrical acceptance simulation setup

The layout of the GIF setup has been reproduced¹ and incorporated into a C++ Monte Carlo (MC) simulation to study the geometrical acceptance of the telescope projected onto the readout strips [270]. A 3D view of the simulated layout is given into Figure 5.13. The RPC read-out plane is represented as a yellow trapezoid while the two scintillators as blue cuboids. The green plane corresponds to the $4 \times 4.5 \text{ m}^2$ muon generation plane centered on the experimental setup within the simulation. The goal of the simulation is to look at muons that pass through the telescope composed of the two scintillators and define their distribution onto the RPC read-out plane. During the reconstruction, the read-out plane is then divided into its read-out strips and each muon track is assigned to a strip.

$N_\mu = 10^8$ muons are generated at a random position in the horizontal generation plane. This position corresponds to the intersection of the muon track with the generaltion plane. The plane is located at a height corresponding to the lowest point of the scintillators in order to easily simulate muons coming at very large zenith angles (i.e. $\theta \approx \pi$). The position of the particle within the plane is associated with a random direction: an azimuth angle ϕ chosen between 0 and 2π and a zenith angle θ chosen between 0 and $\pi/2$ to follow a usual $\cos^2\theta$ distribution for cosmic particles. Then, using the position of the muon in the generation plane and its direction, the intersection of the track with the planes of the scintillator cuboids is computed. In the case the muon wasn't found within the surface of both the scintillators, the simulation restarts and generates a new muon. On the contrary, if the track passed through the telescope, the simulation goes on. The position of the muon hit within the RPC read-out plane is computed. The hits are saved into histograms, one per read-out partition,

¹Albeit only roughly using Figure 5.10 due to the lack of actual measurements of the respective positions of each parts of the experimental setup. Using reference dimensions such as the saize of the detector and the size of the photomultiplier, the positions could be deduced.

whose bins corresponds to the RPC copper strips. The strip in which the hit occured is determined by knowing precisely the geometry of the RPC. Muon hits are also filled in different histograms whether they are associated to forward coming ($\pi \leq \phi < 2\pi$) or backward going ($0 \leq \phi < \pi$) muons.

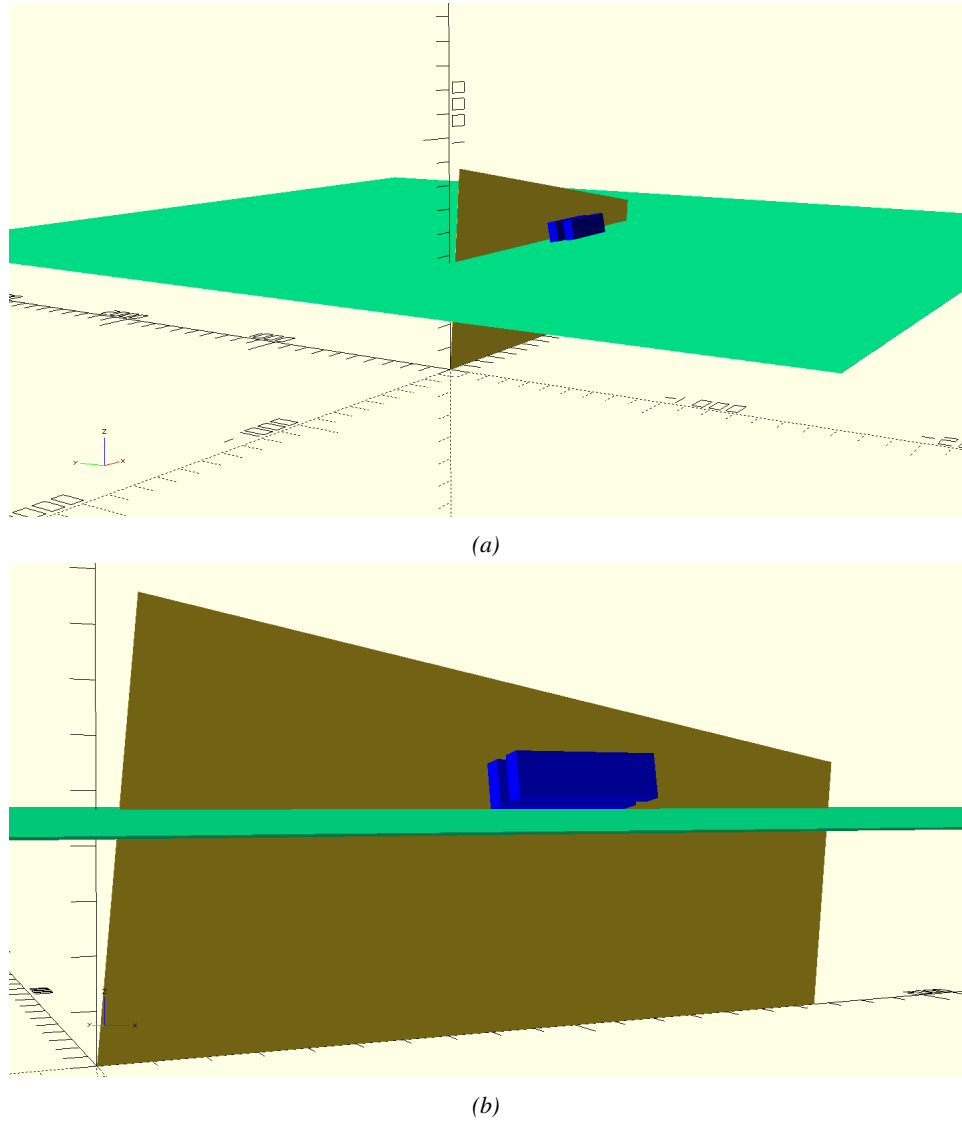
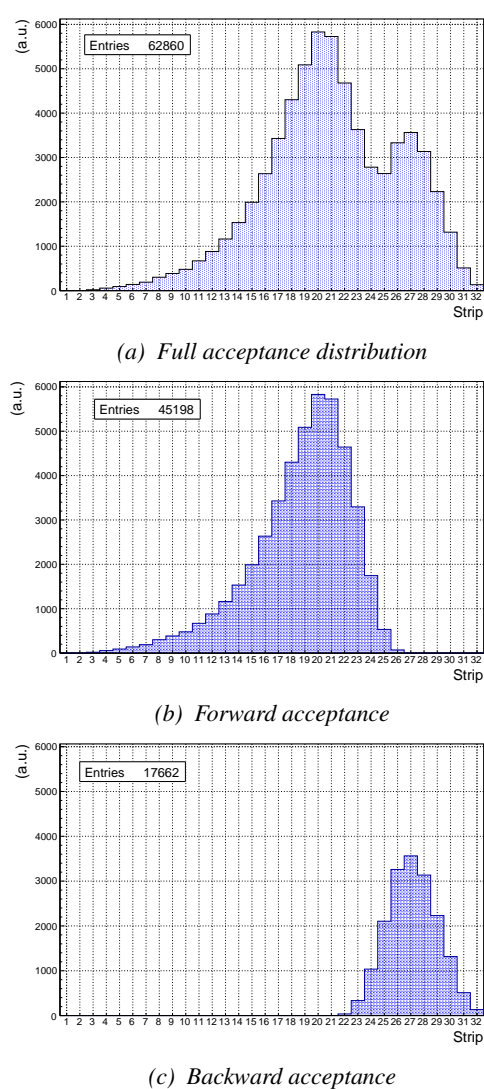


Figure 5.13: Representation of the layout used for the simulations of the test setup. (a) Global view of the simulated setup. (b) Zoomed view on the experimental setup.

3696 5.2.2.2 Results and limitations



3729 *Figure 5.14: Geometrical acceptance distribution as
3730 provided by the Monte Carlo simulation.*

3731 affected by a variation of the inclination angle, as can be seen in Figure 5.16. Yet, the position of
3732 the acceptance peaks in the distribution would be in agreement with what is measured, and the con-
3733 tribution of farward and backward muons would never reach the observation. With an inclina-
3734 tion of 10° , 28.1% of the total geometrical acceptance should contribute to detecting backward muons
3735 whereas it is measured that the hit profile contains 22.0% of backward data only. Introducing in the
3736 simulation an error of $\pm 2^\circ$ would lead to a correction factor $c_{geo} = 1.20^{+0.04}_{-0.03}$ allowing for a good
3737 improvement of the efficiency measured in GIF, as can be seen from Figure 5.17. GIF measurement
3738 is in agreement with the reference curve within statistical errors.

The output from the simulation is given in Figure 5.14 in which the geometrical acceptance distribution of the setup is shown. The distributions for the separate contributions of forward coming and backward going muons are all provided. The strip number is given in a range of 1 to 32 corresponding to the 32 strips contained in each RPC read-out partition even though partition B corresponds, by convention, to strip numbers 33 to 64. It can be established that, out of the total amount of muons that have passed through the telescope and reached the RPC, 16.8% were hitting the 16 first strip of the read-out plane corresponding to half partition B1. This number corresponds to the inefficiency. It can be used then to correct the data by scaling up by a factor $c_{geo} = 1/(1 - 0.168)$ the efficiency measured during data taking.

Nevertheless, the distribution showed in Figure 5.14a differs from the measured hit profile showed in Figure 5.11 as can be seen in Figure 5.15. It is difficult to evaluate a systematic uncertainty on this geometrical correction for different reasons.

First of all, even though the dimensions of the scintillators and of the RPC are well known, the position of each element of the setup with respect to one another was not measured. The extraction of the position of each part of the setup from Figure 5.10 was a first large source of error.

The inclination is also roughly measured to be 10° bringing more uncertainty into the simulation. The acceptance distribution would be

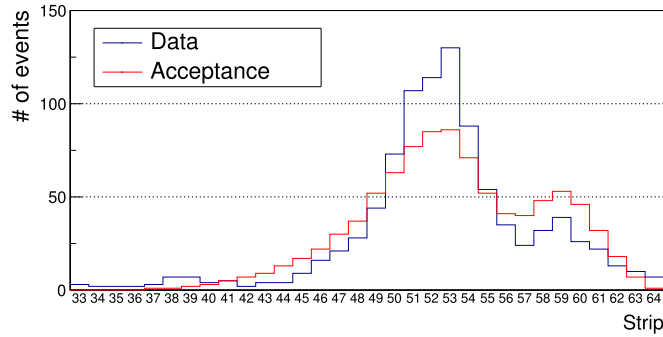


Figure 5.15: Comparison of the hit distribution recorded in the detector and of the normalised geometrical acceptance distribution.

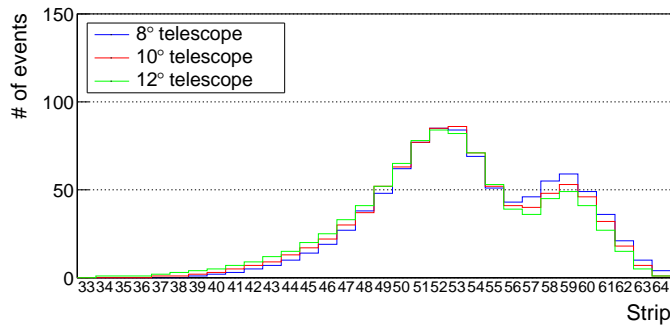


Figure 5.16: Effect of the variation of telescope inclination on the normalised geometrical acceptance distribution.

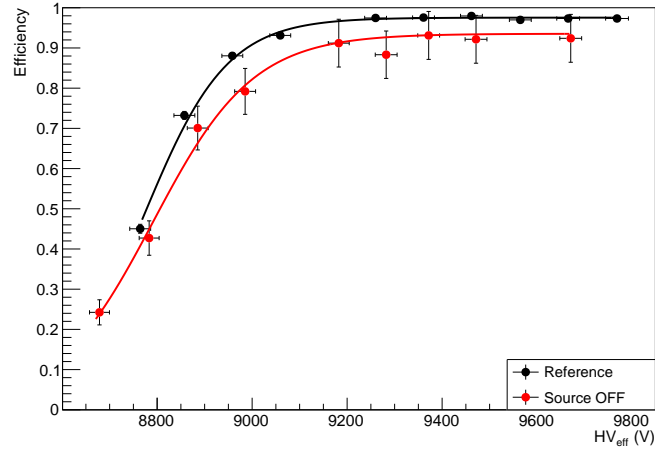


Figure 5.17: Correction of the efficiency without source. The efficiency after correction gets much closer to the Reference measurement performed before the study in GIF by reaching a plateau of $(93.52 \pm 2.64)\%$.

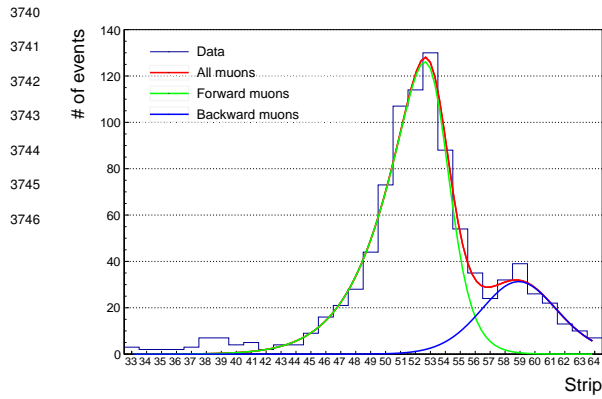


Figure 5.18: Hit distributions over read-out partition B of RE-4-2-BARC-161 chamber together with skew distribution fits corresponding to forward and backward coming muons.

Given the observed difference between the simulation and the measured data, one should realize that the geometrical acceptance and the hit profile are actually not directly comparable. The geometrical acceptance only provides with the information about what the detector can expect to see in a perfect world where all muons are detected in the exact same way. The detection would be independent from their energy or angle of incidence, and there would be no fluctuation of the detector gain due to complex avalanche development. No thresholds would be applied on the scintillators and on the RPC FEEs to reduce the noise, the cross-talk and the corresponding spread of the induced charge observed on the read-out strips. The hit profile provides the final product of all the previously mentioned contributions and can greatly differ from purely geometrical considerations. A full physics analysis involving softwares such as GEANT would be required to further refine the correction on the measured efficiency at GIF.

5.2.3 Photon flux at GIF

In order to understand and evaluate the γ flux in the GIF area, simulations have been conducted at the time GIF was opened for research purposes [264]. Table 5.2 gives the γ flux for different distances D to the source. The simulation was done using GEANT and a Monte Carlo N-Particle (MCNP) transport code, and the flux F is given with the estimated error from these packages expressed in %.

Nominal ABS	Photon flux F [$\text{cm}^{-2} \text{s}^{-1}$]			
	at $D = 50 \text{ cm}$	at $D = 155 \text{ cm}$	at $D = 300 \text{ cm}$	at $D = 400 \text{ cm}$
1	$0.12 \times 10^8 \pm 0.2\%$	$0.14 \times 10^7 \pm 0.5\%$	$0.45 \times 10^6 \pm 0.5\%$	$0.28 \times 10^6 \pm 0.5\%$
2	$0.68 \times 10^7 \pm 0.3\%$	$0.80 \times 10^6 \pm 0.8\%$	$0.25 \times 10^6 \pm 0.8\%$	$0.16 \times 10^6 \pm 0.6\%$
5	$0.31 \times 10^7 \pm 0.4\%$	$0.36 \times 10^6 \pm 1.2\%$	$0.11 \times 10^6 \pm 1.2\%$	$0.70 \times 10^5 \pm 0.9\%$

Table 5.2: Total photon flux ($E_\gamma \leq 662 \text{ keV}$) with statistical error predicted considering a ^{137}Cs activity of 740 GBq at different values of the distance D to the source along the x-axis of irradiation field [264].

This estimation of the backward versus forward content in the data was done through a fit using a sum of two skew distributions given in Equation 5.1. Although a skew distribution lacks physical interpretation, it allows fitting easily such kind of data, as showed in Figure 5.18.

$$(5.1) \quad \begin{aligned} g(x) &= A_g e^{-\frac{(x-\bar{x})^2}{2\sigma^2}} \\ s(x) &= \frac{A_s}{1 + e^{-\lambda(x-x_i)}} \\ sk(x) &= g(x) \times s(x) \\ &= A_{sk} \frac{e^{-\frac{(x-\bar{x})^2}{2\sigma^2}}}{1 + e^{-\lambda(x-x_i)}} \end{aligned}$$

3763 The table however does not
 3764 provide in a direct way the flux
 3765 at the level of the RPC under
 3766 test. First of all, it is nec-
 3767 essary to extract the value of
 3768 the flux from the available data
 3769 contained in the original paper
 3770 and then to estimate the flux in
 3771 2014 at the time the experimen-
 3772 tation took place. The extraction will be performed for the case of a pointlike source emitting
 3773 isotropic and homogeneous gamma radiations. The flux F_0 is known at a given reference point sit-
 3774 uated at D_0 from the source. The gamma flux F at a distance D from the source will be expressed
 3775 with Equation 5.2, assuming that the flux decreases as $1/D^2$ and where c is a fitting factor that can
 3776 be written as in Equation 5.3. Finally, using Equation 5.3 and the data of Table 5.2, with $D_0 =$
 3777 50 cm as reference point, Table 5.3 can be built. It is interesting to note that c for each value of D
 3778 does not depend on the absorption factor.

$$(5.2) \quad F^{ABS} = F_0^{ABS} \times \left(\frac{cD_0}{D} \right)^2$$

$$(5.3) \quad c = \frac{D}{D_0} \sqrt{\frac{F^{ABS}}{F_0^{ABS}}} \\ \Delta c = \frac{c}{2} \left(\frac{\Delta F^{ABS}}{F^{ABS}} + \frac{\Delta F_0^{ABS}}{F_0^{ABS}} \right)$$

3781 For the range of D/D_0 values available, it is possible to use a simple linear fit to get the evolution
 3782 of c that can be expressed as $c(D/D_0) = aD/D_0 + b$. Using Formula 5.4, but neglecting the
 3783 uncertainty on D that will only be used when extrapolating the values for the position of the RPC
 3784 under test whose position is not perfectly known, the results shown in Figure 5.19 is obtained.
 3785 Figure 5.19b confirms that using only a linear fit to extract c is enough as the evolution of the rate
 3786 that can be obtained superimposes well on the simulation points.

$$(5.4) \quad F^{ABS} = F_0^{ABS} \left(a + \frac{bD_0}{D} \right)^2, \quad \Delta F^{ABS} = F^{ABS} \left[\frac{\Delta F_0^{ABS}}{F_0^{ABS}} + 2 \frac{\Delta a + \Delta b \frac{D_0}{D} + \Delta D \frac{bD_0}{D^2}}{a + \frac{bD_0}{D}} \right]$$

3787 During the 2014 Gif tests, the RPC read-out plane was located at a distance $D = 206$ cm from
 3788 the source. Moreover, to estimate the strength of the flux in 2014, it is necessary to consider the
 3789 nuclear decay through time of the Cesium source whose half-life is well known ($t_{1/2} = (30.05 \pm$
 3790 0.08) y). The very first source activity measurement has been done on the 5th of March 1997 while
 3791 the Gif tests were done in between the 20th and the 31th of August 2014, i.e. at a time $t =$
 3792 (17.47 ± 0.02) y resulting in an attenuation of the activity from 740 GBq in 1997 to 494 GBq in
 3793 2014. All the needed information to extrapolate the expected flux through the detector at the moment
 3794 of the Gif preliminary tests has now been assembled, leading to Table 5.4. By assuming an average
 3795 sensitivity of the RPC to γ emitted by the ^{137}Cs source of $(2 \pm 0.2) \times 10^{-3}$ [271], the order of
 3796 magnitude of the expected hit rate per unit area would be of the order of kHz for a fully opened
 3797 source, as reported in the last column of the table. As photons are not charged particles, they mainly

3798 interact with the electrodes where they are converted into electrons. The HPL electrodes are not very
 3799 sensitive to gamma photons, hence only a small fraction of the incoming flux is seen by the RPC.

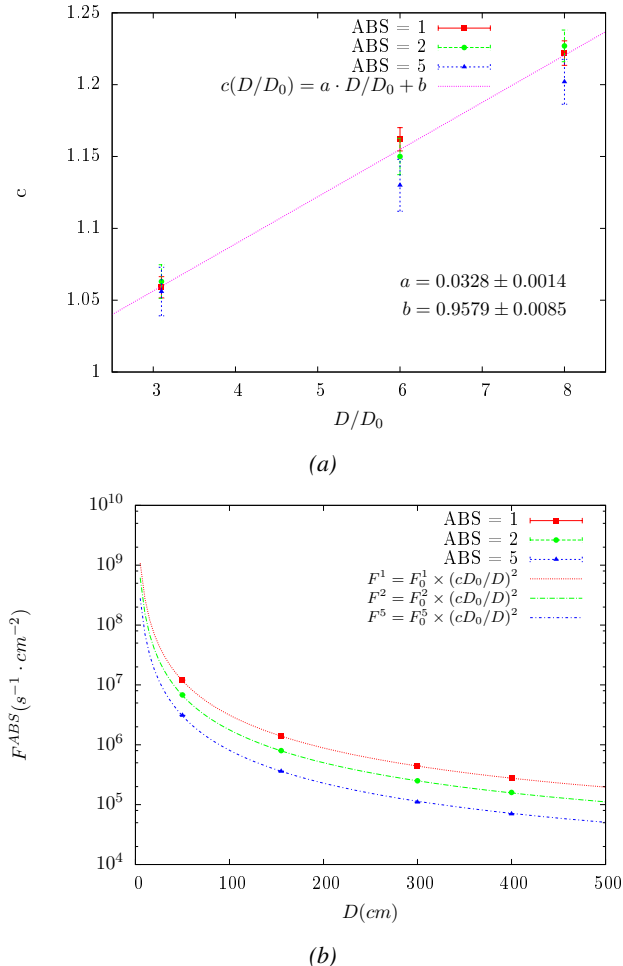


Figure 5.19: (a) Linear approximation fit performed on the data extracted from table 5.3. (b) Comparison of Equation 5.4 with the simulated flux using a and b given in figure 5.19a in Equation 5.2 and the reference $D_0 = 50$ cm and the associated flux for each absorption factor F_0^{ABS} from table 5.2.

Nominal ABS	Photon flux F [$cm^{-2} s^{-1}$]			Rate [Hz/cm ²] at $D^{2014} = 206$ cm
	at $D_0^{97} = 50$ cm	at $D^{97} = 206$ cm	at $D^{2014} = 206$ cm	
1	$0.12 \times 10^8 \pm 0.2\%$	$0.84 \times 10^6 \pm 1.2\%$	$0.56 \times 10^6 \pm 1.2\%$	1129 ± 14
2	$0.68 \times 10^7 \pm 0.3\%$	$0.48 \times 10^6 \pm 1.2\%$	$0.32 \times 10^6 \pm 1.2\%$	640 ± 8
5	$0.31 \times 10^7 \pm 0.4\%$	$0.22 \times 10^6 \pm 1.2\%$	$0.15 \times 10^6 \pm 1.2\%$	292 ± 4

Table 5.4: The data at D_0 in 1997 is taken from [264]. Using Formula 5.4, the flux at D , including an error of 1 cm, can be estimated in 1997. Then, taking into account the attenuation of the source activity, the flux at D can be estimated at the time of the tests in GIF in 2014. Assuming a sensitivity of the RPC to gammas, $s = (2 \pm 0.2) \times 10^{-3}$ [271], an estimation of the hit rate per unit area is obtained.

3800 The goal of the study was to have a good measurement of the intrinsic RPC performance without
 3801 source irradiation. Then, taking profit of the two working absorbers, at absorption factors 5 (300 Hz)
 3802 and 2 (~ 600 Hz) the goal was to show that the detectors fulfill the performance certification of CMS
 3803 RPCs. Finally, a first assessment of the performance of the detectors at higher backgrounds was
 3804 obtained with absorption factor 1 (no absorption and >1 kHz)).

3805 5.2.4 Results and discussions

3806 The data taking at GIF has been conducted between the 21st and the 31st of August, 2014. Data
 3807 have been collected with source both ON and OFF using three different absorber settings (ABS 5, 2
 3808 and 1) in order to vary the irradiation on the RPC. For each source setting, two HV scans have been
 3809 performed with two different trigger settings. During a first scan the trigger sent to the TDC module
 3810 was the coincidence of the two scintillators composing the telescope while during a second scan
 3811 the trigger was a pulse coming from a pulse generator in order to measure the noise or gamma rate
 3812 seen by the chamber. Indeed, using a pulse generator allows to trigger at moments not linked to any
 3813 physical event and, hence, to obtain a *RANDOM* trigger on noise and gamma events to measure the
 3814 associated rates, the probability to have a pulse in coincidence with a cosmic muon being negligible.

3815 From the cosmic trigger scans, a summary of the efficiencies and corresponding cluster sizes
 3816 is shown in Figure 5.20. The efficiency curves with Source ON show a shift with respect to the
 3817 case without irradiation. With ABS 5, the general shape of the efficiency curve stays unchanged
 3818 whereas a clear alteration of the performance is observed at ABS 2 and ABS 1. From the cluster
 3819 size results, a reduction of the mean cluster size under irradiation can be observed at equivalent
 3820 efficiency. This effect can be due to the perturbation of the electric field by the strong flux of gamma
 3821 particles interacting with the electrodes. With the increasing number of photons being converted
 3822 into electrons, an increasing number of charges need to be recombined all over the volume of the
 3823 electrodes that act as capacitors. A discharge of the electrodes reduces the effective field seen in the
 3824 gas volume by introducing a voltage drop across the electrodes thickness. The constant pressure put
 3825 on the detector by the converting photons can become strong enough to uniformly affect the gain of
 3826 the detector.

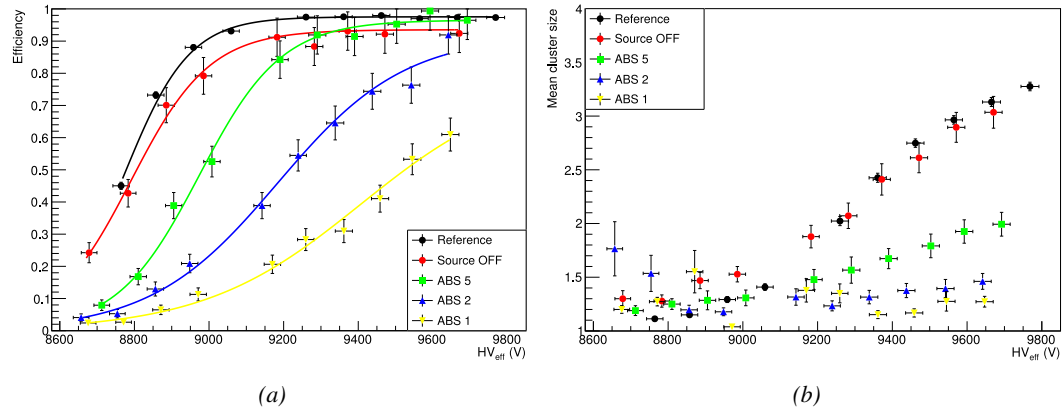


Figure 5.20: Efficiency (a) and cluster size (b) of chamber RE-4-2-BARC-161 measured at GIF with Source OFF (red) and Source ON using different absorber settings: ABS 5 (green), ABS 2 (blue) and ABS 1 (yellow). The results are compared to the Reference values obtained with cosmics.

3827 It is necessary to study the evolution of the performance of the chamber with the increasing rate
 3828 per unit area. The hit rate is measured as the number of hits detected in the RPC normalized to the
 3829 surface area of the read-out and to the total integrated time. The integrated time is linked to the time
 3830 window in which the TDC searches for data related to a trigger signal. Data is continuously kept in
 3831 the buffer of the TDCs but not all of these data is of interest. When a trigger signal is sent to the TDC
 3832 module, the TDC saves all of the data located in a certain time window set around the time stamp of
 3833 the signal. The total integrated time is then the total number of trigger signals times the width of a
 3834 search time window.

3835 In Figure 5.21a, the noise rate when the source is OFF remains low but increases at voltages above
 3836 9500 V. Aside of the natural increase of the noise with increasing voltage, the rise of the noise rate
 3837 in the detector can be related to the increased streamer probability observed with such a large electric
 3838 field. The rates measured at GIF with source ON all show a similar behaviour until a high voltage
 3839 of approximately 9400 V at which the rate of ABS 5 reaches a plateau, coinciding with the chamber
 3840 reaching full efficiency. It is important to note that, even though the rates look similar independently
 3841 from the gamma flux, relative to the efficiency of the chamber, the rate actually increases with
 3842 increasing flux at equivalent efficiency. A rough way to measure the rate effectively observed by
 3843 the detector for each source setting would be to normalize the measured rates to the efficiency of
 3844 the detector. This exercise was done with Figure 5.21b from which constant fits were done on
 3845 Source ON data in order to extract the rate the chamber was subjected to. This method leads to
 3846 rates of (164 ± 12) Hz/cm², (340 ± 26) Hz/cm² and (598 ± 50) Hz/cm² respectively for ABS 5,
 3847 2 and 1 which is consistent with the absorber values. Also, contrary to the case of the source OFF
 3848 measurement, no rise of the noise is observed at ABS 5. This difference could be explained by
 3849 the efficiency shift that is related to a decrease of the electric field across the gas volume. [But, as
 3850 **no data were taken at higher voltage values, this assumption can't be confirmed.**] Could be
 3851 confirmed by a study of the streamer probability for each dataset.

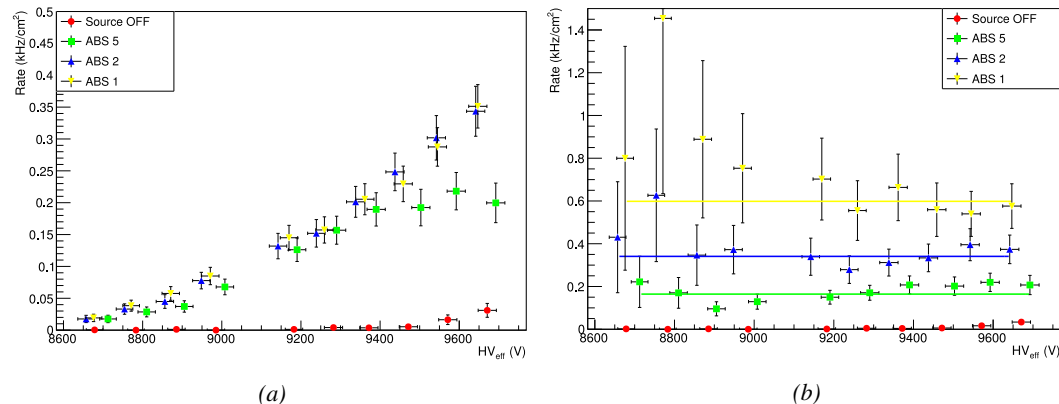


Figure 5.21: Rates in chamber RE-4-2-BARC-161 measured at GIF with Source OFF (red) and Source ON using different absorber settings: ABS 5 (green), ABS 2 (blue) and ABS 1 (yellow). On Figure (b), the rates of Figure (a) were normalized to the measured efficiency, and constant fits are performed on Source ON data showing the gamma rate in the chamber.

3852 The results need to be taken with care as a better estimation of the rate would have been to push
 3853 the detector towards higher voltages to reach the efficiency plateau for each absorber configuration
 3854 and only then extract the measured rate at working voltage, defined as in Formula 3.25. Nevertheless,

3855 using this method to estimate the rate to which the chamber is subjected, it is possible to look at the
 3856 evolution of the HV_{50} and HV_{knee} as a function of the increasing rate as showed in Figure 5.22.
 3857 The results from GIF suggest that at a rate of 600 Hz/cm^2 the working voltage of the chamber is
 3858 increased by a thousand V while the efficiency is reduced to approximately 80%, although the result
 3859 still is consistent with an efficiency better than 90% due to the large error on the measurement.

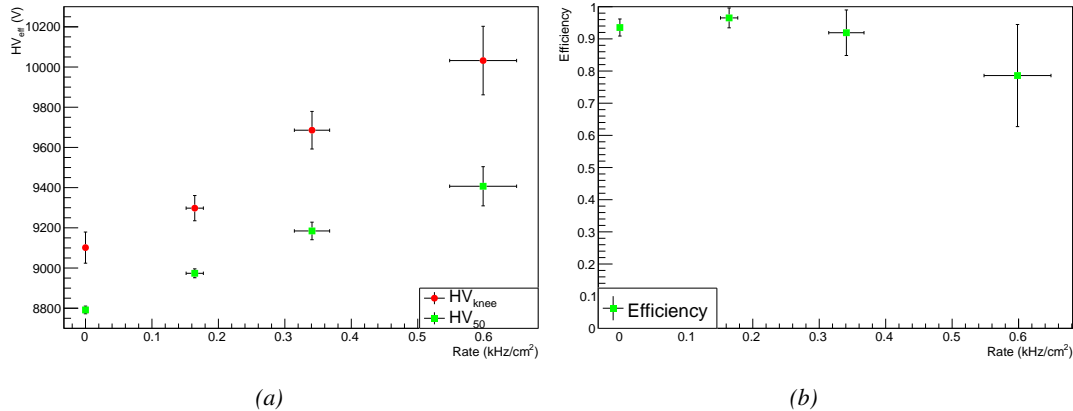


Figure 5.22: Evolution of the voltages at half maximum and at 95% of the maximum efficiency (Figure 5.22a), and of the maximum efficiency (Figure 5.22b) as a function of the rate in chamber RE-4-2-BARC-161. The data is extracted from the fits in Figures 5.20a and 5.21b.

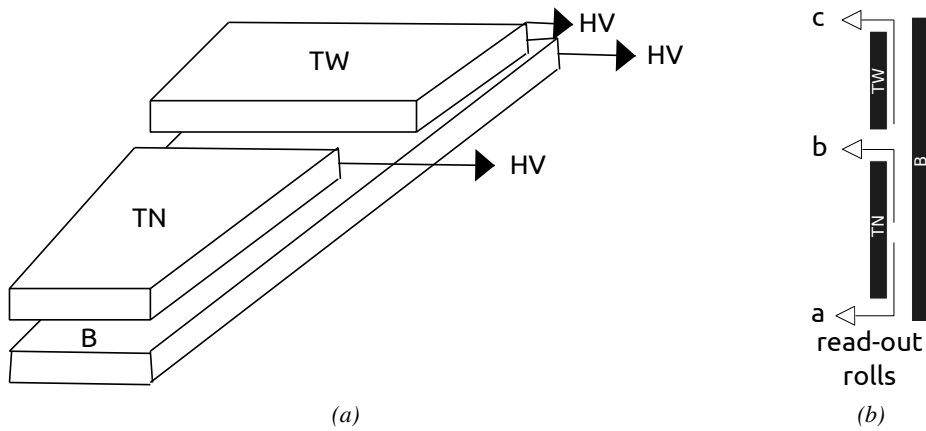


Figure 5.23: Presentation of a double-gap endcap RPC with its three RPC gaps. Due to the partitioning of the read-out strips into three rolls, the TOP layer of gap is divided into two gaps: TOP NARROW (TN) and TOP WIDE (TW). The BOTTOM (B) only consists in one gap.

3860 It is likely that the rates obtained through fitting on normalized values is underestimated. Indeed,
 3861 monitoring the current in the three gaps composing a CMS endcap RPC (Figure 5.23) while knowing
 3862 the rate, the charge deposition per avalanche q_γ can be computed. A current density, expressed in
 3863 A/cm^2 , divided by a rate per unit area, expressed in Hz/cm^2 yields a charge expressed in C. The
 3864 current driven by the RPC is assumed to be due to the irradiation, hence, to the avalanches developing

in the gas volume due to the photons of the Cesium source. On the other hand, the rate is supposed to be a measure of the number of photons interacting with the detector. This way, it comes that the charge deposition per avalanche is expressed like $q_\gamma = J_{mon}/R_\gamma$, with J_{mon} being the monitored current density and R_γ the measured γ rate. The current density is computed as the sum of the current density measured in the top and bottom gap layers, $J_{mon} = (I_{mon}^{TW} + I_{mon}^{TN})/(A_{TW} + A_{TN}) + I_{mon}^B/A_B$, with $A_{B,TN,TW}$ being the active area and $I_{mon}^{B,TN,TW}$ the monitored currents of the gaps. According to Figure 5.24, the charge deposition per avalanche consistently converges to a value of the order of 50 pC for each absorber setting which corresponds to a value more than twice larger than what reported in literature for CMS detectors [271, 272] indicating that the rates could have been wrongly evaluated during the short study performed at GIF. An increase of the γ rate by a factor 2 would actually be consistent with the expected rates calculated in Table 5.4, assuming the sensitivity to γ to be of the order of $(2 \pm 0.2) \times 10^{-3}$.

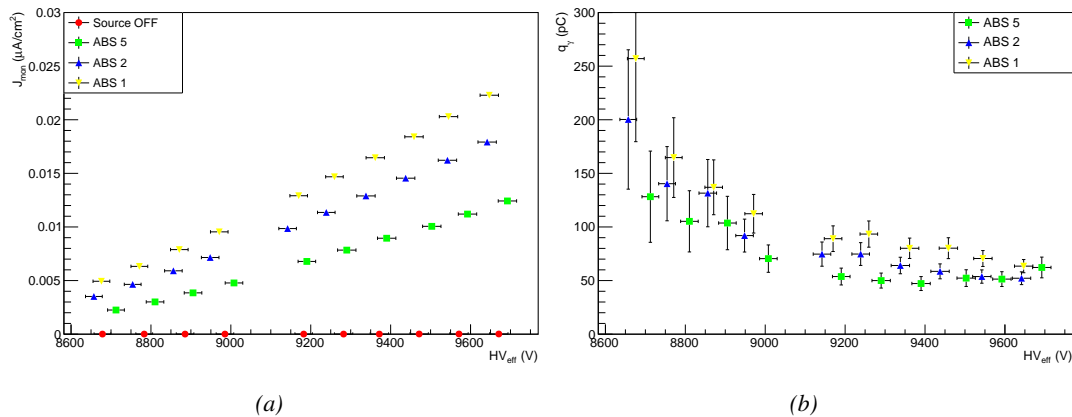


Figure 5.24: Current density (a) and charge deposition per gamma avalanche (a), defined as the current density normalized to the measured rate taken from Figure 5.21a as a function of the effective high voltage in chamber RE-4-2-BARC-161 measured at GIF with Source ON using different absorber settings: ABS 5 (green), ABS 2 (blue) and ABS 1 (yellow).

Overall, working at GIF has been a rewarding experience as it offered CMS RPC R&D team the possibility to start developing the necessary skills and tools that would become the core of GIF++ experiment. The quality of the results can be argued both due to the little robustness of the experimental setup and the lack of available statistics to draw conclusions from, bringing large errors on the final result. The confrontation of the data to known results pointed to a failure in correctly measuring the γ rate at working voltage and, hence, to an overestimation of the charge per avalanche and of the drift of working voltage with increasing rate. Nevertheless, the prototypes of DAQ and offline analysis tools proved to be reliable.

5.3 Longevity tests at GIF++

5.3.1 Selection and characterization of CMS RPCs for longevity at GIF++

In the perspective of future upgrades of LHC that would bring detectors to be operated in a high irradiation environment, the new Gamma Irradiation Facility of CERN was first proposed in 2009 [273].

3889 The Gif++ would thus provide all LHC R&D teams working on behalf of the different LHC experiment
 3890 with a facility to perform longevity studies using a very intense Cesium gamma source.

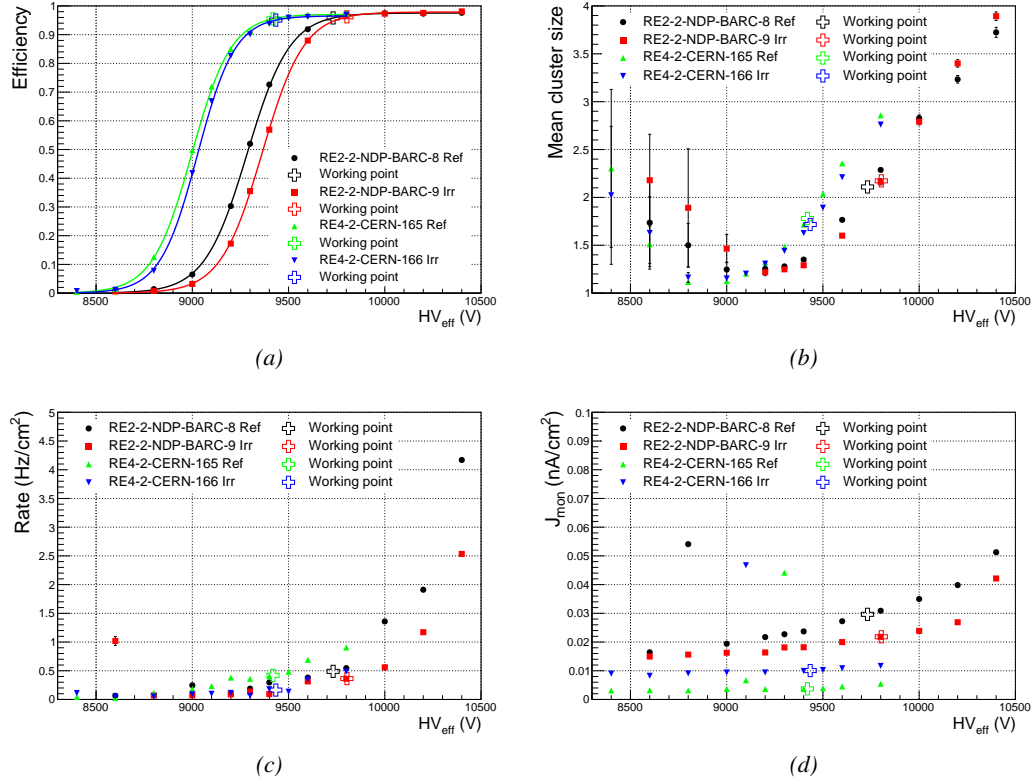


Figure 5.25: Characterization of CMS RPC detectors foreseen to be used at Gif++ for longevity studies of the present system. Using cosmic muons, efficiency (a) and cluster size (b) were measured as well as noise rate (c) and current density (d). For each detector, the working voltage, defined as in Formula 3.25 after LS1, was extracted from sigmoid fits performed in Figure (a) and the values of efficiency, cluster size, noise rate and current density at this voltage are reported using open crosses.

3891 In the specific case of CMS RPC, the longevity studies imply a constant irradiation of selected
 3892 detectors in order to accumulate a charge equivalent to what is expected during HL-LHC, i.e. a
 3893 charge of $0.8 \text{ C}/\text{cm}^2$ according to Figure 5.2 including a safety factor 3. Other detectors are left
 3894 non-irradiated to be used as references. Throughout the irradiation campaign, the performance of
 3895 the irradiated and reference detectors will be periodically probed using the high intensity H4 muon
 3896 beam. Dedicated test beam periods will be used to measure the efficiency and gamma rate at the
 3897 level of the detectors. Different source absorber settings will test the rate capability of CMS RPCs,
 3898 that needs to be certified above $600 \text{ Hz}/\text{cm}^2$. Using a muon beam will also help identifying signs of
 3899 ageing in the case the performance of the irradiated detectors diverges from those of the reference
 3900 detectors with increasing accumulated charge. Other than the performance of the detectors, signs of
 3901 ageing could come from increasing dark current that would be related to local ageing of the elec-
 3902 trodes triggered by the increased hydrofluoric acid (HF) production in an irradiated environment.
 3903 HF is produced by the decomposition of $C_2H_2F_4$ molecules during the charge multiplication pro-

cess and leads to increased dark current and noise in Bakelite RPCs treated with linseed oil. This effect is strongly reinforced by the presence of UV photons [274, 275]. A close monitoring of the current driven by the detectors will then be necessary as well as dedicated periodical electrode resistivity measurements and chromatography analyses on the gas exhaust.

As the maximum background in CMS is found in the endcap disks, the choice was made to focus the GIF++ longevity studies on endcap chambers. Most of the RPC system was installed in 2007. Nevertheless, the large chambers in the fourth endcap (RE4/2 and RE4/3) have been installed during LS1 in 2014. The HPL of these two different productions possibly having slightly different properties, four spare chambers of the present system were selected. From the original CMS RPC system, two RE2/2 spares were selected along two RE4/2 spares from the newest detectors. Having two chambers of each type allowed to always keep one of them non-irradiated as reference. Due to the limited gas flow in GIF++, the RE4 chamber remained non-irradiated until end of November 2016 when the longevity studies could finally be started on those chambers.

The performance of the chambers prior to the start of the longevity campaign was characterized in Ghent before their transportation to CERN for installation in the GIF++. The results of the characterization are showed in Figure 5.25 and summarized in Table 5.5. A clear difference in performance for both types of chambers is observed as the working voltages of the newest chambers, of type RE4, are 300 to 400 V lower to the older chambers indicating that the gap thickness of RE4 detectors could be thinner. This conclusion could as well be supported by the lower cluster size at working voltages that are also smaller in RE4 chambers. Even though the measured currents are low, RE4 detectors draw less current without irradiation than RE2 detectors pointing to a difference in electrode resistivity that were produced at different moments. Efficiency and noise rate levels are of the same order of magnitude for both type of RPCs.

RPC	RE2-2-NPD-BARC-08	RE2-2-NPD-BARC-09	RE4-2-CERN-165	RE4-2-CERN-166
Used as	Reference	Irradiation	Reference	Irradiation
HV_{WP} (V)	(9732 ± 6)	(9803 ± 6)	(9419 ± 5)	(9434 ± 5)
Efficiency at WP	(96.2 ± 0.3)	(96.6 ± 0.3)	(95.9 ± 0.3)	(95.5 ± 0.3)
Cluster size at WP	(2.19 ± 0.04)	(2.27 ± 0.05)	(1.88 ± 0.04)	(1.80 ± 0.04)
Noise at WP (Hz/cm ²)	(0.51 ± 0.01)	(0.39 ± 0.01)	(0.44 ± 0.00)	(0.15 ± 0.01)
J^{WP} (pA/cm ²)	(30.1 ± 0.1)	(22.2 ± 0.1)	(3.8 ± 0.0)	(10.2 ± 0.0)

Table 5.5: Summary of the characterization measurement performed in Ghent on CMS RPC detectors foreseen to be used at GIF++ for longevity studies of the present system. For each detector, the working voltage, defined as in Formula 3.25, was extracted from sigmoid fits performed in Figure 5.25a. The values of efficiency, cluster size, noise rate and current density at this voltage are reported.

5.3.2 RPC test setup

For an easy manipulation of the detectors, a trolley with a structure containing slots in which the RPCs can be slid vertically was used and is referred to as T1. When in position, each chamber is in a plane perpendicular to the beam line and the source flux as can be seen through Figure 5.26, and receives a uniform irradiation. Moreover the trolley allows for easy movement of the system. Indeed, the position of the trolley varies according to the specific measurements that are being done.

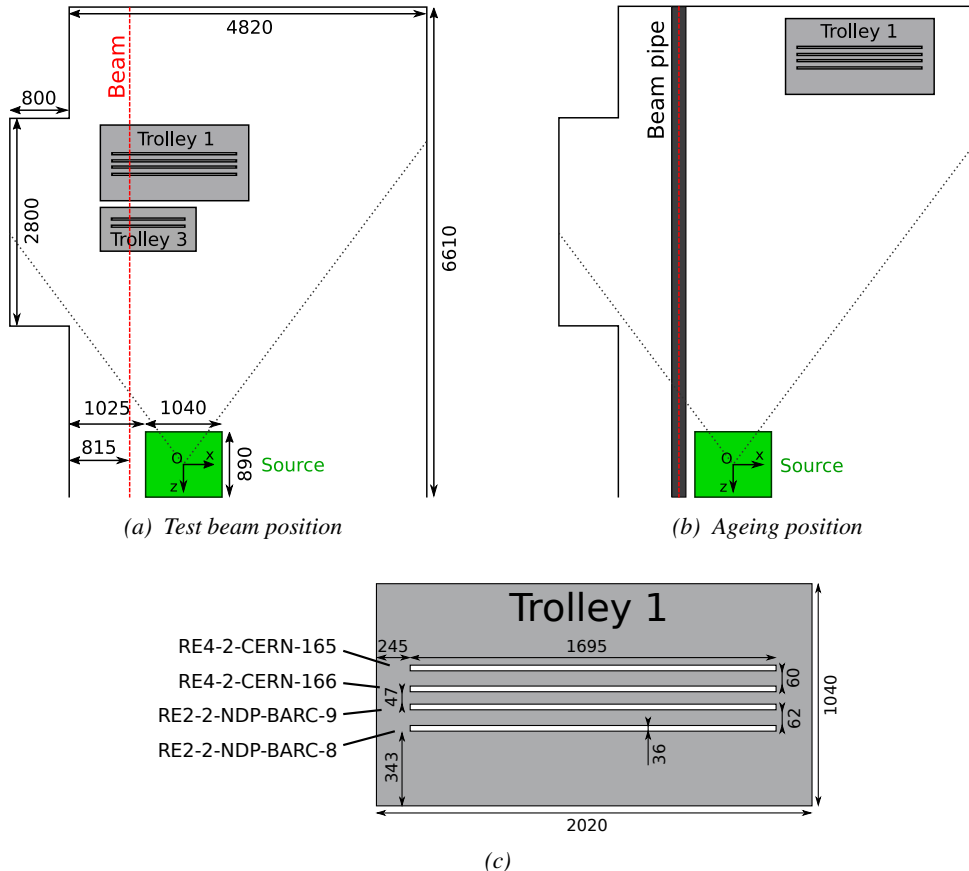


Figure 5.26: CMS RPC setup inside the GIF++ bunker during test beam (a) and ageing periods (b). The space in between the RPCs and the source is usually used by other detectors while the space in between T1 and the upstream wall is not filled. Due to the presence of the beam pipe, the trolley is moved away from the beam line during irradiation periods and placed further away from the source for less intense irradiation. The position of the trolley can vary due to the use of the space by other setups and is then not exact. Nonetheless, the position of the chambers in the trolley is fixed and given in Figure (c).

During the dedicated test beam periods, the GIF++ experiments are in control of the muon beam. The trolley is placed in the upstream region of the bunker, in the beam line at a distance of generally 3.4 m from the source, as described through Figure 5.26a. At this distance, the simulated gamma current is the order of $5 \times 10^6 \text{ cm}^{-2} \text{ s}^{-1}$. The CMS RPC detectors are the furthest away from the source as other detectors need to be certified at higher background rates. Depending on the needs of the other experiments at the GIF++, the trolley position of the trolley can be pushed as far as 4.1 m from the source. An additional trolley, referred to as T3, contains iRPCs and is placed between the source and the T1 trolley. Indeed, iRPCs need to be certified at higher rates and thus need to be placed closer to the source to receive a stronger irradiation using the same absorber settings. The space on T1 being limited, the tracking RPCs used for extra offline information during the analysis are placed on the same trolley as the iRPCs. They are kept at full efficiency at all time to reconstruct muon tracks and to correlate them with hits recorded in T1 chambers. The beam trigger system is composed of three scintillators. Two are placed outside on each side of the bunker and of the third scintillator is placed in the beam line in between T1 and the wall.

3947 Most of the year, outside of these test beam periods, T1 is placed in the so called *ageing position*
 3948 corresponding to the furthest position at approximately 4.7 m from the source outside of the beam
 3949 line before August 2019. At such a distance, the simulated gamma current is the order of 3×10^6
 3950 $\text{cm}^{-2} \text{s}^{-1}$. Following the extension of the upstream area in August 2019, the trolley was pushed
 3951 approximately 1 m away at a distance of 5.7 m to the source, corresponding to a simulated gamma
 3952 current of the order of $2 \times 10^6 \text{ cm}^{-2} \text{s}^{-1}$. During periods where GIF++ doesn't have the control of
 3953 the beam, the beam line needs to stay clear so that a beam tube can be installed through the bunker,
 3954 as can be seen in Figure 5.26b. The reason for placing the chambers as far as possible from the
 3955 source comes from the too high irradiation delivered by the source during the irradiation periods
 3956 where all the other groups having placed detectors in the bunker require as much charge integration
 3957 as possible. Hence, the source is operated without any absorbers. On the contrary, during the test
 3958 beam periods, all the groups working in GIF++ are interested in operating the source using various
 3959 absorber settings to study the performance of their detectors under different irradiation conditions.
 3960 T1 RPCs are kept at a stanby voltage of 6500 V when the other groups need to work with ABS 1
 3961 due to the proximity of the trolley to the source compared to ageing periods.

3962 From the bunker area, long cables and pipes running through the wooden floor connect the de-
 3963 tectors to the service area, visible in Figure 5.6. The service area hosts all the high and low voltage
 3964 power supplies, the TDCs and computers used for data acquisition and preliminary offline analysis.
 3965 The gas system required for the gaseous detectors installed in GIF++ can also be found in the service
 3966 area [276].

3967 The detectors read-out is, as in the case of GIF, connected to V1190A VME TDCs communicating
 3968 with the DAQ computer via a V1718 VME bridge manufactured by CAEN. At the end of each data
 3969 tacking, the preliminary analysis is run to fill the Detector Control Software webpage, referred to as
 3970 WebDCS, with Data Quality Monitoring (DQM) histograms. The WebDCS is a custom made DCS
 3971 application for the specific case of GIF++ RPCs. It provides online information about the environ-
 3972 mental parameters in the bunker as well as the state of each detector. A constant monitoring of
 3973 all the environmental parameters, in different points of the bunker area, gas parameters, to control its
 3974 composition, temperature and pressure, and of the voltages and currents delivered by the power sup-
 3975 plies is performed and displayed on the homepage of the WebDCS interface. Moreover, it contains
 3976 the database with all the RPC data in the form of ROOT files and of summary hisograms. Hence, it
 3977 is a useful tool for the shifters on duty in the control room located farther in the building, away from
 3978 the beam lines.

3979 5.3.3 GIF++ data flow

3980 At GIF++, the CMS RPC R&D setup collects different types of data from the detector monitoring
 3981 parameters, such as voltage and currents, the gas, source, and environmental parameters, and, of
 3982 course, the TDC data related to the actual muon and gamma measurements. These different data
 3983 sources correspond to three different data flows as presented in Figure 5.27.

3984 The *Data Interchange Protocol (DIP)* flow, DIP being a communication system allowing for
 3985 exchange of real-time information between systems [277], concerns all the data coming from the
 3986 gas composition, temperature and humidity, the environmental temperature and pressure, the source
 3987 settings and the radiation monitoring sensors. At the experimental area, all data of interest for all of
 3988 the users of the facility (source settings, radiation monitoring, gas composition at the exit of the gas
 3989 mixer and general environmental information) are measured, distributed and also stored in the data
 3990 of the experimental hall where is located the GIF++. Access to the database is done through DIP

3991 communication. The measurement of more specific data such as gas flow, temperature and humidity
 3992 at the level of the detectors (upstream and downstream of the detectors) as well as environmental
 3993 parameters has to be arranged by the users themselves. For this reason, several pressure, tempera-
 3994 ture and humidity sensors were installed on the gas distribution system of the RPC trolleys. The
 3995 corresponding data flow, although not related to DIP itself, is saved together with the DIP data into
 3996 the local CMS RPC database and displayed on the front page of the WebDCS. In the case any of
 3997 the measured values go out of their optimal range, the WebDCS will produce corresponding alerts.
 3998 The data are particularly important to perform the PT correction described in Section 3.4 of Chap-
 3999 ter 3 and to stabilize the effective voltage of the detectors. Monitoring history plots are made using
 4000 JavaScript are also displayed for easy access to past information, as shown in Figure 5.28.

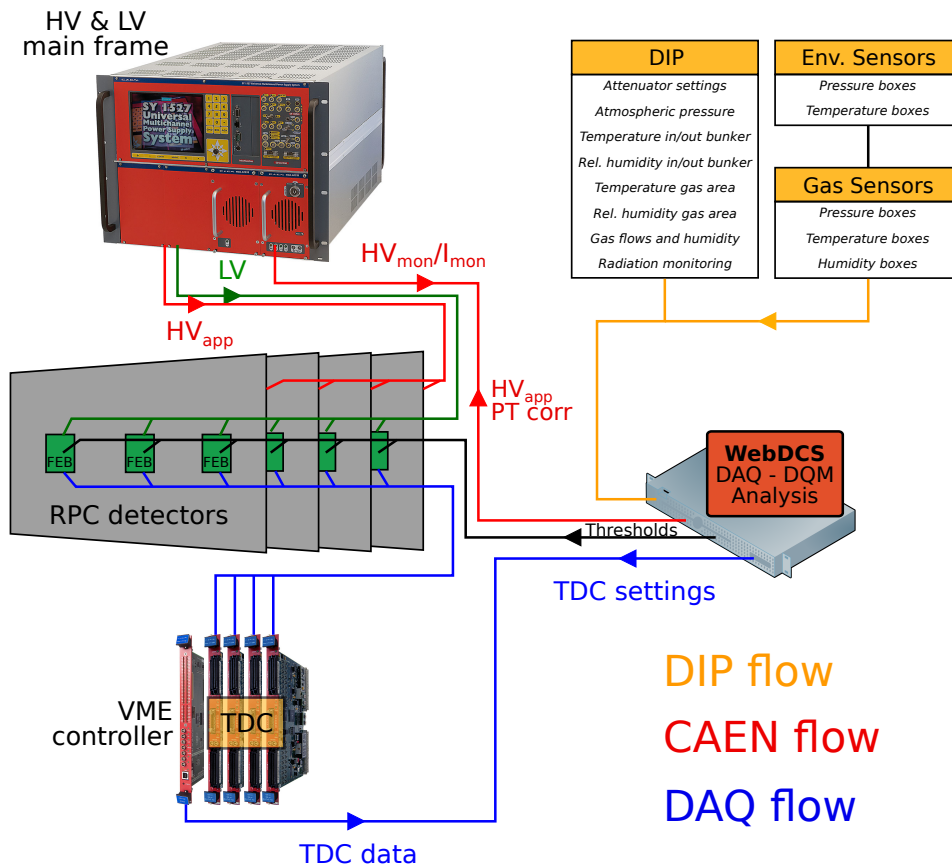


Figure 5.27: Visualisation of the main data flows in the CMS RPC setup at the Gif++. The yellow flow lines correspond to the DIP flow used for source, environmental and gas information. The red flow lines are for the CAEN flow through which the WebDCS communicates the voltages to be applied on the detectors using pressure and temperature information and retrieves the monitored voltages and currents. Finally, the blue flow lines correspond to the DAQ flow through which the RPC data is collected from the TDCs by the computer.

4001 The data flow related to the monitoring of the detector high voltages and currents, referred to
 4002 as *CAEN flow* as a reference to the manufacturer of power supplies, is handled through direct com-
 4003 munication between the DAQ computer and the power supply main frames. Finally, the DAQ flow
 4004 concerns all data acquired through the use of the TDCs, i.e. all the muon or gamma event data

4005 recorded by the detectors under test at GIF++. It was already discussed that when a trigger signal is
 4006 sent to a TDC module, the TDC saves all of the data located in a certain time window set around the
 4007 time stamp of the signal. The trigger signal in the case of GIF++ can be a coincidence of the trigger
 4008 scintillators or a signal from a pulse generator. The DAQ computer extracts from the TDC buffers the
 4009 list of fired channels and of associated time stamps for each trigger signal. The data is then used to
 4010 reconstruct muon tracks along the CMS RPC setup at the GIF++ or to compute the noise and gamma
 4011 rates associated to a certain source setting.

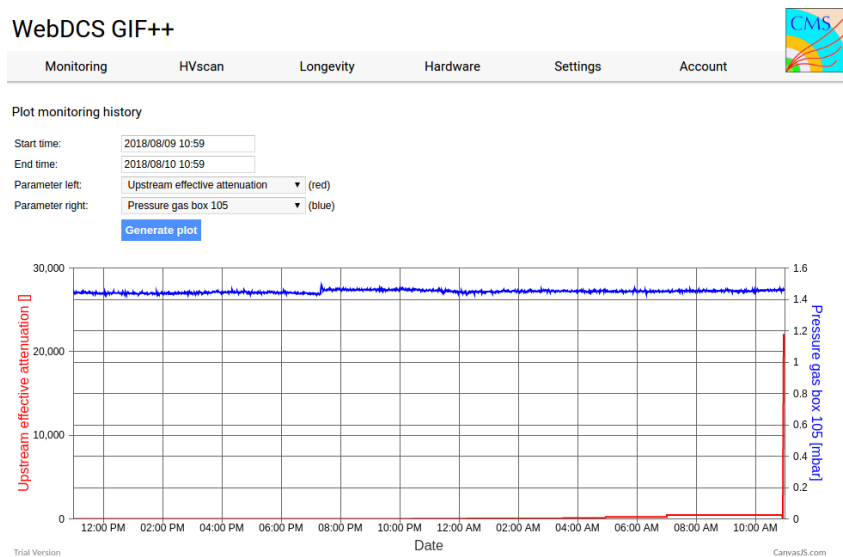


Figure 5.28: DIP monitoring history accessed through the GIF++ WebDCS interface.

4012 5.3.4 Measurements performed during beam periods

4013 As previously described, two types of measurements are performed on the chambers during beam
 4014 periods. On the one hand, it is interesting to measure the efficiency of the RPCs with increasing
 4015 voltage with different source absorber settings but on the other hand, it is important to correlate the
 4016 efficiency information to the gamma rate seen by the chambers at the different voltages. The choice
 4017 was made to separate efficiency measurements from rate measurements to better manage time and
 4018 data volume. In both cases, TDC data recorded during so called *HV scans* is divided into *runs*, one
 4019 for each high voltage point, whose data is stored into ROOT files. The TDC settings used during
 4020 both these scans as well as the ROOT data structure are detailed in Section A.4.2 of Appendix A.

4021 The goal of both efficiency and rate scans is to measure the rate capability of the detectors but
 4022 also to monitor any degradation of the performance due to ageing. This way, during test beam
 4023 periods the efficiency and corresponding gamma background are measured to correlate the evolution
 4024 of rate capability at different stages of irradiation. In the absence of other signs of ageing, a reduction
 4025 of the rate capability could be related to an increase of the electrodes resistivity.

4026 5.3.4.1 Efficiency scans

4027 The HV scans performed to specifically measure
 4028 the muon detection efficiency under different
 4029 irradiation conditions follow a standard-
 4030 ized procedure. Data using the DAQ is taken
 4031 at the same 12 HV points for all chambers,
 4032 ranging from 9 kV to 10.1 kV in steps of
 4033 100 V. For each HV run, a minimum of 5000
 4034 muon beam triggers, provided by the coinci-
 4035 dence of the three scintillators, is required in
 4036 order to accumulate enough statistics for a re-
 4037 liable computation of the efficiency of the de-
 4038 tectors. In addition to the four RPCs held on
 4039 T1, two tracking RPCs installed on T3 are
 4040 kept at a fixed voltage of 9.7 kV to provide
 4041 the analysis software [278] with beam position
 4042 information to exclude off-track signals.
 4043 The tracking RPCs are double gap detectors
 4044 featuring 2 mm HPL electrodes and 2 mm gas
 4045 gaps. They are prototypes built by the ital-
 4046 ian company *General Tecnica* using a different
 4047 production of HPL. Finally, the monitored cur-
 4048 rents and voltages are recorded in histograms
 4049 along with the TDC data in a different ROOT
 4050 file for each run.

4051 HV scans are taken for different source
 4052 settings as the goal is to irradiate all the de-
 4053 tectors with a minimal rate of 600 Hz/cm².
 4054 Usually, a full study of the performance of the
 4055 detectors is performed with Source OFF, and
 4056 then with nine absorber settings that attenu-
 4057 ate the nominal gamma flux by factors from
 4058 more than 200 to only 3, where settings with
 4059 fully opened source are avoided with RPCs
 4060 in test beam position. During the efficiency
 4061 scans, the cluster size is also measured and the
 4062 currents are monitored as can be seen in Fig-
 4063 ure 5.29.

4064 5.3.4.2 Rate scans

4065 The background measurements are performed using a similar HV scan procedure as for the efficiency
 4066 measurements. The HV scan in test beam periods is taken at fewer HV points compared to the
 4067 efficiency scans as the region of interest is located around the knee and efficiency plateau of the
 4068 detectors, i.e. these scans are performed only on six HV points ranging from 9.5 kV to 10 kV. The
 4069 value of the rate at the operating voltage is then deduced from the efficiency scan through linear

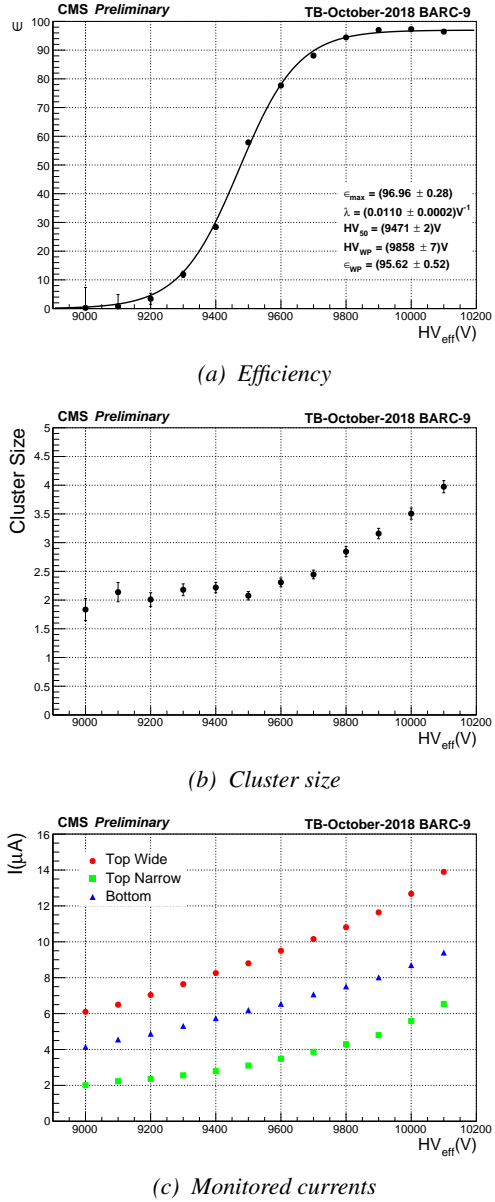


Figure 5.29: Example of results obtained during an efficiency scan performed with ABS 113 (4.6) during October 2018 testbeam period.

4070 interpolation. A good estimation of the rate requires a long enough integrated time of the TDC data.
 4071 The way data is collected, detailed in Appendix A, makes the DAQ search for data stored in the TDC
 4072 buffers prior to the trigger signal. The time window from which the data can be collected ranges from
 4073 25 ns to more than 50 μ s. With the Cesium source delivering a constant gamma flux, it was decided
 4074 that a total integrated time of 0.2 s would be enough to have a reliable calculation of the gamma
 4075 rate. This is achieved by taking 20,000 random trigger pulses delivered by a pulse generator at a
 4076 frequency of 300 Hz while extracting 10 μ s of data from the buffers for each trigger. An example
 4077 of the data obtained during rate scans is showed in Figure 5.30 in which the hit multiplicity at a
 4078 single HV step of a scan, used to compute the rate per unit area, is showed together with the rates as
 4079 computed at every HV steps.

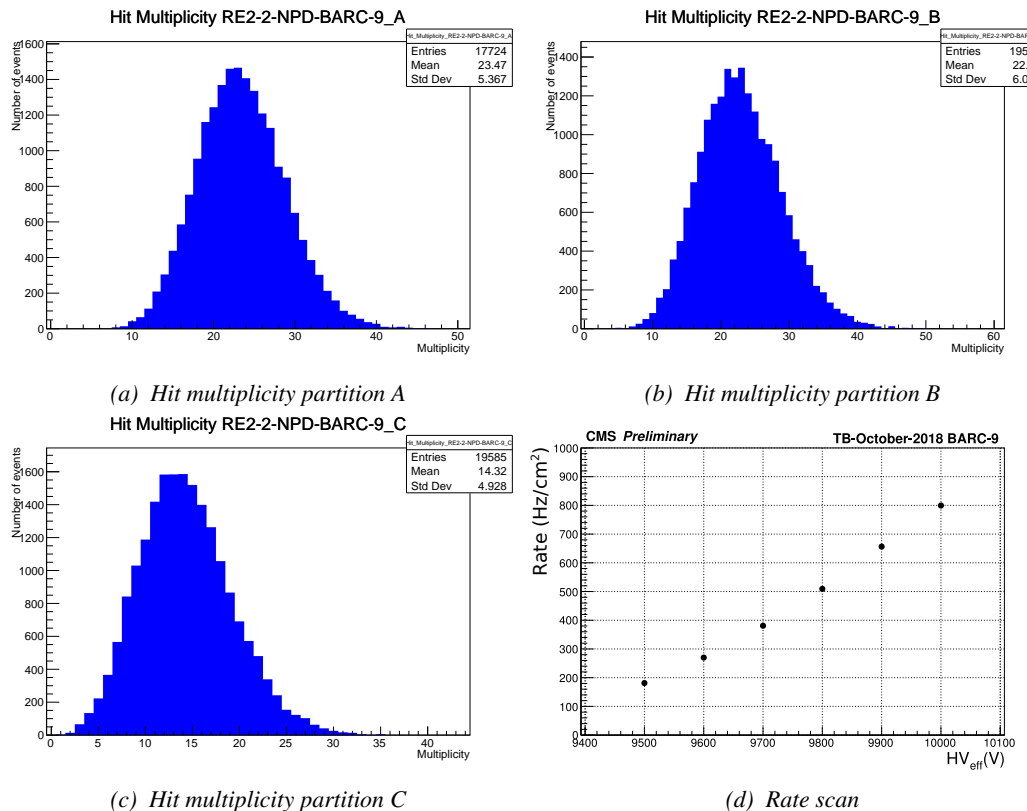


Figure 5.30: Example of results obtained during an efficiency scan performed with ABS 113 (4.6) during October 2018 testbeam period. The hit multiplicity histograms (a), (b) and (c) correspond to the fourth HV point of the scan at 9800 V.

4080 Separating the rate and efficiency measurements was motivated by the inconsistency of the muon
 4081 beam provided in Gif++². Using periods without beam to measure rates with a good statistics allows
 4082 for faster study programs. Moreover, the number of muons per beam spill depends strongly on the
 4083 user setups placed upstream of the Gif++ and on the specific beam optic magnet settings. Collecting

²During test beam periods, the delivery of the muon beam at the SPS North Area depends on the LHC program. As the SPS is used to feed the LHC with accelerated protons, the priority is given to the LHC. Other than the LHC, the delivery of muon beams can also be stopped due to maintenance or breakdown on the acceleration lane. This may translate into long periods with low intensity beams or even without any beam at all.

4084 20,000 events could then take too long for the other users at the Gif++. Hence, efficiency scans are
 4085 performed with lower statistics, and the time window from which the TDC data are extracted is
 4086 strongly reduced (400ns for efficiency scans versus 10 μ s for rate scans) to keep the data size to its
 4087 bare minimum.

4088 **5.3.4.3 Offline analysis and Data Quality Monitoring**

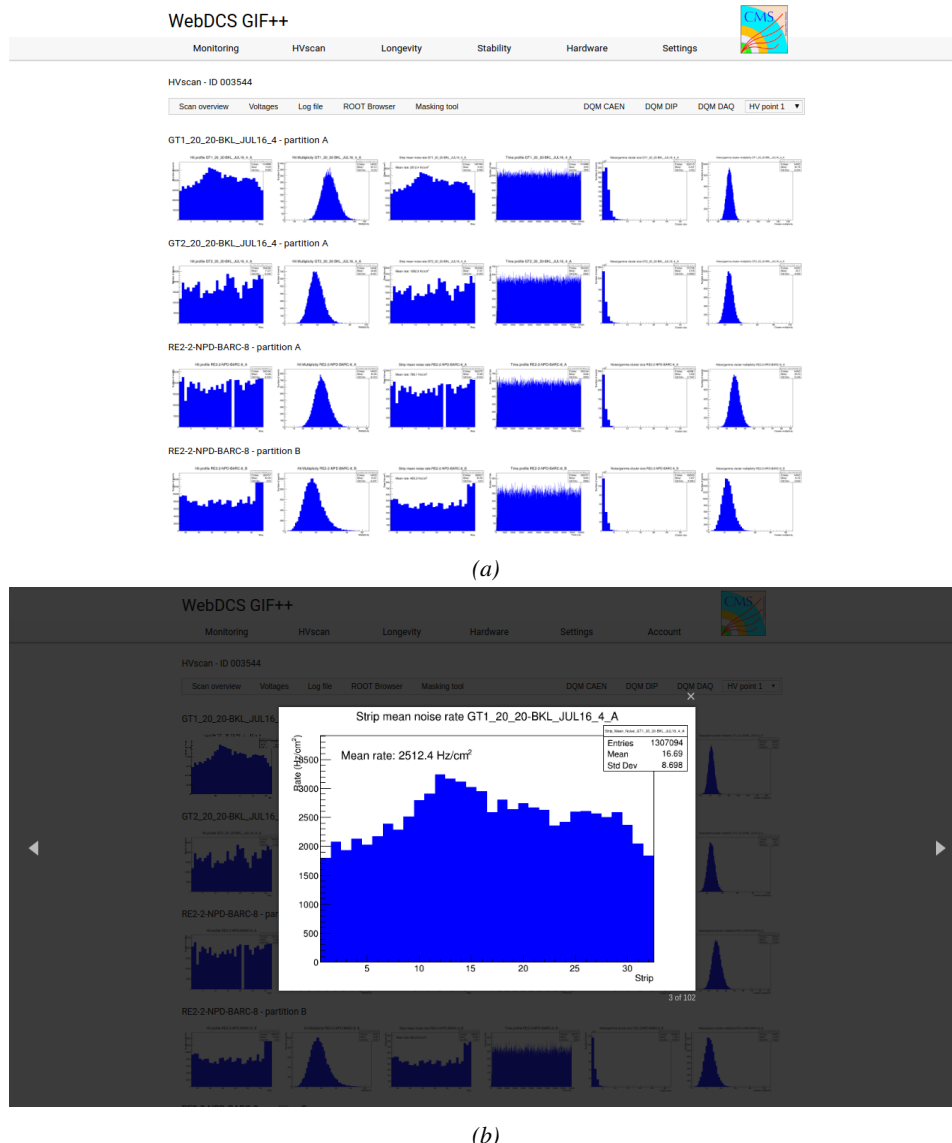


Figure 5.31: Example of DQM page available on CMS RPC WebDCS at the Gif++: the histogram of the rate measured in one of the tracking chambers, namely GT1_20_20_BKL_JUL16_4, is selected and displayed above the page.

4089 The data recorded during efficiency and rate scans always consists of two ROOT files per run, where
 4090 each run corresponds to a certain HV point. One of the files contains the TDC data, a collection
 4091 of hits and time stamps per active channel on the read-out of the RPCs, while the second is the
 4092 CAEN main frame data, i.e. the detector currents and high voltages. The data are systematically
 4093 analysed at the end of each scan using the Offline Analysis tool of GIF++, detailed in Appendix B,
 4094 that produces histograms such as hit, rate and time profiles, hit multiplicities, gamma cluster sizes or
 4095 multiplicities for the DQM display of the WebDCS, as shown in Figure 5.31. More histograms can be
 4096 accessed through the ROOT browser included in the WebDCS, as shown in Figure 5.32. Moreover,
 4097 the analysis performed with the Offline tool provides final results for the rate scans. On the contrary,
 4098 the algorithm for efficiency calculation is kept simple and approximative in the tool. Including
 4099 tracking into the analysis requires manual adjustment for each individual scan as the positions of the
 4100 trolleys with respect to each other may vary.

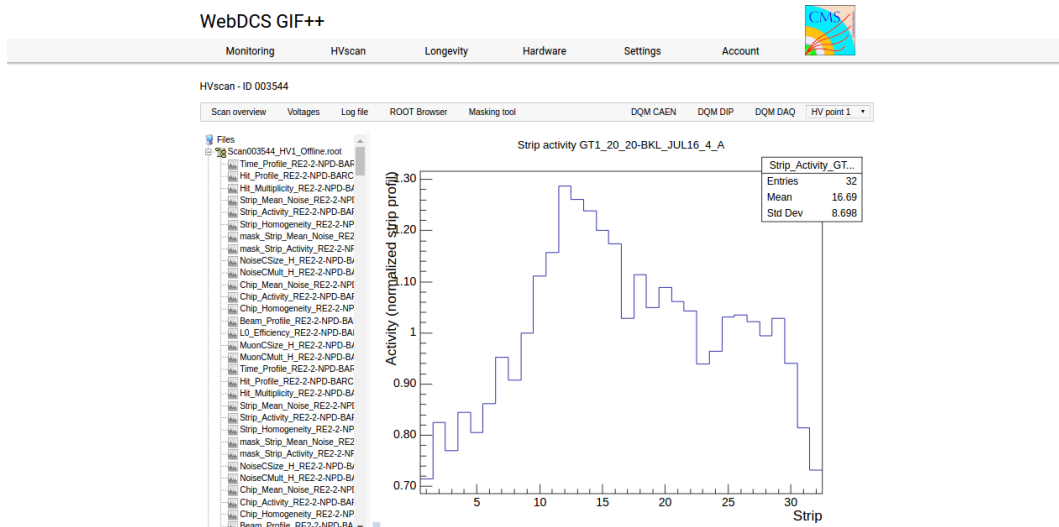


Figure 5.32: Example of DQM ROOT Browser page available on CMS RPC WebDCS at the GIF++: the strip activity profile, defined as the rate profile normalized to the mean rate, in one of the tracking chambers, namely GT1_20_20-BKL_JUL16_4. Available ROOT files and histograms can be browsed thanks to the left panel showing the directory and files structures.

4101 5.3.5 Measurements performed during irradiation periods

4102 Even though test beam periods are stressful times as an extensive data taking program needs to
 4103 be finalized in a short amount of time, the biggest amount of data actually comes from irradiation
 4104 periods. Indeed, when T1 is moved back to its ageing position in between each test beam periods,
 4105 data is recorded at any time the source can be switched ON for irradiation. Other experiments in the
 4106 area might prevent the source from staying open continuously. As an example, the time efficiency
 4107 of irradiation of CMS RPC detectors in GIF++ is presented in Figure 5.33.

4108 Several types of measurement are performed throughout the irradiation period. As long as the
 4109 detectors are being irradiated, a monitoring of the currents is performed to evaluate the corresponding
 4110 integrated charge over the total irradiation time. Moreover, in order to spot any signs of ageing, the

4111 gamma rates seen by the chambers at the chosen source absorber setting as well as the noise rates
 4112 and dark currents are periodically measured. During irradiation periods this is looked at every week
 4113 via HV scans performed at various source settings. The weekly scans involve both the irradiated but
 4114 also the reference chambers, providing with a weekly monitoring of the evolution of the irradiated
 4115 chambers noise, gamma rate and dark current. Measuring with all detectors at the same time also
 4116 allows getting rid of potential systematics that might make the rates (noise or gamma) vary from one
 4117 measurement to another. If such systematic effects occur, they will be observed in all detectors.

4118 Finally, the resistivity is measured periodically during the year, generally before or after test
 4119 beam periods, by the use of Argon breakdown technique. The method consists in filling the detector
 4120 volume with Argon instead of the CMS standard gas mixture and to increase the voltage while
 4121 monitoring the current. Beyond an electric field of about 1 kV mm^{-1} at the GIF++ environmental
 4122 conditions, Argon turns into a conductive plasma and does not offer electric resistance anymore. The
 4123 monitoring of the currents beyond the breakdown voltage can then be used to calculate the resistivity
 4124 of the electrode material.

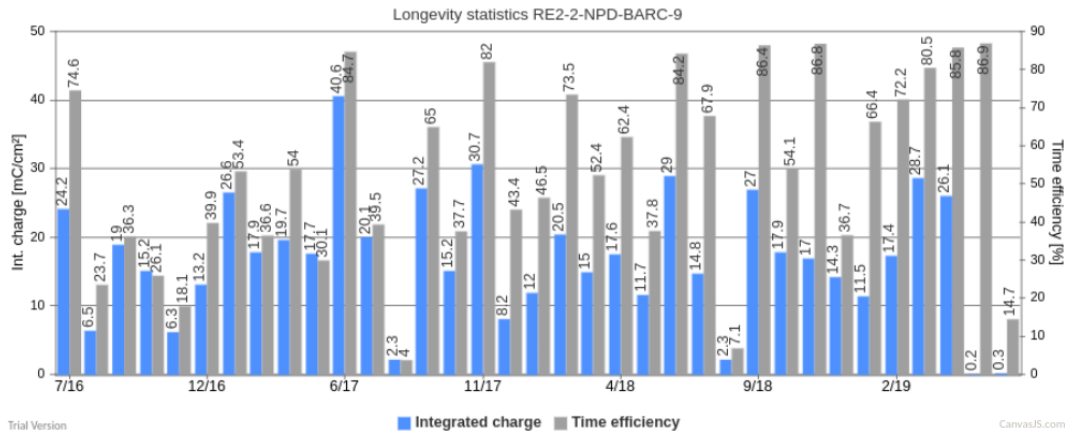


Figure 5.33: Longevity data for chamber RE2-2-NPD-BARC-9 in GIF++. For each month since July 2017, the integrated charge (in blue) as well as the time efficiency of irradiation (in gray) is reported.

4125 5.3.5.1 Longevity scans

4126 The main activity of irradiation periods consists of the *longevity scans* during which the currents of
 4127 the irradiated chambers are continuously monitored. The two irradiated chambers, RE2-2-NPD-BARC-09
 4128 and RE4-2-CERN-166, are both brought to a voltage of 9.8 kV while the source flux can vary de-
 4129 pending on the needs of the groups using the facility. The currents are monitored for each active
 4130 gas volume as can be seen in Figure 5.34. The integrated charge for each individual gas volume
 4131 is computed by integrating through time the current density, current normalised to the surface area,
 4132 flowing through each gap, as shown in Figure 5.35.

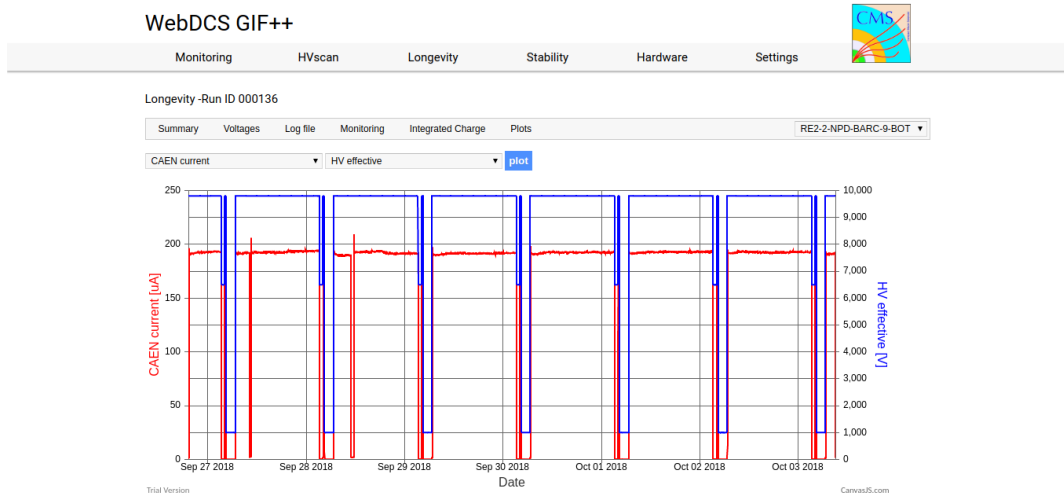


Figure 5.34: Example of a longevity scan monitoring page available on CMS RPC WebDCS at the GIF++: the current and effective voltage, as well as environmental parameters, are monitored for the bottom gap of chamber RE2–2–NPD–BARC–9. The decrease of current is related to a decrease of the voltage due to the daily rate scan procedure or to periods during which the source was turned OFF.

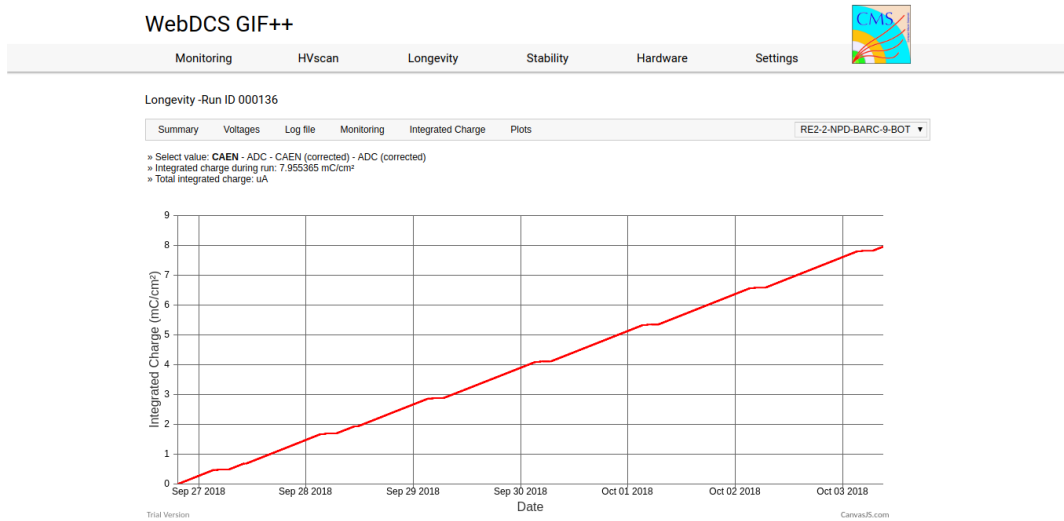


Figure 5.35: Example of a longevity scan summary page available on CMS RPC WebDCS at the GIF++: the integrated charge is computed for the bottom gap of chamber RE2–2–NPD–BARC–9.

Finally, at the end of each longevity scan each gap contribution is translated into the mean chamber integrated charge. The integrated charge accumulated in each chamber is used to update the

4133
4134

4135 summary plots providing the collaboration with official results to be spread as can be seen from
 4136 Figure 5.36. The translation from individual gap currents to total integrated charge in the chamber
 4137 is done using Equation 5.5, where the equation to compute the monitored current density already
 4138 mentioned in Section 5.2.4 is recalled.

$$(5.5) \quad J_{mon} = \frac{I_{mon}^{TW} + I_{mon}^{TN}}{A_{TW} + A_{TN}} + \frac{I_{mon}^B}{A_B}$$

$$Q_{int} = \int_{t_i}^{t_f} J_{mon} dt$$

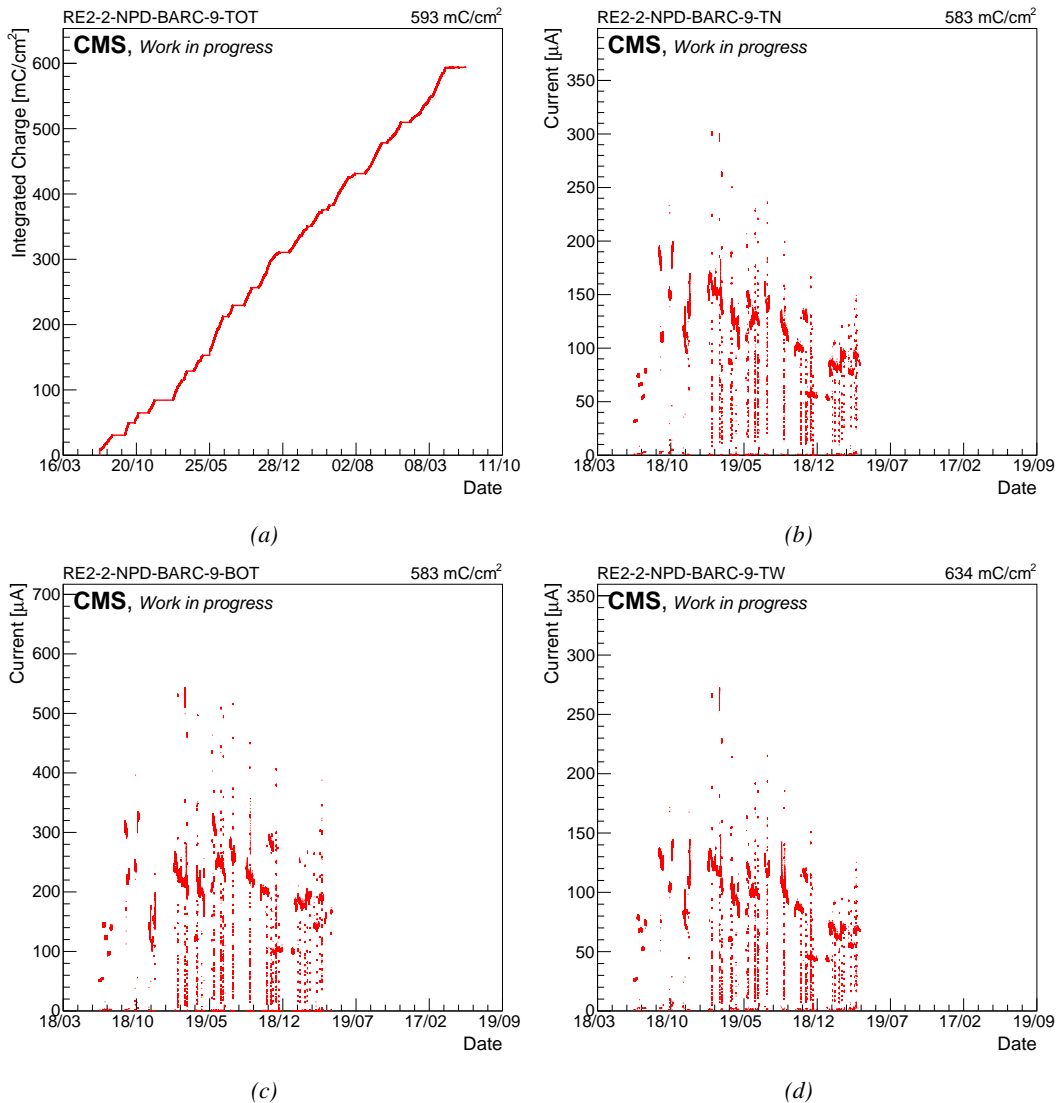


Figure 5.36: Example of current monitoring summary (top wide (a), top narrow (b) and bottom (c) gap currents) and of corresponding integrated charge (d) of chamber RE2-2-NPD-BARC-09.

4139 5.3.5.2 Daily rate monitoring scans

4140 Every night during longevity scans, the setup performs *daily rate scans*. These scans aim at keeping
4141 track of the gamma rate measured in the irradiated RPCs during longevity scans, but are also used
4142 to measure the noise rate at standby voltage for each gap. The procedure for these HV scans consist
4143 of nine runs for which 50,000 random triggers are accumulated, corresponding to 0.5 s of total
4144 integrated time.

4145 1- All gaps are first left at the irradiation voltage of 9.8 kV to measure the gamma rate.

4146 2- Then all gaps are brought to the standby voltage of 6.5 kV to measure the noise rate of the full
4147 detectors.

4148 3- Both top gaps (TW and TN) are brought to a voltage equivalent to an OFF status, i.e. 1 kV so
4149 that the noise contribution of only the bottom gap at standby voltage can be measured.

4150 4- The bottom gaps are ramped up toward the working voltage of 9.8 kV to measure their contri-
4151 bution to the gamma rate estimation.

4152 5-8 The steps 3 and 4 are repeated on TN and then on TW, keeping the bottom and the top gap
4153 which is not of interest at a voltage of 1 kV. This way, the individual contribution to the noise
4154 and gamma rates are known.

4155 9- Both TW and TN are brought to working voltage while the bottom gap is left at 1 kV to
4156 measure the gamma rate for the full top layer at once.

4157 Finally, the voltages of all gaps are brought back to working voltage for the longevity program to
4158 continue until the next daily scan. These scans are responsible for the drop of voltages and currents
4159 observed in Figure 5.34. The procedure previously described is highlighted in Figure 5.37.

4160 Similarly to the efficiency and rate scans taken during test beam periods, the data is here stored
4161 in two separate ROOT files for the TDC and CAEN data for each run. At the same time, the currents
4162 are still monitored by the longevity scan and saved into the GIF++ database for an easy evaluation
4163 of the currents to the integrated charge. The Offline Analysis tool then provides the DQM page with
4164 histograms, and daily values can be compiled into long term monitoring plots to study the variations
4165 of rate and current with increasing integrated charge, as presented in Figure 5.38. The variations
4166 of the rate and current are correlated and correspond mainly to change of source irradiation, gas
4167 flow, gas humidity, or environmental conditions. The rates on every single read-out channel are
4168 also tracked to control their activity with increasing integrated charge and, this way, understand
4169 the appearance of hot spots through noisy channels, as shown in Figure 5.39. The activity of a
4170 strip is defined as the rate of the individual channel normalized to the mean rate measured in the
4171 corresponding read-out partition.

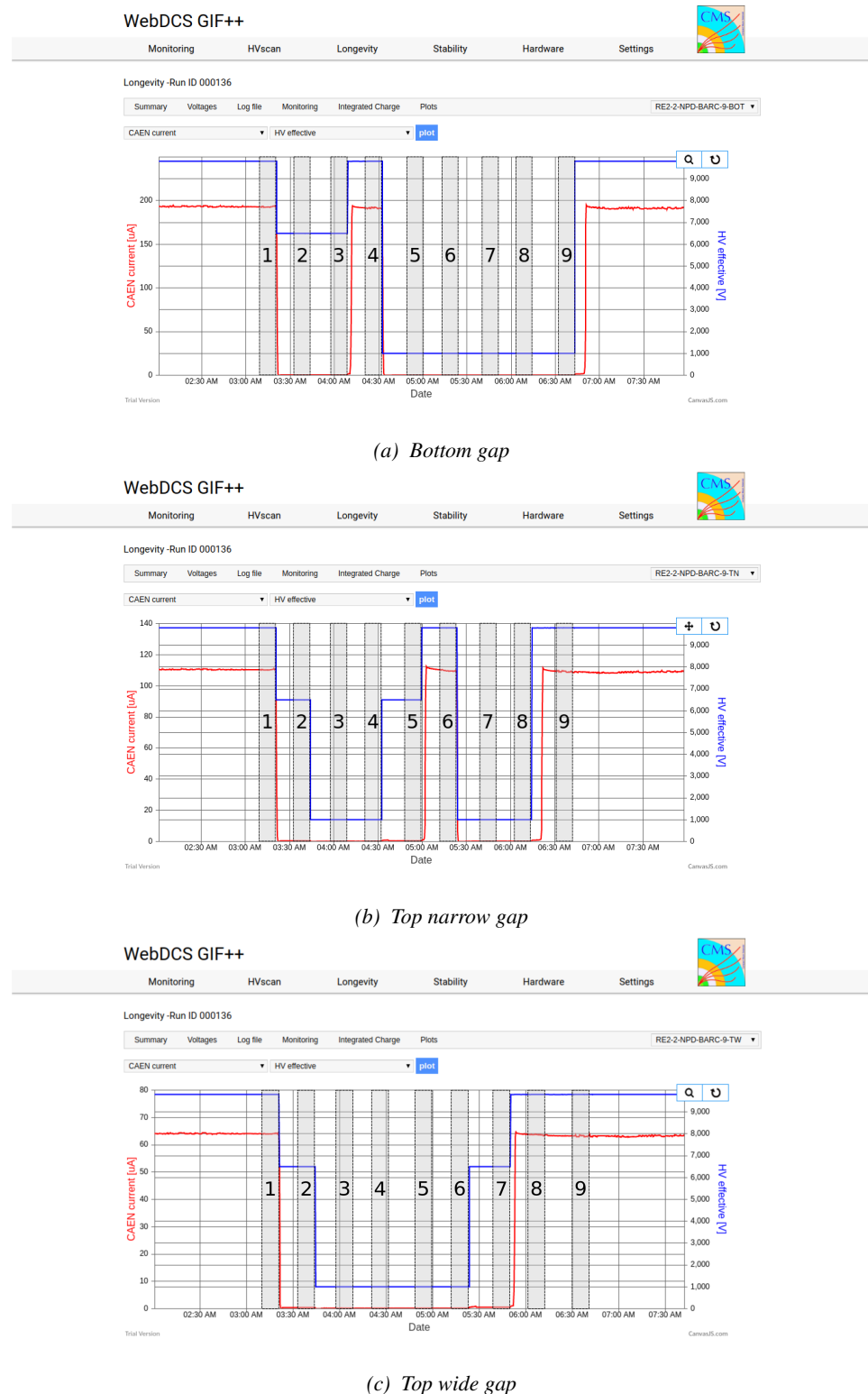


Figure 5.37: Example of daily scan procedure of chamber RE2-2-NPD-BARC-09 with highlighted runs on the CMS WebDCS at the GIF++.

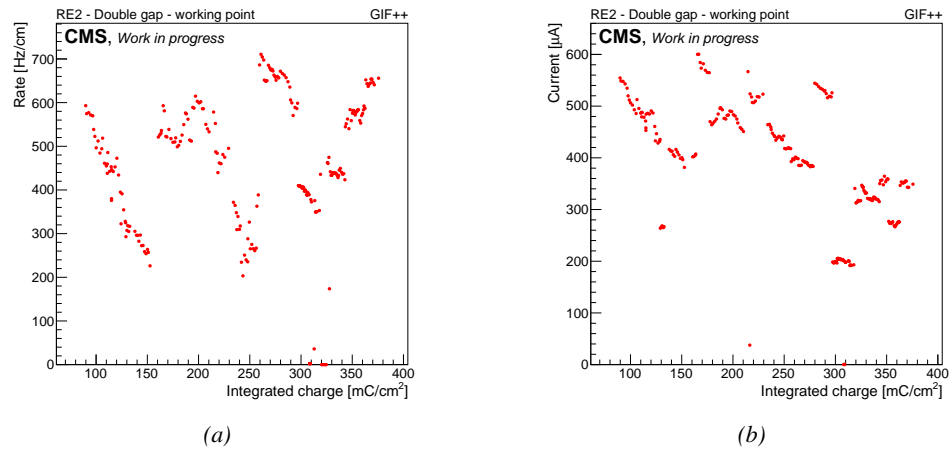


Figure 5.38: Example of rate (a) and current (b) monitoring of chamber RE2-2-NPD-BARC-09 at working voltage in double gap mode (step 1) with increasing integrated charge.

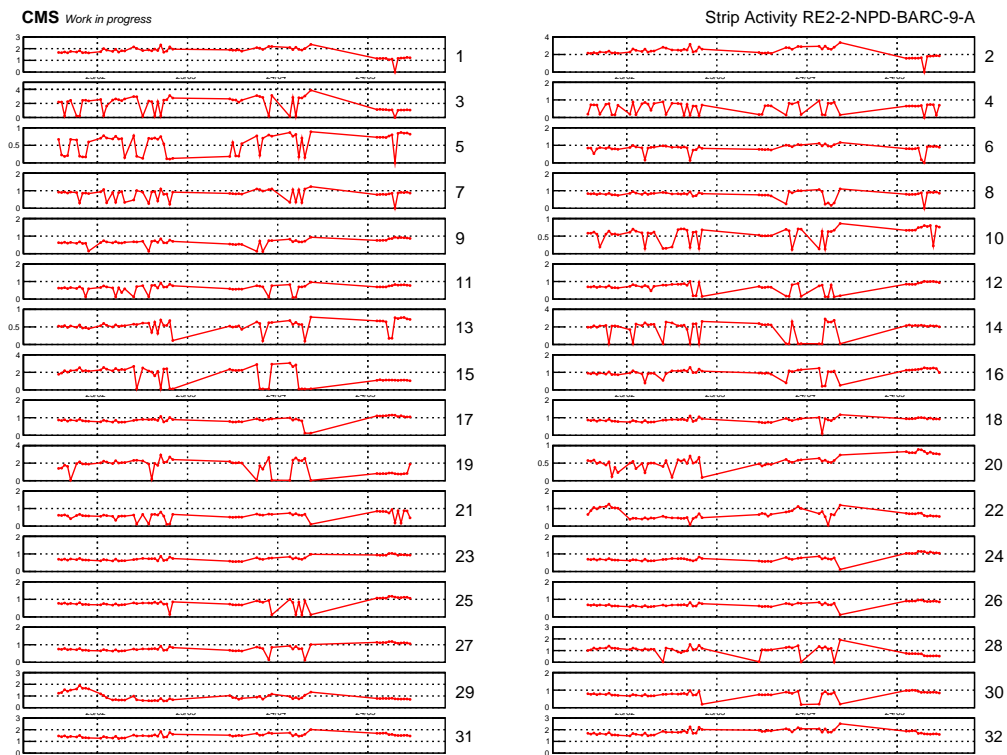


Figure 5.39: Example of strip activity of chamber RE2-2-NPD-BARC-09 monitored over time.

4172 5.3.5.3 Weekly noise monitoring scans

Once a week, the source is turned OFF to make a noise scan for the CMS RPC. This HV scan is composed of six runs for which 25,000 random triggers are accumulated. The first run is taken at

standby voltage and the second one at 8 kV. The next five runs are taken at voltages ranging from 9.4 to 9.8 kV in order to access for both type of chambers, RE2 and RE4, in the voltage region where the efficiency rises and reaches its plateau. The whole procedure is shown in Figure 5.40. On the occasion of this scan, the ongoing longevity scan is stopped. A new one will be started once the weekly scans are over.

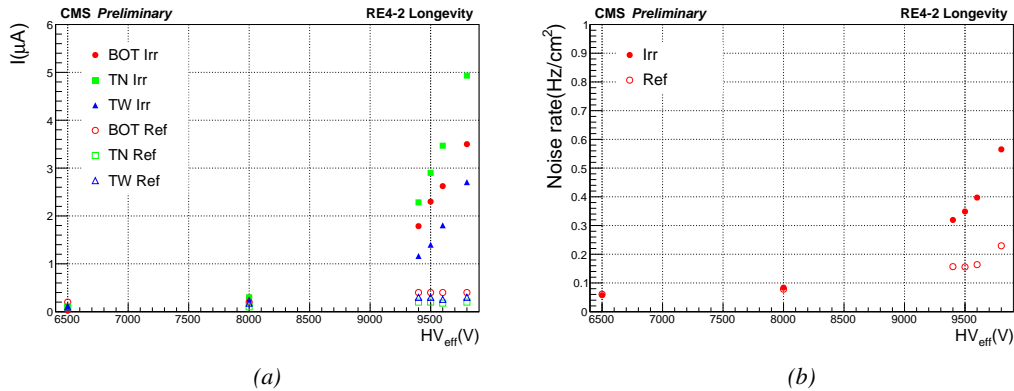


Figure 5.40: Example of rates (a) and currents (b) of irradiated chamber RE4-2-CERN-166 and reference chamber RE4-2-CERN-165 measured during a weekly noise scan.

5.3.5.4 Weekly source scans

Directly following the weekly noise scans, HV rate scans are organised at different source settings (usually ABS 6.8, 4.6 and 3.3). The procedure of these HV scans consists of nine runs for which 25,000 random triggers are accumulated. The first run is taken at standby voltage while the next eight runs are taken at voltages ranging from 9.4 to 10.1 kV. They aim at measuring the gamma rate to which the chambers are subjected and the related currents. The whole procedure is shown in Figure 5.41.

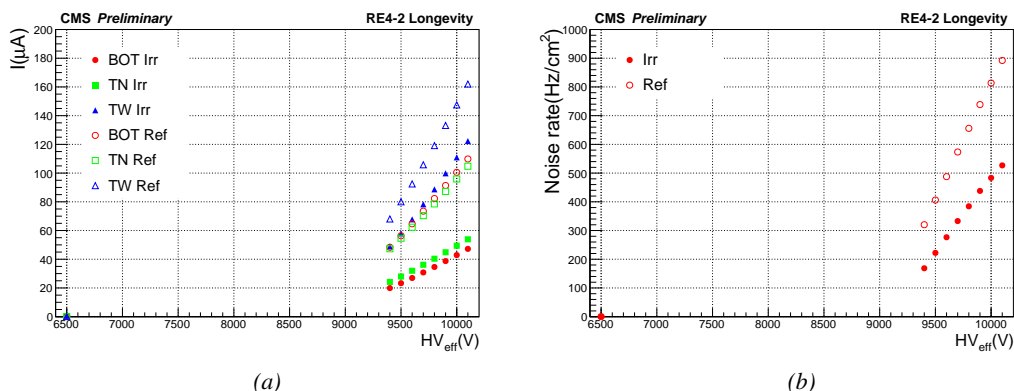


Figure 5.41: Example of rates (a) and currents (b) of irradiated chamber RE4-2-CERN-166 and reference chamber RE4-2-CERN-165 measured during a weekly source scan. The data were measured with ABS 123 (6.9).

5.3.5.5 Weekly current scans

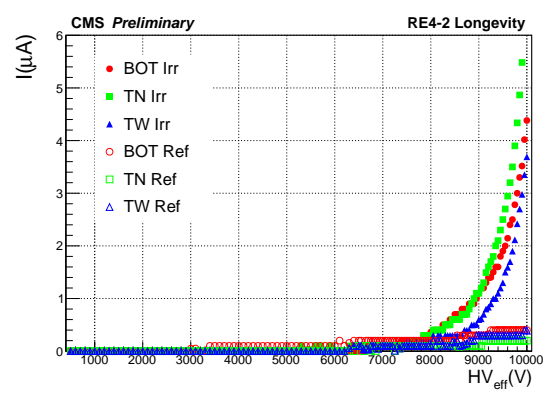


Figure 5.42: Example of currents of irradiated chamber RE4-2-CERN-166 and reference chamber RE4-2-CERN-165 measured during a weekly current scan.

procedure includes measurements at 131 high voltage points in between 500 V and 10 kV, in steps of 100 V until the standby voltage of 6.5 kV is reached and then in steps of 50 V. At low voltage, the current rise is slow and is only driven by the resistance of the detector electrode and thus increases linearly. It is referred to as the *ohmic current* as opposed to the *physics current* corresponding to the voltage region where charge multiplication starts to occur. A fit on the ohmic current range gives access to the resistance of the 'electrodes/gas' system. If any variation of the electrode resistance occurs, the global resistance will increase and so will the current. Technically, these scans will record a ROOT file per HV step that will have the same format as the CAEN ROOT file saved during other HV scans. The data is also analysed using the Offline Analysis tool to provide with DQM histograms as well as standardized I/V tables.

5.3.6 Extraction and monitoring of the resistivity

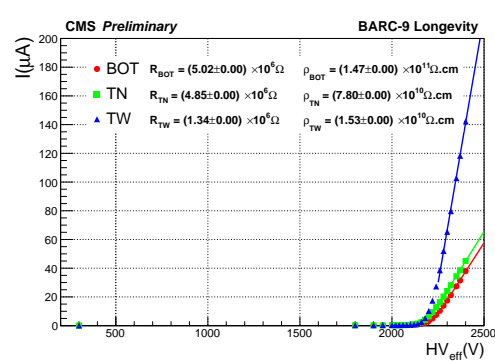


Figure 5.43: Example of currents of irradiated chamber RE2-2-NPD-BARC-09 measured during an argon scan. The resistance is extracted from the linear fit and the resistivity is computed using Equation 5.6.

the couple of electrodes R_{elec} is extracted as can be seen from Figure 5.43. The resistivity is then

The previously detailed daily rate scans, but also the weekly noise and source scans are interesting tools to look at an increase of noise rates and dark currents or at a loss of rate capability. They could point to an increase of surface resistivity of the electrodes through the absorption of hydrofluoric acid. Nevertheless, periodically measuring the currents on wider high voltage ranges allows to have access to the ohmic part of the current driven by the detectors related to the electrodes resistance. This is why precise current scans, consisting only in measuring the current driven through the four detectors, are performed each week. The scan pro-

A critical parameter to monitor is the resistivity of the electrodes. Its variation would impact the rate capability of the RPC. An increase of the resistivity with increased irradiation is expected. In the first place, the measurement of the resistivity of the electrodes is done using the so called *Argon scans*. Such tests are performed regularly before or after test beam periods through high voltage scans of the detectors operated with pure Argon. The electric field strength at which Argon breaks down being well known, the current beyond the breakdown voltage is monitored. Assuming a relation $I_{mon} = HV_{eff}/R_{elec}$ beyond the breakdown voltage, the resistivity of

the resistivity is then

deduced by using Formula 5.6 where S is the surface area of the gap and l the thickness of a single electrode.

$$(5.6) \quad \rho = R \times \frac{S}{2 \times l}$$

There exist other ways to access a quantity directly related to the resistivity. During the testbeam periods, the efficiency of the detectors is measured with both source OFF and source ON with high irradiation. The shift of voltage introduced by an irradiation is directly linked to the rate capability of the detector and hence to the resistivity of the electrodes. By comparing the efficiency curves observed with source ON and OFF during a single testbeam, it is possible to access the local mean resistance of the detector during a testbeam period. This value can be compared to the resistivity directly measured using the argon scans. It also provides a tool to compare different testbeam results by getting rid of the bias introduced by the fluctuation of the resistivity through time. The mean resistance is computed as in Formula 5.7.

$$(5.7) \quad R = \frac{\Delta HV}{\Delta I} = \frac{HV^{ON} - HV^{OFF}}{I^{ON} - I^{OFF}}$$

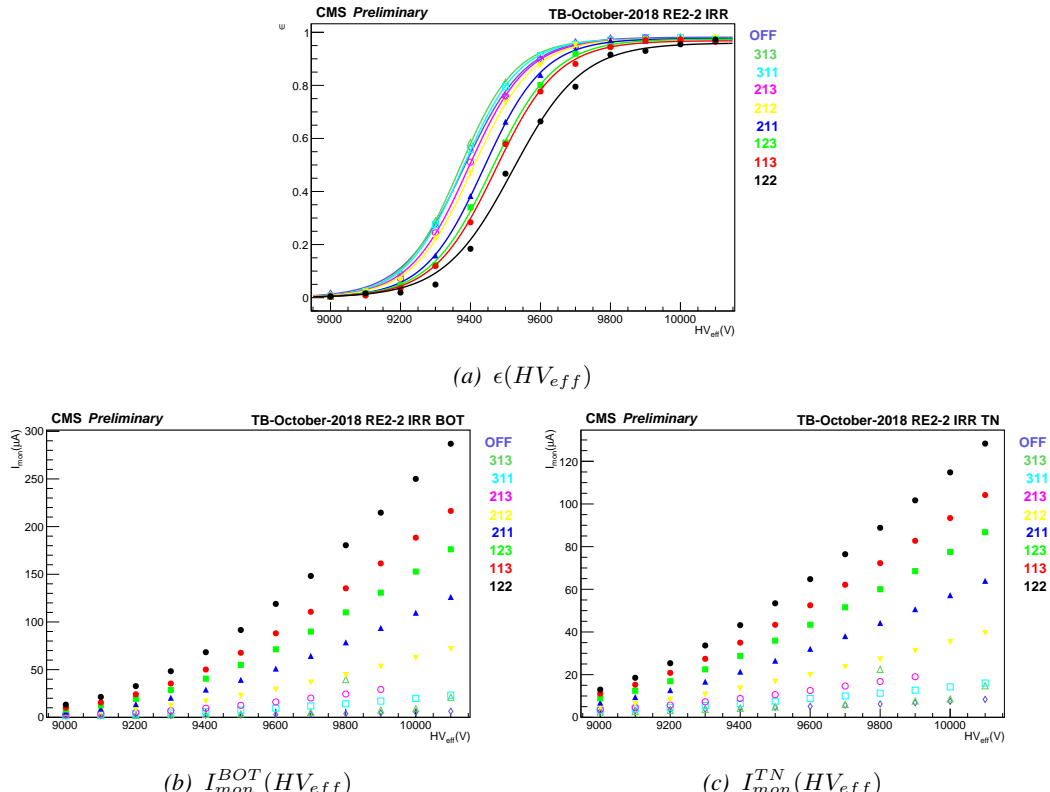


Figure 5.44: Efficiency (a) and monitored currents of the bottom (b) and top narrow (c) gaps as a function of the effective voltage of chamber RE2-2-NPD-BARC-09 during October 2018 testbeam period.

4242 It is important to note that the result provided by using this method will only concern the re-
 4243 sistance of the detector under the beam, including the little contribution of the resistance of the gas
 4244 volume itself. The translation to the resistivity of the electrodes is not straight forward even though
 4245 the result falls in the same order of magnitude. Also, the quality of the resistance extraction depends
 4246 on which level of irradiation is available in the data. During October 2018 testbeam period, HV
 4247 scans were done on partition C of the RPCs (bottom and top narrow gas gaps) with source OFF and
 4248 with eight diffent ABS values: ABS 313 (464), ABS 311 (100), ABS 213 (46.4), ABS 212 (21.5),
 4249 ABS 211 (10), ABS 123 (6.9), ABS 113 (4.6) and ABS 122 (3.2). T1 was placed close to the bunker
 4250 upstream wall at a distace of 5.6 m from the source. This position corresponds to a gamma current
 4251 of the order of $5 \times 10^5 \text{ cm}^{-2} \text{ s}^{-1}$ with source fully open.

4252 In a first step, the efficiency sigmoids as well as the bottom and top narrow gaps' monitored
 4253 current as a function of the effective voltage were retrieved as can be seen from Figure 5.44. The
 4254 goal is to compute the value of the effective voltage at the knee HV_{knee} of the sigmoids. The knee
 4255 where $\epsilon = 0.95 \times \epsilon_{max}$ would be the best location to extract the value of the resistivity. At this point,
 4256 the performance of the detectors is stable and a little variation of voltage does not have a large effect
 4257 on the efficiency. The effective voltage at the knee is given by Formula 5.8.

$$(5.8) \quad HV_{knee} = HV_{50} + \frac{\ln(19)}{\lambda}$$

4258 The monitored current at the knee I_{knee}^G for each gap G is then computed by extrapolating from
 4259 the monitored currents value located around HV_{knee} as in Formula 5.9 where I_{\downarrow}^G and HV_{\downarrow}^G are the
 4260 monitored current and the effective voltage at the voltage point bellow the knee and I_{\uparrow}^G and HV_{\uparrow}^G
 4261 are the monitored current and the effective voltage above the knee.

$$(5.9) \quad I_{knee}^G = I_{\downarrow}^G + (I_{\uparrow}^G + I_{\downarrow}^G) \times \frac{HV_{knee} - HV_{\downarrow}^G}{HV_{\uparrow}^G - HV_{\downarrow}^G}$$

4262 Once the values of the monitored currents are known at the knee, the mean current flowing
 4263 through the gaps at the level of the studied partition P can be computed. First of all, the currents at
 4264 knee of the gaps in the beam line is normalised to the area of the gap active area seen by the local
 4265 read-out partition $S^{G,P}$. Then the mean current at knee \bar{I}_{knee}^P is computed by ponderating the local
 4266 currents $I_{knee}^{G,P}$ of each gap by their respective active area in the partition.

$$(5.10) \quad \begin{aligned} I_{knee}^{G,P} &= \frac{I_{knee}^G \times S^{G,P}}{S^G} \\ \bar{I}_{knee}^P &= \frac{I_{knee}^{1,P} \times S^{1,P} + I_{knee}^{2,P} \times S^{2,P}}{S^{1,P} + S^{2,P}} \end{aligned}$$

4267 The variation of effective voltage and mean monitored current at the knee in between the Source
 4268 OFF and ON scans can then be obtained. The local resistivity of the detector can finally be calculated
 4269 combining Formula 5.6 and Formula 5.7. This process is performed for every scan of each approved
 4270 test beam period as can be seen in Figure 5.45. Finally, the most probable resistivity during the test
 4271 beam period is obtained thanks to a constant fit. The value of the mean partition resistivity displayed
 4272 in Figure 5.45 is of the same order than what would be expected for CMS RPCs.

Later, the value extracted from this method will be used to compare the efficiency sigmoids of the different testbeam periods. During the operation of the detector without irradiation, the voltage drop across the detector almost only consists in a voltage drop across the gas volume. As the electrodes behave approximately as charged capacitors, there is only a negligible voltage drop across their volume. The charge of the electrodes is only affected locally by the charge carriers freed by avalanches in the gas volume. Nevertheless, under irradiation, the conversion of photons is uniform throughout the electrodes' volume and charge recombination happens everywhere at the same time making it impossible for the electrodes to stay charged. Hence, a significant part of the voltage drop appears across the electrodes, explaining the usual voltage shift observed in the performance of irradiated RPCs. The data comparison will then be done using the gas voltage drop HV_{gas} obtained by correcting the effective voltage HV_{eff} thanks to Formula 5.11 in which R is the resistance computed at the knee using Formula 5.7 in the RPC partition of interest and \bar{I} is the mean current in this partition at each voltage step.

$$(5.11) \quad HV_{gas} = HV_{eff} - R \times \bar{I}$$

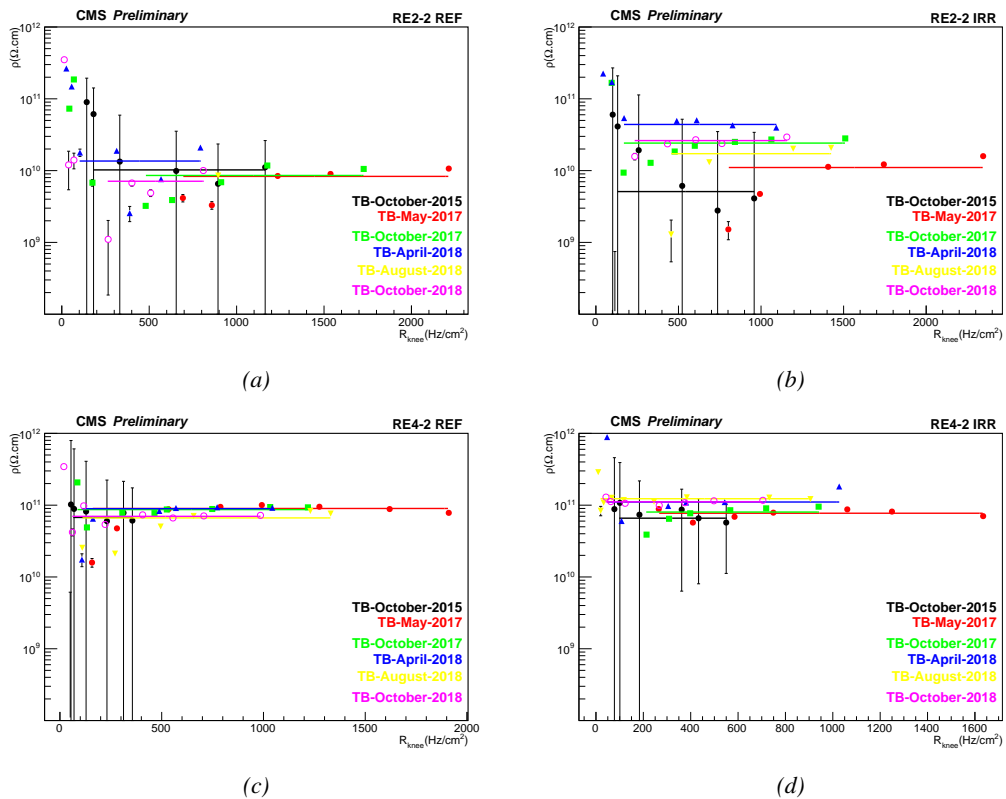
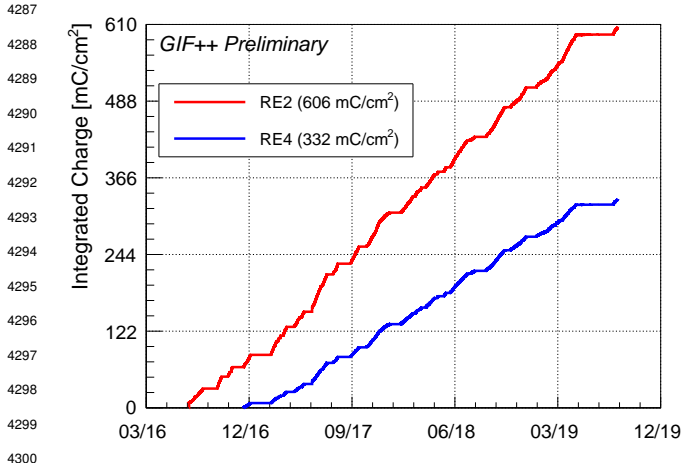


Figure 5.45: Resistivity extraction for all approved test beam periods for the reference RE2/2 (a) and RE4/2 (c) chambers and the irradiated RE2/2 (b) and RE4/2 (d) chambers.

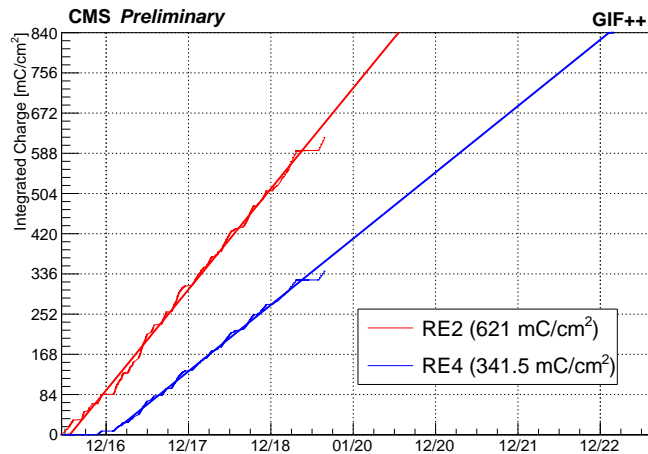
4286 **5.3.7 Results and discussions**



4301 *Figure 5.46: Total integrated charge in the irradiated RPCs,*
 4302 *RE2-2-NPD-BARC-9 and RE4-2-CERN-165, in July 2019.*
 4303 *The irradiation of the RE2 chamber started early July 2016 while*
 4304 *the RE4 chamber couldn't be irradiated before end of November*
 4305 *2016.*

4306 charge accumulation of the RE2 detector is faster than which of the RE4 and is expected to end
 4307 within a year. In the case of the RE4 RPC, the irradiation would go on for more than two years at
 4308 the current charge accumulation rate. This time would be reduced after the end of the longevity study
 4309 of the RE2 by placing the trolley hosting the detectors closer to the source.

Since 2015, CMS RPCs have been irradiated at the GIF++ with the goal to reach a total integrated charge per irradiated detector of $0.84 \text{ C}/\text{cm}^2$ while certifying the detectors to a single hit rate capability of $600 \text{ Hz}/\text{cm}^2$. At the time of writing, the RE2 and RE4 chambers were exposed to 74 and 40% of their total irradiation program respectively, as shown in Figure 5.46. According to Figure 5.47, a few years of irradiation are expected before reaching the end of the longevity study for both types of detectors and before reaching a final answer on whether the present CMS RPC system will be able to live through HL-LHC or not.



4301 *Figure 5.47: Linear projection of the time necessary to finish the longevity program on the RE2 and RE4*
 4302 *detectors at the GIF++.*

4310 5.3.7.1 Long term monitoring of the RPC parameters

4311 Throughout the longevity program, great care was put into monitoring the detector characteristics.
 4312 While presenting the results, current densities expressed in $\mu\text{A}/\text{cm}^2$ will be showed in the place of
 4313 currents. In the first part of the discussion the current densities will be referred to as "dark current".
 4314 Also, the data of the reference detectors will be displayed with increasing integrated charge. This
 4315 integrated charge will always refer to the integrated charge of the irradiated detectors.

4316 Using the data collected during the weekly noise scans performed on all four RPCs, the dark
 4317 currents are monitored. Two voltage of interest are being compared through time. The first value
 4318 of interest was chosen at a *STANDBY* voltage of 6500 V where no multiplication process happens.
 4319 This is done to follow the variations of the ohmic component of the current. The monitored dark
 4320 current in *STANDBY* are shown in Figure 5.48. At the time of writing, the ohmic currents for all
 4321 detectors are stable. Both RE4 detectors appear to follow the same trend while the ohmic current
 4322 of the irradiated RE2 detector has increased a little. Nevertheless, this increase is only of 10 to
 4323 20 pA/cm^2 and a similar behaviour can be observed for both RE4 detectors. There is no reason to
 4324 associate the increase in ohmic current with the irradiation.

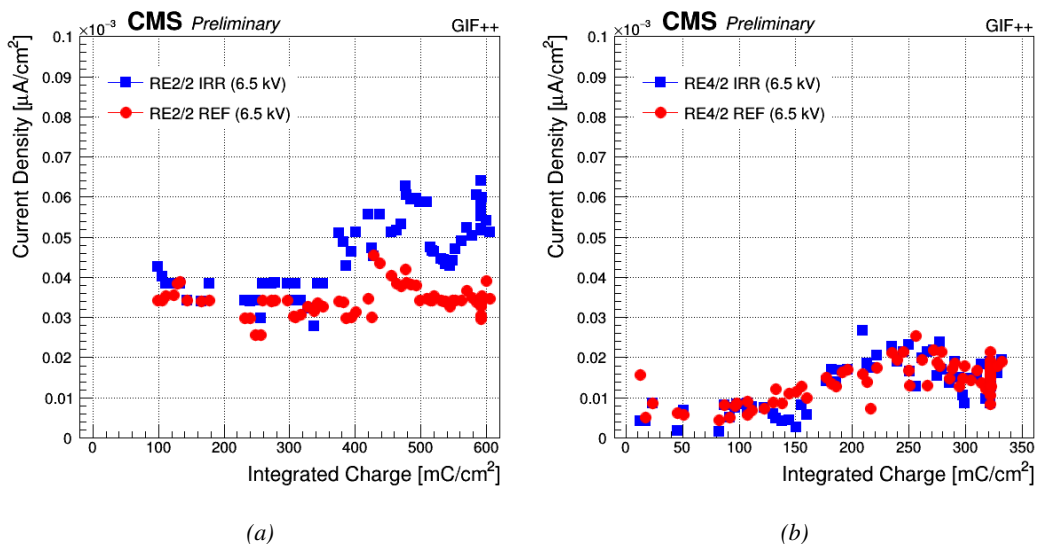


Figure 5.48: Monitoring of the ohmic component of the dark current with increasing integrated charge at a voltage of 6500 V of the RE2-2 (a) and RE4-2 (b) detectors installed at the GIF++.

4325 The second value of interest is located in the gain region near the working point at a voltage
 4326 of 9600 V for the RE2 detectors and of 9500 V for the RE4 ones. Monitoring the multiplication
 4327 region allows to spot the appearance of hot spots across the detectors' areas. A local damage to the
 4328 electrode could result in an increase of local discharges and an overall increase of the current drawn
 4329 by the detector which would show in the monitored values. Near the working voltage, in addition to
 4330 the current densities, the noise rate per unit are monitored as can be seen in Figure 5.49. In the case
 4331 of the RE2 detectors, the dark currents and noise rate stay stable since the beginning of the irradiation
 4332 program. The variability of the dark current of the irradiated chamber is higher than the one of the
 4333 reference chamber but seem to always come back between 0.1 and 0.15 nA/cm^2 . Concerning the
 4334 RE4 detectors, both chambers are very stable up to an irradiation of 150 mC/cm^2 .

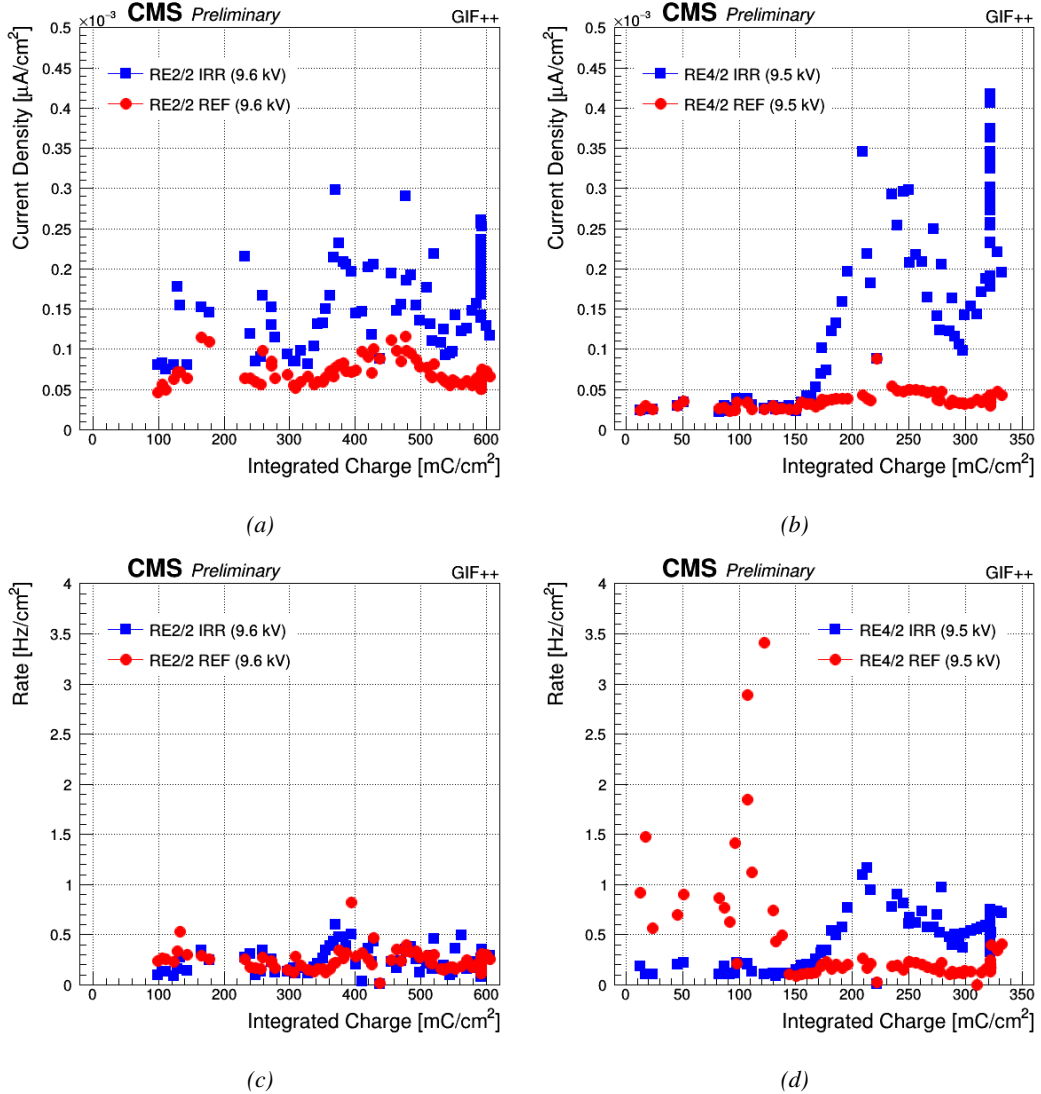


Figure 5.49: Monitoring of the physics component of the dark current and of the noise rate per unit area with increasing integrated charge at a voltage of 9600 V for the RE2-2 detectors (a) and (c) and at a voltage of 9500 V for the RE4-2 detectors (b) and (d) installed at the GIF++.

Even though the noise rate of the reference chamber seem to fluctuate a lot between 0.5 and 3.5 Hz/cm^2 before this value, the monitoring of the noise rate per unit area following this early range as well as the very stable dark current would suggest that the chamber was in fact suffering from a bad grounding. Indeed, beyond 150 mC/cm^2 , the noise rate suddenly stabilizes between 0.1 and 0.2 Hz/cm^2 while the dark current increases very slightly to 50 pA/cm^2 . On the contrary, the irradiated chamber which was very stable under 150 mC/cm^2 , sees its dark current and its noise rate increase and fluctuate with a similar shape. The noise rate is still within the requirements of CMS. Indeed, an upper threshold of 1 Hz/cm^2 was considered to be good enough to prevent fake events due to noise. Regarding the dark current, so far the highest peak, reached a little higher

than 0.4 nA/cm^2 and have since dropped to 0.2 nA/cm^2 . During *source scans* at gamma rates per unit area usually above 400 Hz/cm^2 , the current densities are of the order of 10 nA/cm^2 , almost two orders of magnitude larger than the dark current. Nevertheless, both the noise rate and dark current have almost gained an order of magnitude at their highest monitored values and will need to be carefully followed at higher values of integrated charge.

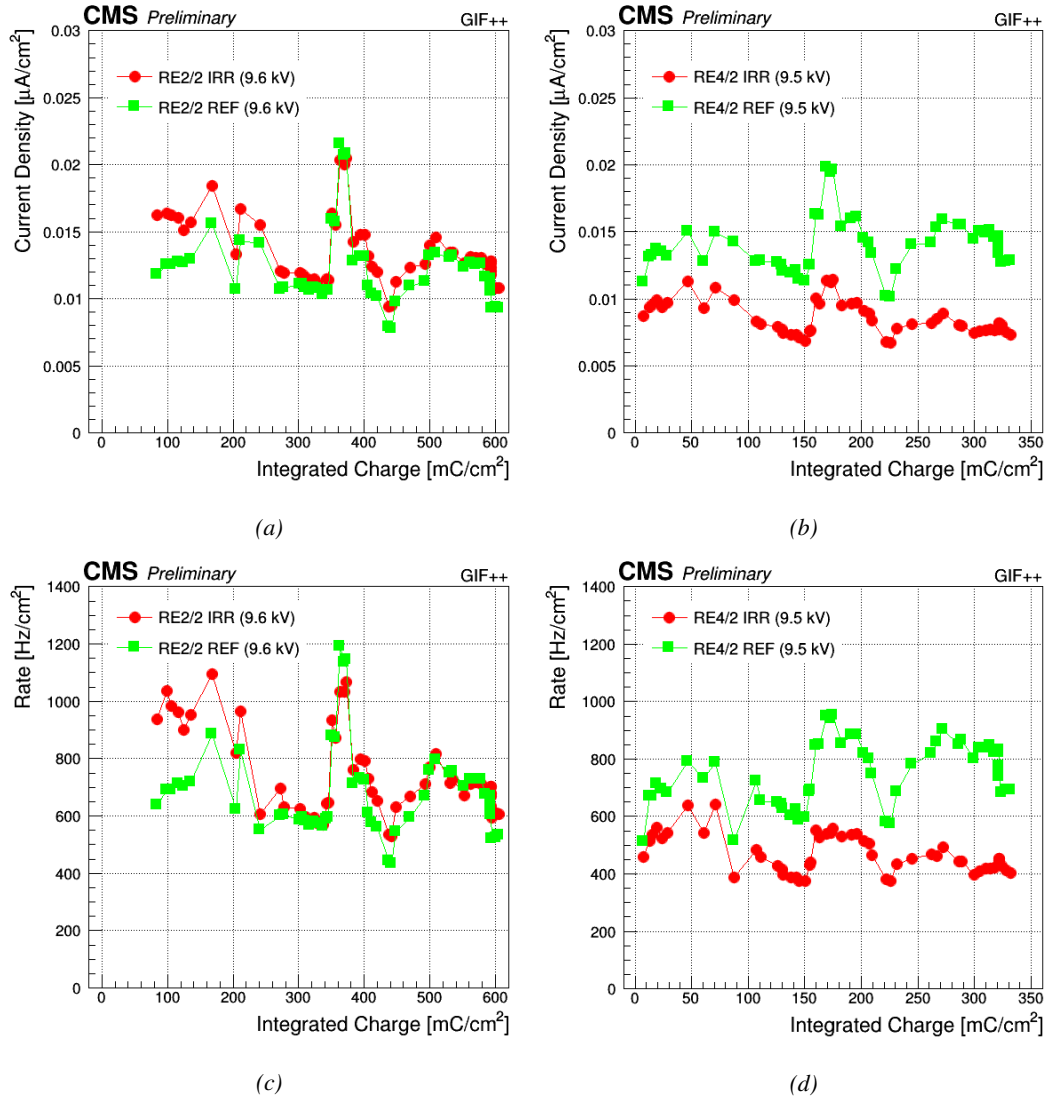


Figure 5.50: Monitoring of the current density and of the gamma rate per unit area under irradiation with increasing integrated charge at a voltage of 9600 V for the RE2-2 detectors (a) and (c) and at a voltage of 9500 V for the RE4-2 detectors (b) and (d) installed at the GIF++. The source irradiation is attenuated by a factor 6.9.

The same exercise is done using the data collected during the weekly source scans. The monitoring of the current densities and of the gamma rate per unit area is showed in Figure 5.50. The reported measurements are always performed with the same source conditions corresponding to an

4352 irradiation attenuated by a factor 6.9. The increase in dark current of the irradiated RE4 chamber
 4353 don't have any visible effect when the source irradiates the detectors. No signs of ageing due to
 4354 irradiation is yet to be seen for both the RE2 and RE4 detectors. The current densities and gamma
 4355 rates of all four detectors evolve following the same phases of increase and decrease, as confirmed
 4356 by Figure 5.51.

4357 The use of Principal Component Analysis (PCA) [279] reveals that the study of the correlations
 4358 between the current densities and the gamma rates can be reduced to a single dimension. To perform
 4359 the PCA, the algorithm used normalises each variable to get a mean value of 0 and a variance of
 4360 1 resulting in the study of the variance. The associated *Scree* plot [280] showed in Figure 5.51b
 4361 indicates for each of the components of the PCA, the eigenvalues of the covariance matrix. In this
 4362 case, the eigenvalues have been normalised to express the percentage of variance explained by each
 4363 component. More than 93% of the data variation can be explained using a simple linear composition
 4364 of the current density and of the gamma rate. It is expected as the current density and gamma rate
 4365 are two side of the same physical process. Any deviation would mean that other processes than the
 4366 conversion of photons in the electrode material take place.

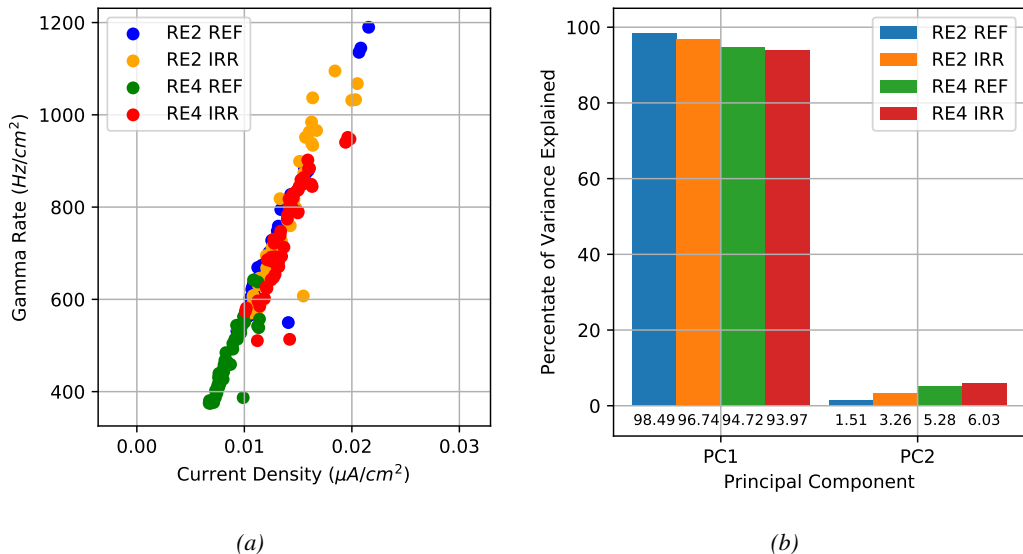


Figure 5.51: (a) Gamma rates as a function of the corresponding current densities. (b) Scree plot obtained at the output of PCAs performed on each set of current densities and corresponding gamma rates.

4367 The fluctuations observed on Figure 5.50 may arise due to different factors such as the environmental
 4368 conditions (gas temperature, gas relative humidity, environmental pressure) or the presence
 4369 of other experiments between the source. The distance from the source and the trolley, and the
 4370 gamma current at which the detectors are irradiated during the ageing procedure are kept as consistent
 4371 as possible and should not contribute to the fluctuations in current density and gamma rate. In
 4372 order to have a better understanding, the monitoring of the environmental parameters, i.e. the gas
 4373 relative humidity and temperature both at the supply and at the exhaust of the trolley together with the
 4374 humidity and temperature inside of the bunker and the environmental pressure, is showed in Figures
 4375 5.52, 5.53 and 5.54. In these Figures, the data are displayed with increasing integrated charge
 4376 in the case of the RE2 and of the RE4 detectors for comparison purposes. Each value of integrated

⁴³⁷⁷ charge corresponds to a unique date.

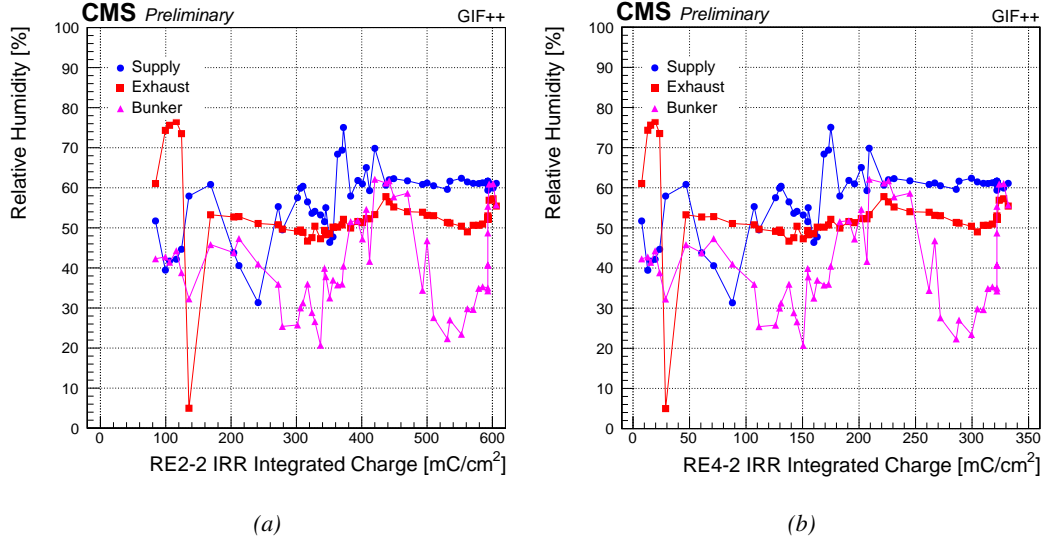


Figure 5.52: Monitoring of the gas relative humidity at the level of the supply and of the exhaust of T1 and ambient relative humidity at the GIF++ during the source scans.

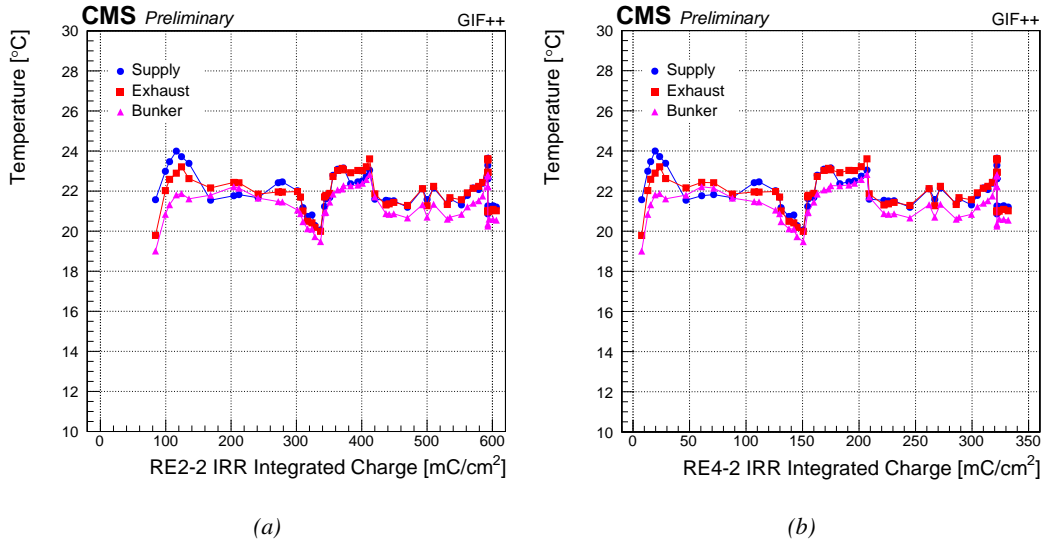


Figure 5.53: Monitoring of the gas temperature at the level of the supply and of the exhaust of T1 and ambient temperature at the GIF++ during the source scans.

⁴³⁷⁸ Comparing the trends visible in Figure 5.50 to the monitoring of the different environmental
⁴³⁷⁹ parameters, it would seem that the temperature variations may be able to explain most of the fluctuations.
⁴³⁸⁰ This assumption is confirmed by a PCA performed on data sets composed for each detector
⁴³⁸¹ of the monitored environmental parameters and of its current density and gamma rate data. The

4382 corresponding Scree plot is showed in Figure 5.55. The dimension reduction for this data set is less
 4383 trivial as expected.

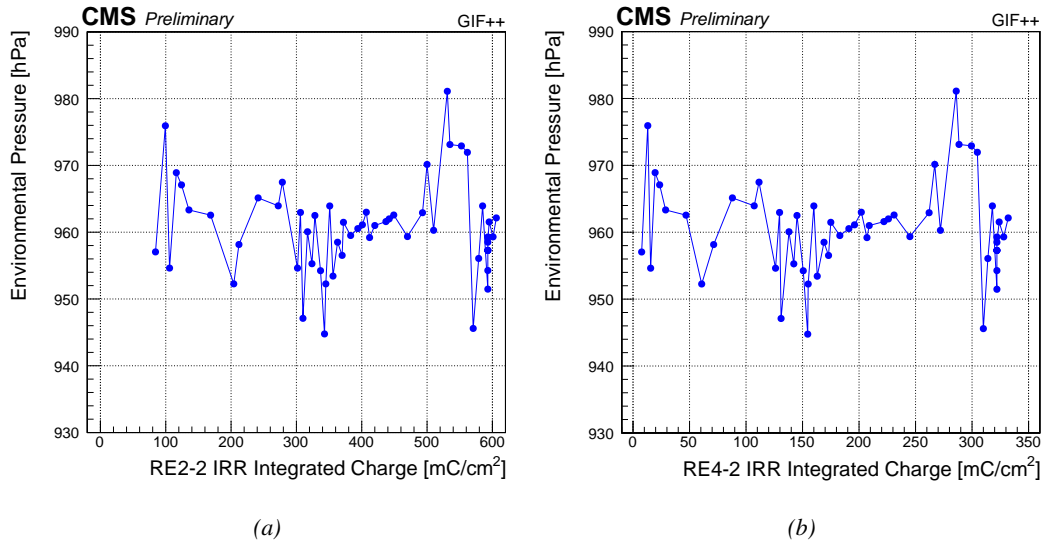
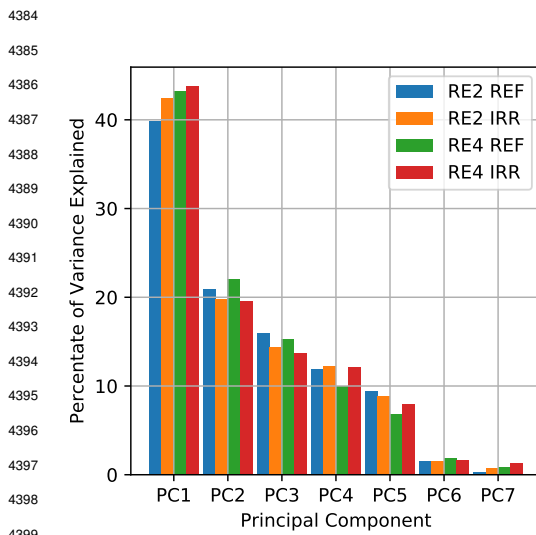


Figure 5.54: Monitoring of the environmental pressure at the GIF++ during the source scans.



4400 Figure 5.55: Scree plot corresponding to the PCAs per-
 4401 formed on each RPC data set to study the influence of the
 4402 environmental parameters in the fluctuation of the cur-
 4403 rent densities and gamma rates.

4404 density and gamma rate vectors in the principal component eigenvector space with the environmental
 4405 parameters vectors are summarized. The linearity between current density and gamma rate is again
 4406 visible. Moreover, the temperature seems to always be a positive source of variation for the current
 4407 density and the gamma rate.

4384 Nevertheless, most of the variation in cur-
 4385 rent densities and gamma rates is held by the
 4386 first principal component of the PCA basis
 4387 for all four detectors, as can be understood
 4388 from the Score plots presented in Figure 5.56.
 4389 The Score plots show for each principal com-
 4390 ponent the decomposition of its correponding
 4391 eigenvector in terms of the variables of the
 4392 original data set normalised to the eigenvalue
 4393 associated to the eigenvector. The eigenvectors
 4394 represent the directions of maximum vari-
 4395 ance. Hence, the *strength* of each original
 4396 variable leads to its variability along this di-
 4397 rection.

4398 Based on the information of Figure 5.56, the
 4399 first principal component can be interpreted
 4400 as the variations directly linked to the fluctua-
 4401 tions in current density and gamma rate. This
 4402 statement is supported by Table 5.6 in which
 4403 the values of the scalar products of the current
 4404 density and gamma rate vectors in the principal
 4405 component eigenvector space with the environ-
 4406 mental parameters vectors are summarized. The
 4407 linearity between current density and gamma rate is again
 4408 visible. Moreover, the temperature seems to always be a positive source of variation for the current
 4409 density and the gamma rate.

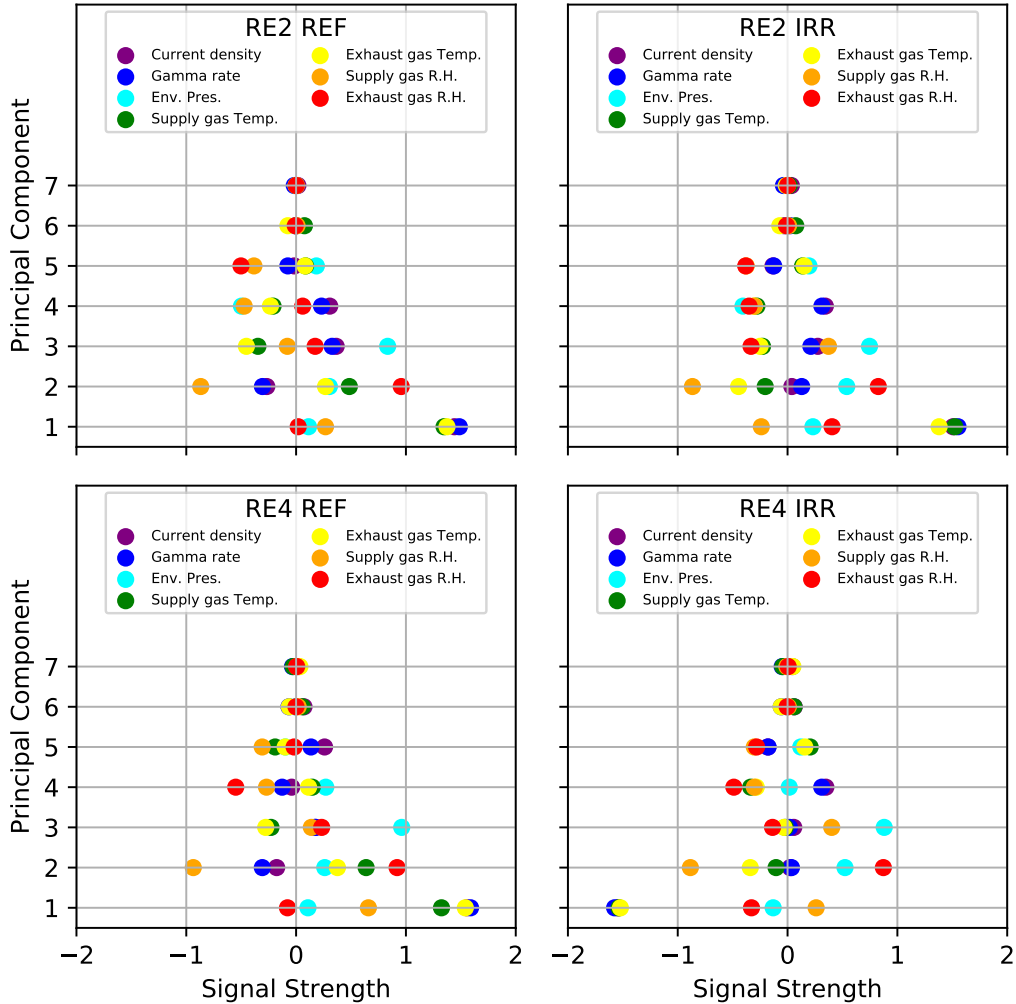


Figure 5.56: Score plots corresponding to the PCAs performed on each RPC data set to study the variations in current density and gamma rate.

Variables	Current density				Gamma rate			
	RE2 REF	RE2 IRR	RE4 REF	RE4 IRR	RE2 REF	RE2 IRR	RE4 REF	RE4 IRR
Env. Pres.	0.21	0.38	0.21	0.19	0.20	0.40	0.16	0.16
Bunker Temp.	1.83	2.01	2.69	2.66	1.93	2.03	2.76	2.75
Bunker air R.H.	-0.83	-0.31	-0.38	0.26	-0.82	-0.23	-0.26	0.35
Supply gas Temp.	1.91	2.42	2.31	2.64	2.00	2.48	2.30	2.73
Exhaust gas Temp.	2.03	2.26	2.81	2.76	2.13	2.28	2.86	2.85
Supply gas R.H.	0.45	-0.33	1.18	-0.39	0.56	-0.42	1.40	-0.40
Exhaust gas R.H.	-0.23	0.43	-0.29	0.40	-0.25	0.57	-0.34	0.46

Table 5.6: Summary of the scalar product between the current density and gamma rate vectors, and the environmental parameters vectors in the principal component eigen vector space.

The contribution of the atmospheric pressure is always significantly smaller but consistent and could be a source of positive feedback. The relative humidity of the gas and of the air in the bunker

on the other hand doesn't provide a consistent feedback but it can be noted that the role of the supply and exhaust humidity seem to have an opposite effect in the case of the reference detectors than in the case of the irradiated detectors.

It is safe to conclude that the voltage correction performed at the GIF++ is not able to account for the high variability of the temperature in the bunker and, hence, of the gas mixture the detectors are operated with. The pressure on the other hand does not play a great role in affecting the RPC operation as the voltage correction was improved to efficiently take into account this parameter [234]. The environmental conditions in the CMS cavern are much more stable in terms of temperature providing an explanation for the less refined temperature correction on the applied voltage as discussed in Section 3.4 of this document.

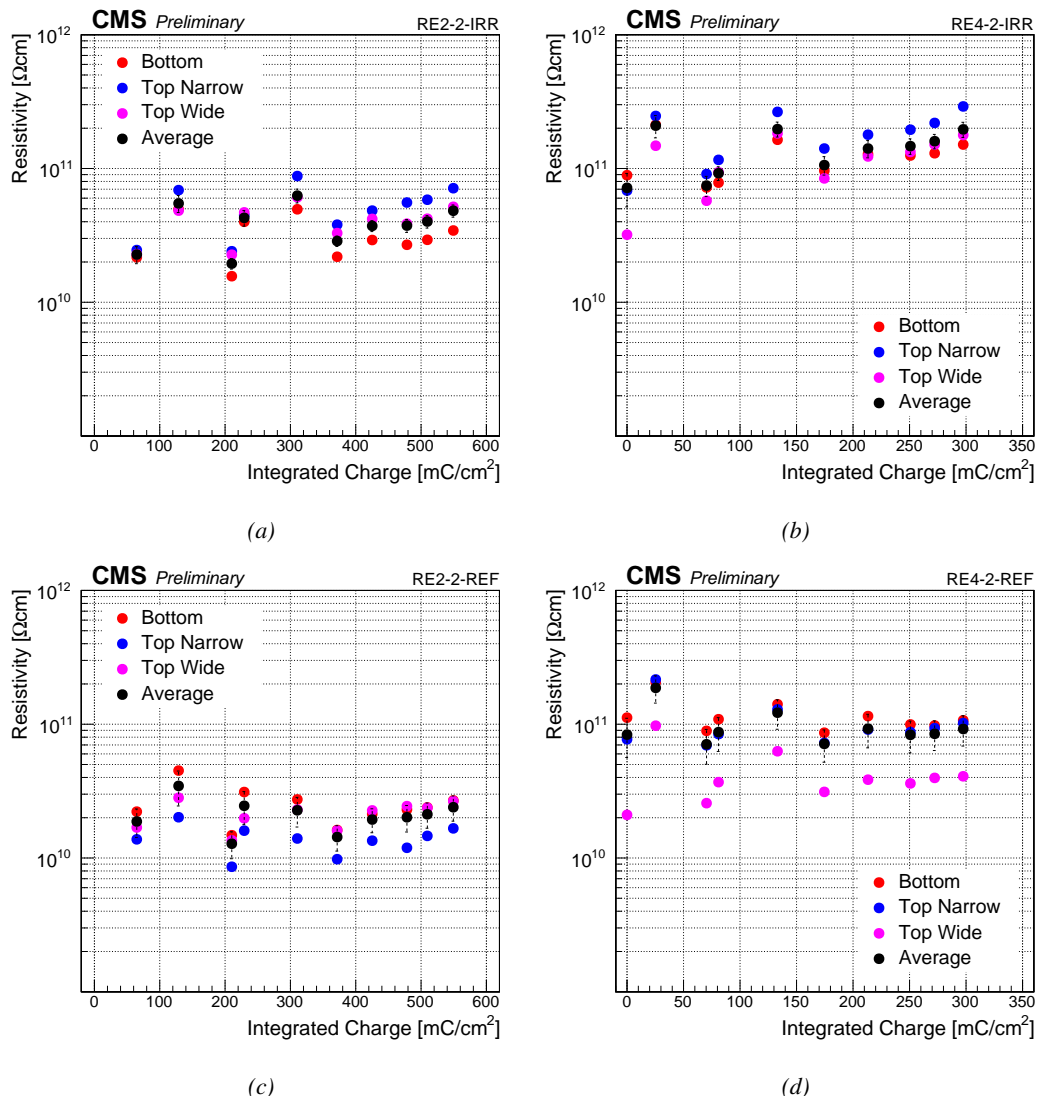


Figure 5.57: Monitoring through argon scans of the resistivity with increasing integrated charge for the RE2-2 detectors (a) and (c) and the RE4-2 detectors (b) and (d) installed at the GIFF++.

4420 Aside of the fluctuations due to the insufficient temperature correction, it seems that both the
 4421 current densities and gamma rate of the irradiated detectors tend to decrease with time. The reference
 4422 detectors features a more stable operation through time. Comparing the evolution of the current
 4423 densities and of the gamma rates to the monitored resistivity showed in Figure 5.57 may explain the
 4424 decrease observed for the irradiated chambers and the more stable behaviour of the reference ones.
 4425 An increase of resistivity is observed for both the irradiated detectors whose average resistivity went
 4426 from $2.27 \times 10^{10} \Omega \text{ cm}$ for the RE2 and from $7.17 \times 10^{10} \Omega \text{ cm}$ to $1.96 \times 10^{11} \Omega \text{ cm}$ for the
 4427 RE4. The average resistivity of the reference RE2 chamber from $1.88 \times 10^{10} \Omega \text{ cm}$ but is still
 4428 compatible with a stable resistivity due to the wide error bars. On the contrary, the average resistivity
 4429 of the reference RE4 is more or less at the same level at the time of writing ($9.22 \times 10^{10} \Omega \text{ cm}$) than
 4430 it was at the start of the longevity program ($8.36 \times 10^{10} \Omega \text{ cm}$). The differences in increase rate of
 4431 the irradiated chambers with respect to the reference ones can be seen in Figure 5.58. It is clear that
 4432 both the current density and the gamma rate of the irradiated detectors decreases relatively to the
 4433 reference ones. This is consistent with the relative increase in average resistivity of the irradiated
 4434 chambers with respect to the reference ones.

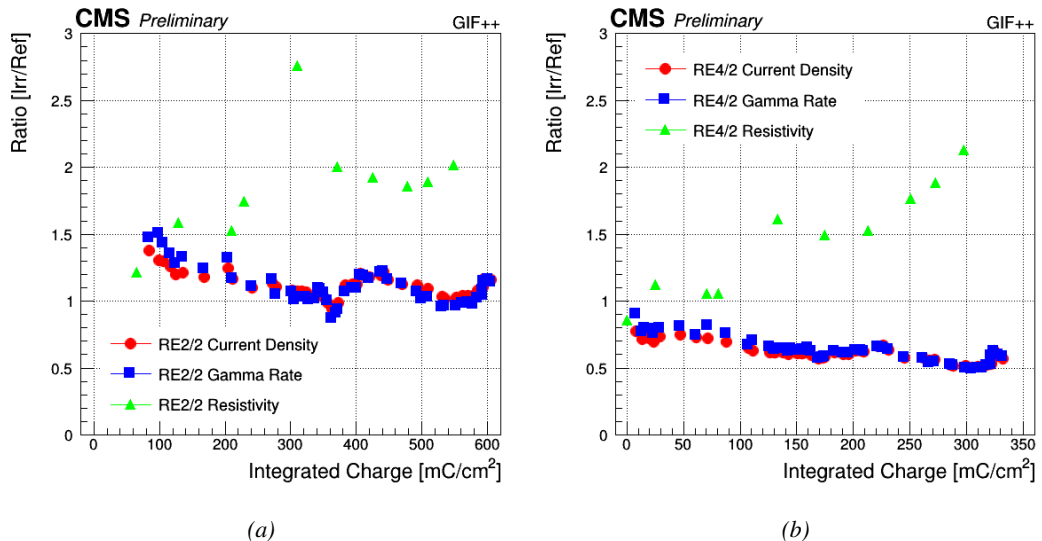
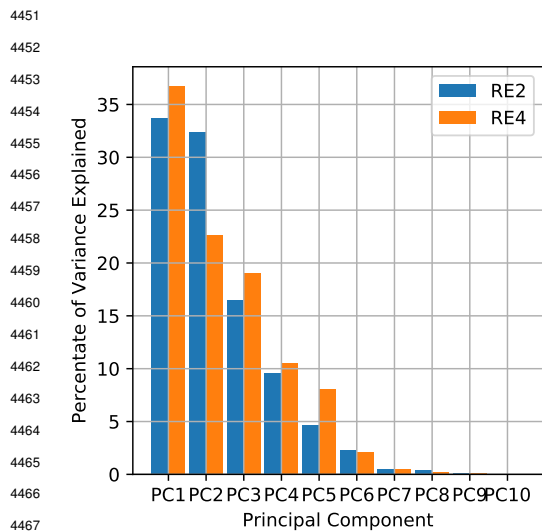


Figure 5.58: "Irradiated over Reference" parameter ratios (current densities, gamma rates and resistivities) as a function of the integrated charge for the RE2 5.58a and the RE4 5.58b detectors installed at the GIF++.

4435 In addition to the decrease of the irradiated detectors current densities and gamma rates with
 4436 respect to the reference RPCs, the fluctuation that can be observed in the ratios could be related to
 4437 the fluctuations of gas humidity observed in Figure 5.52. The effect is seems clearer in the case of
 4438 the RE2 detectors than in the case of the RE4. A PCA is once again performed on updated RPC
 4439 data sets. The single current densities and gamma rates are this time replaced by the "Irradiated over
 4440 Reference" current density and gamma rate ratios. The Scree plot in Figure 5.59 shows a slightly
 4441 different distribution of the variability along the principal components in both cases.
 4442 The Score plots in Figure 5.60 confirms the difference noticed in the Scree plot. Indeed, for the RE2,
 4443 the first principal component mainly shows variability of the temperatures and of the supply relative
 4444 humidity but there is no correlation with the current density or the gamma rate ratios. In fact, their
 4445 variability seems mainly contained in the second principal component together with the variability
 4446 of the bunker and of the exhaust relative humidity. The interpretation of the Score plot in the case of
 4447 the RE4 is much more complex and could be due to the much smaller amplitude of the fluctuation

of the ratios with respect to the RE2. When the environment relative humidity was playing a great role for the RE2, it seems that most parameters have a non negligible effect on the RE4.

4450



4468 *Figure 5.59: Scree plot corresponding to the PCAs per-
4469 formed on each RPC data set to study the influence of the
4470 environmental parameters in the fluctuation of the cur-
4471 rent densities and gamma rates.*

4472

end gas connectors are different. The plastic material of the gas connectors at the level of the gas gaps could for example have a different porosity in between both detector types. Or the tightness of the gas connections is simply of better quality for the RE4 than for the RE2. As a matter of fact, it is known at CMS that the RE4 detectors have a significantly lower gas leak rate as a whole than the rest of the CMS RPC sub-system. Based on this information, the RE2 detectors placed at the GIF++ could have a higher chance of having a gas leak. In the case there are gas leaks, the gas leak of the RE2 detectors could also be bigger than the gas leak of the RE4. Such gas leaks would result in a possible humidity exchange between the air inside of the bunker and the gas mixture inside of the detector as well as a contamination of the mixture by with air.

4482

In conclusion, once the fluctuations of the current densities and gamma rate have been understood as a consequence of the imperfect temperature correction, it remains that the resistivity of the irradiated detectors is decreasing with respect to the reference ones. A better control of the relative humidity in the bunker or an investigation for gas leaks on the detectors could help to mitigate the observed decrease of resistivity of the irradiated electrodes.

The information provided by Table 5.7 which summarizes the scalar products between the current density and the gamma rate ratios vectors, and the environmental parameters vectors, reaches a similar conclusion. The effect of the bunker and of the exhaust relative humidity is clear for the RE2 where the fluctuation is the strongest. But no similar conclusion can be made for the RE4 in which all parameters provide a signal. The PCA has failed to reveal an effect of the humidity for the RE4 even though the fluctuation is likely to have the same origin than the one observed for the RE2 as the dates coincide.

The difference between the RE2 and the RE4 detectors is their manufacturing dates. As was already said, the RE2 detectors were manufactured prior to the start of the LHC while the RE4 were manufactured and installed in CMS during LS1. It is not impossible that the providers of the different parts such as the gas connectors of the gas gaps and the on front-

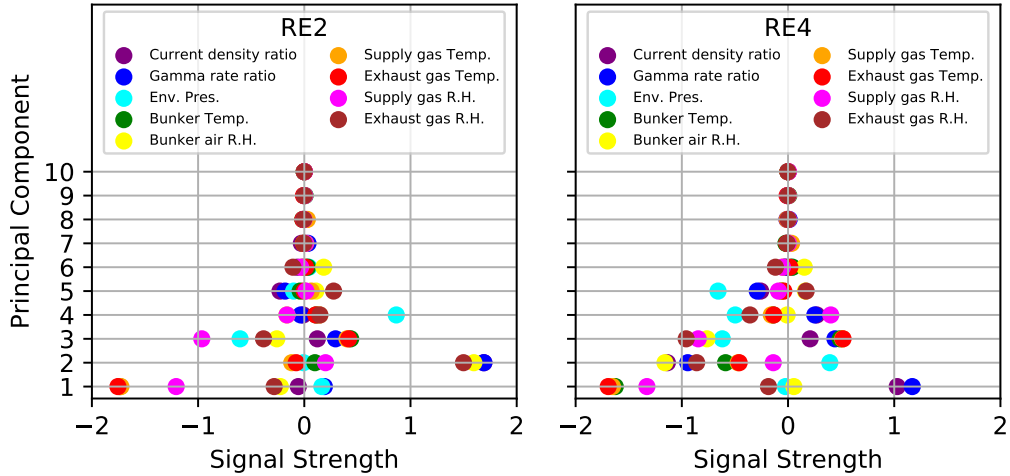


Figure 5.60: Score plots corresponding to the PCAs performed on each RPC data set to study the variations in current density and gamma rate ratios of the irradiated chambers with respect to the reference ones.

Variables	Current density ratio		Gamma rate ratio	
	RE2	RE4	RE2	RE4
Env. Pres.	-0.09	-0.57	-0.17	-0.61
Bunker Temp.	0.33	-0.93	-0.03	-1.15
Bunker air R.H.	2.65	1.17	2.56	0.77
Supply gas Temp.	-0.07	-1.08	-0.42	-1.28
Exhaust gas Temp.	0.02	-1.14	-0.34	-1.34
Supply gas R.H.	0.29	-1.25	-0.17	-1.67
Exhaust gas R.H.	2.45	0.45	2.31	0.04

Table 5.7: Summary of the scalar product between the current density ratio and gamma rate ratio vectors, and the environmental parameters vectors in the principal component eigen vector space.

4487 5.3.7.2 Evolution of the detectors performance

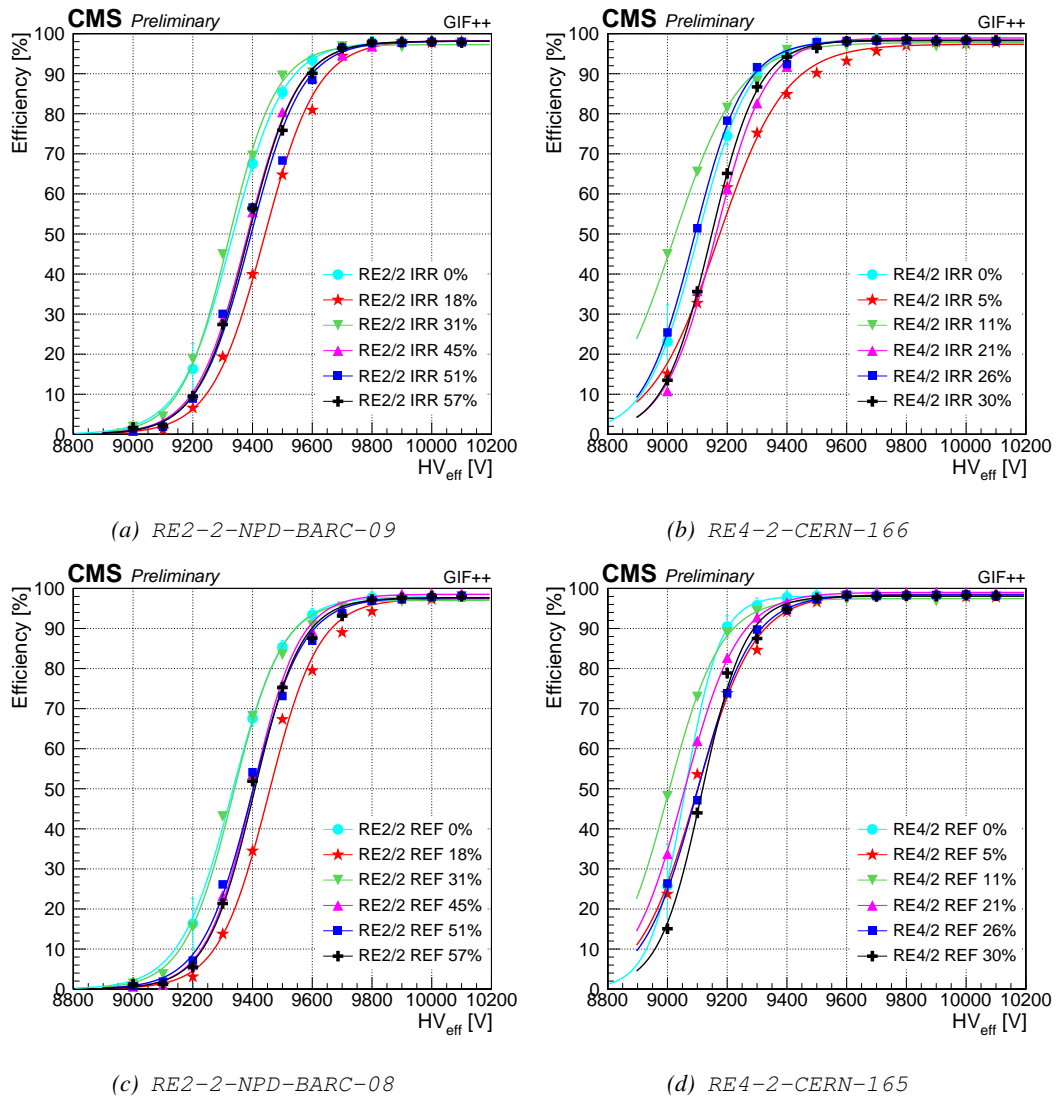


Figure 5.61

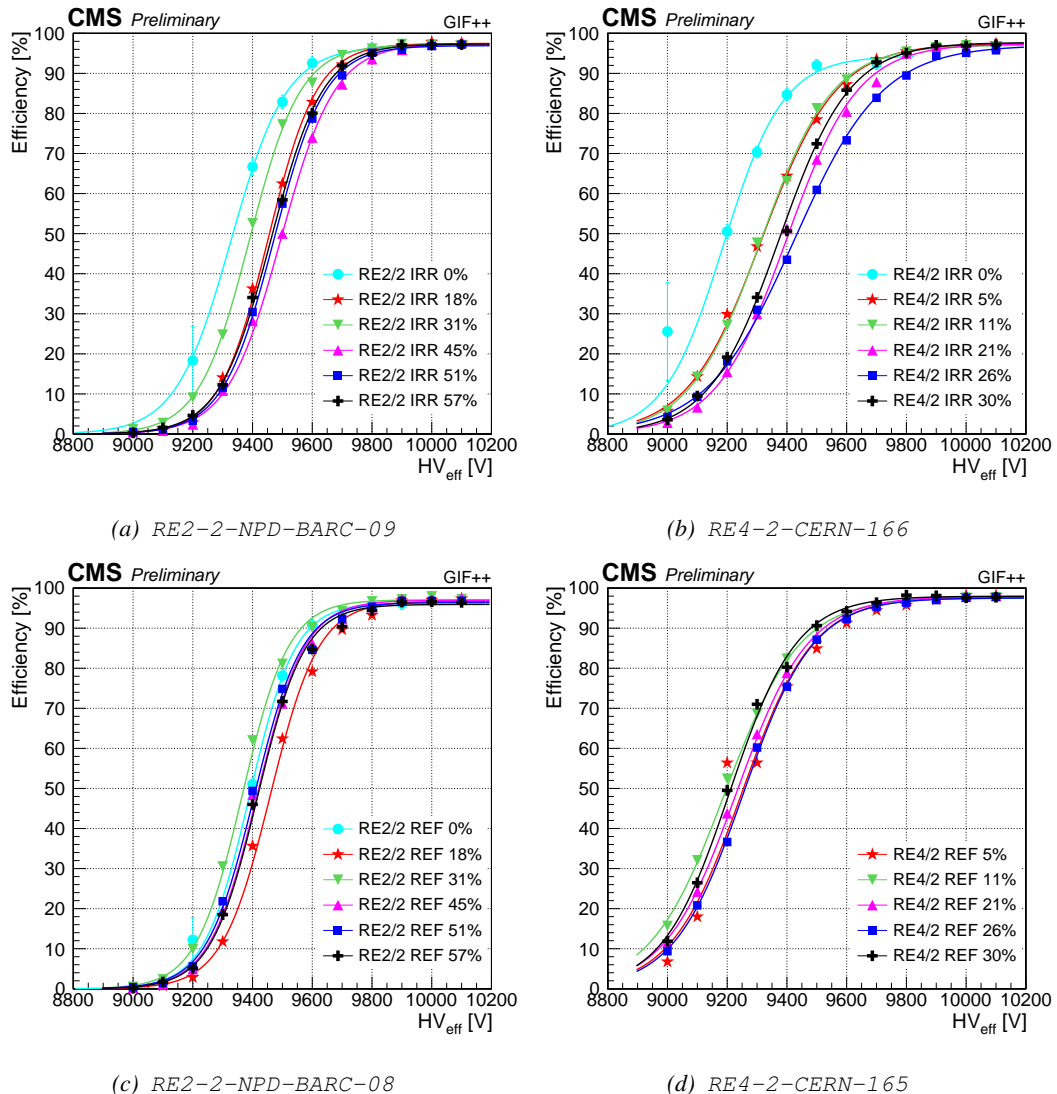


Figure 5.62

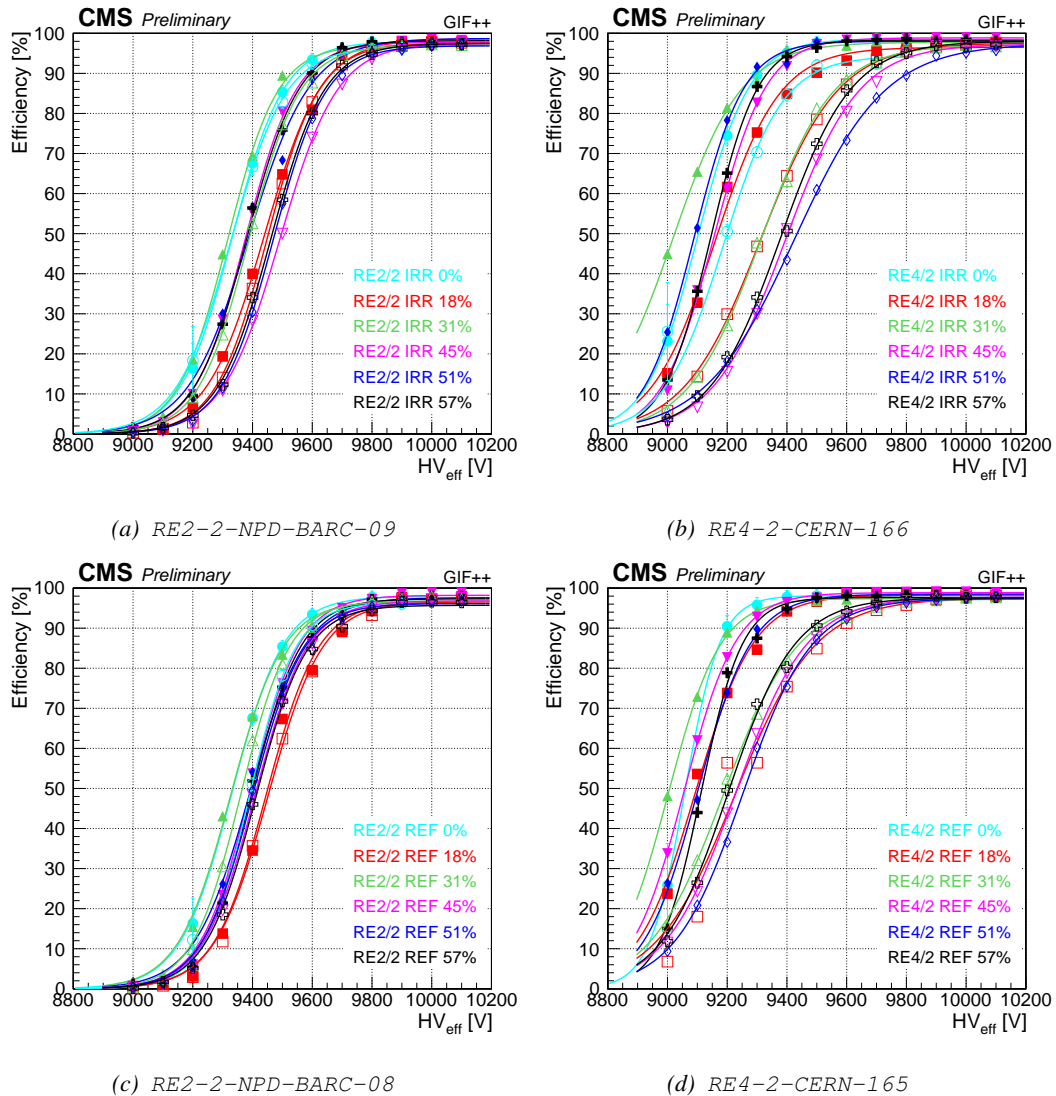


Figure 5.63

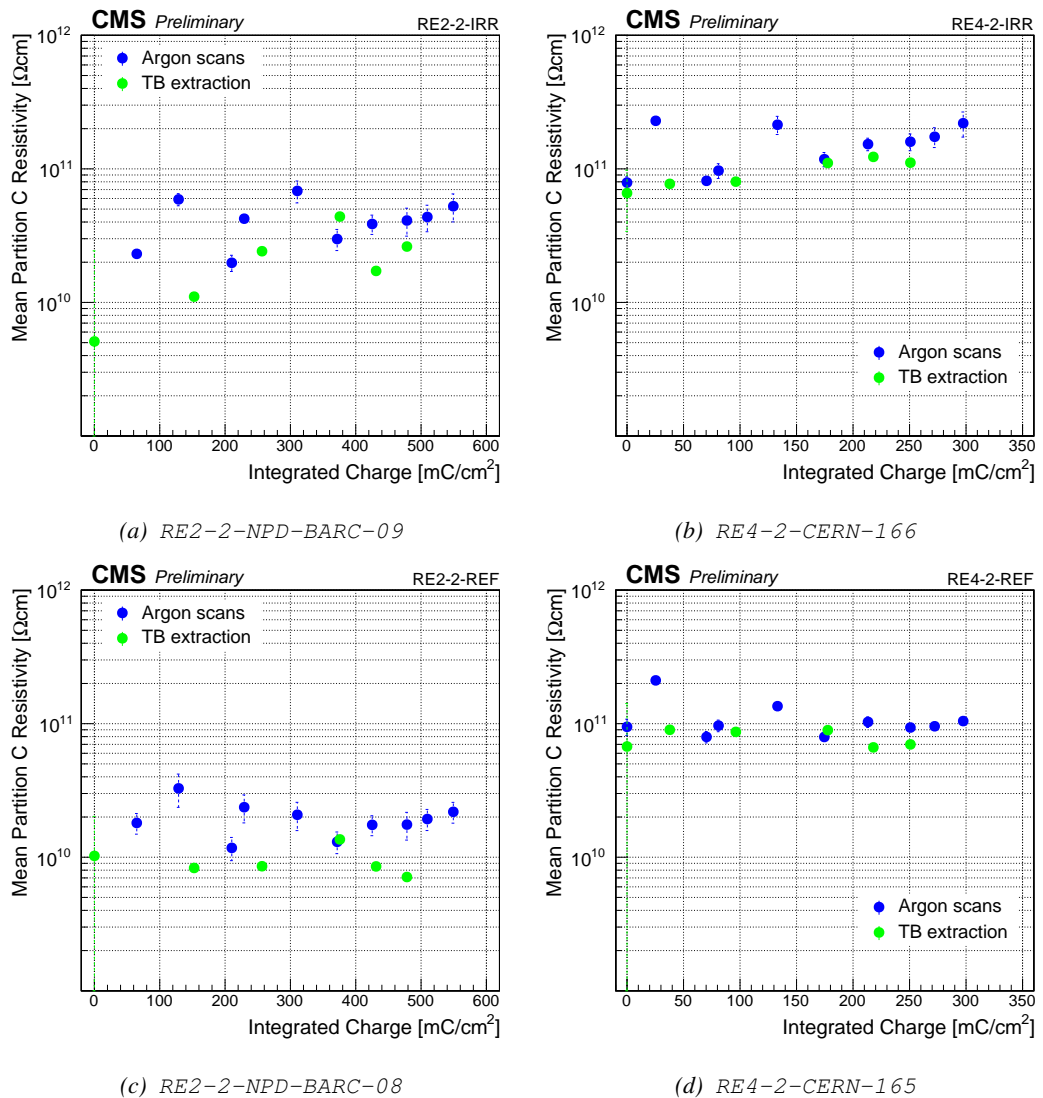


Figure 5.64

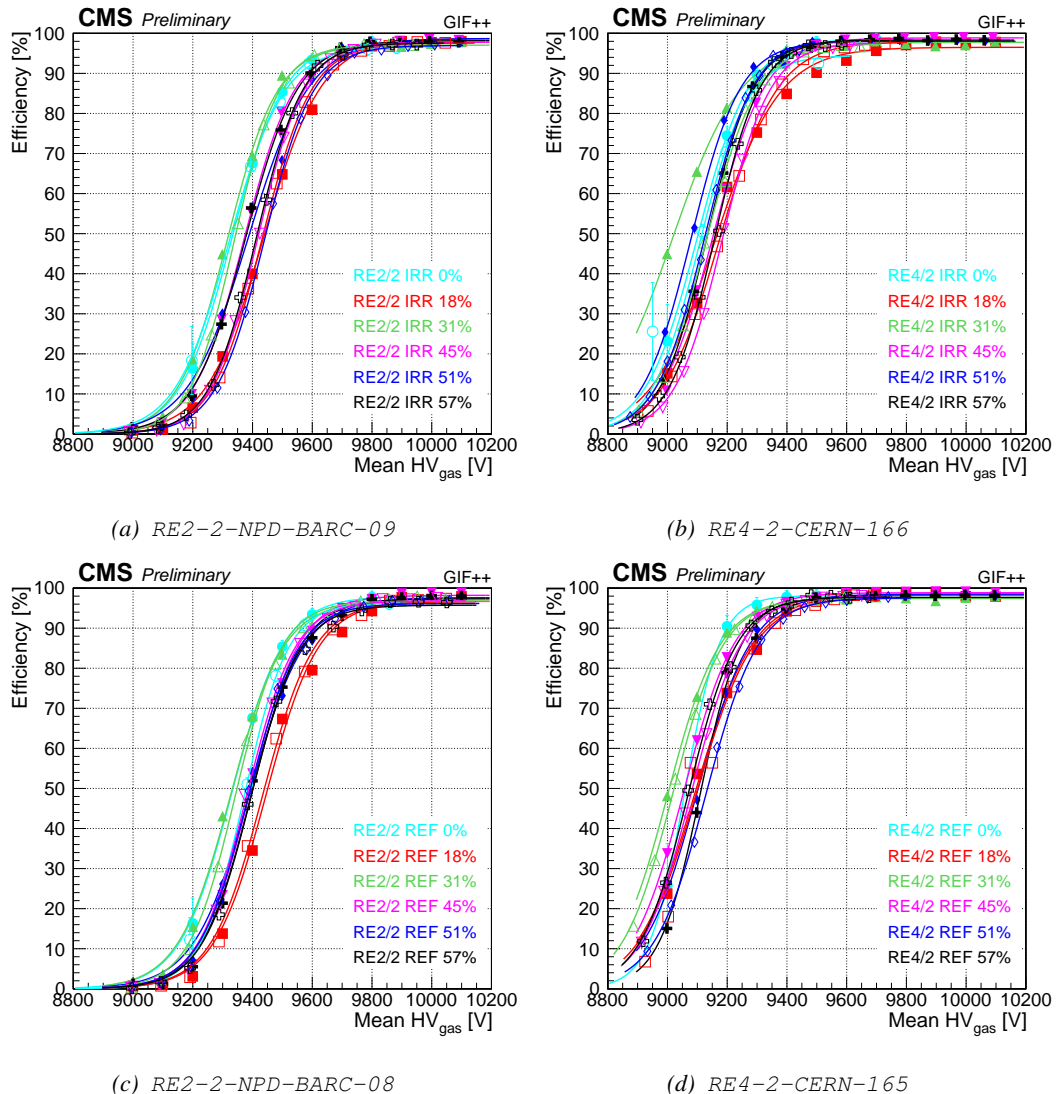


Figure 5.65